

UNIVERSITY OF OKLAHOMA

GRADUATE COLLEGE

DWARF GALAXIES IN N-BODY+SPH SIMULATIONS

A DISSERTATION

SUBMITTED TO THE GRADUATE FACULTY

in partial fulfillment of the requirements for the

Degree of

DOCTOR OF PHILOSOPHY

By

JORDAN D. VAN NEST

Norman, Oklahoma

2023

DWARF GALAXIES IN N-BODY+SPH SIMULATIONS

A DISSERTATION APPROVED FOR THE
HOMER L. DODGE DEPARTMENT OF PHYSICS & ASTRONOMY

BY

Dr. Ferah Munshi, Co-Chair

Dr. Mukremin Kilic, Co-Chair

Dr. Xinyu Dai

Dr. Nathan Kaib

Dr. Ian Sellers

Dr. Jessica Ruyle

Dr. Michael Tremmel

© Copyright by JORDAN D. VAN NEST 2023
All Rights Reserved.

Table of Contents

Abstract	vi
List of Tables	viii
List of Figures	x
1 Introduction	1
1.1 Background	1
1.1.1 Formation of Galaxies through Hierarchical Growth	1
1.1.2 Cosmological Simulations	4
1.1.3 Dwarf Galaxies and Challenges to Λ CDM	10
1.2 Outline	16
2 Quantifying the interplay between the Definition, Orientation, and Shape of Ultra-diffuse Galaxies Using the ROMULUS Simulations	21
2.1 Introduction	22
2.2 The Romulus Simulations	25
2.2.1 Sub-grid Physics and Star Formation	27
2.2.2 Halo Identification	29
2.2.3 UDG Identification	30
2.3 Shapes of UDGs and Non-UDGs	32
2.4 Effects of Changing Definition and Orientation	39
2.4.1 Definitions of UDGs	39
2.4.2 Definition Effects	41
2.4.3 Orientation Effects	43
2.4.4 Effects on Previous Results	56
2.5 Conclusions	57
3 The Role of Mass and Environment on Satellite Distributions around Milky Way Analogs in the ROMULUS25 Simulation	61
3.1 Introduction	62
3.2 Simulation	65
3.2.1 SF and gas cooling	67
3.2.2 Halo Identification	68
3.3 Analog and Satellite Identification	68
3.4 Results	73
3.4.1 Host Effects on Satellite Accumulation	73
3.4.2 Host Effects on Satellite Quenching	80
3.5 Discussion	89
3.5.1 Satellites within R_{vir} versus 300 kpc	89
3.5.2 Quenched Fraction Discrepancy	90
3.5.3 Isolated vs. Paired Hosts	91
3.6 Conclusions	93

4 A Study of Stellar Shapes in the Marvel-ous Dwarfs and DC Justice League Simulations	95
4.1 Introduction	95
4.2 Simulations	97
4.2.1 Star Formation and Gas Cooling	98
4.2.2 Halo Identification and Sample	99
4.3 Direct Measurements of Morphology	100
4.3.1 Isophote Fitting	100
4.3.2 The Shape Tensor	101
4.3.3 Triaxiality	106
4.4 Indirect Measurements of Morphology	108
4.4.1 Deprojection	108
4.4.2 The $\epsilon - \Sigma_*$ Correlation	112
4.5 Comparisons to SIDM	117
4.6 Conclusions	119
5 Conclusions	121
5.1 Summary	121
5.2 Future Work	125
References	128

Abstract

I present a study of various dwarf galaxies from N-body+SPH simulations in Λ cold dark matter cosmology. While the science results of this thesis pertain to dwarf galaxies of varying classifications and environments, I maintain a focus on how variations in definition and 3D-orientation affect these results. In a study of ultra-diffuse galaxies (UDGs), I show that those found in isolation are morphologically distinct from their non-UDG counterparts, a tracer of their unique formation channel through early, high-spin mergers. Randomly orienting and projecting our galaxies onto the 2D plane, however, removes any distinction between isolated UDGs and non-UDGs, suggesting that this difference will be difficult to detect with observations. Additionally, comparing various UDG definitions used in current literature shows that the number of UDGs identified in our simulations can vary drastically based on one's choice of definition, a result that is further complicated when considering various 3D orientations. More permissive definitions, that result in a large number of UDGs, tend to homogenize the UDG and non-UDG populations, erasing any observable distinction that may have existed.

I also present a study of study of Milky Way like galaxies and their satellite distributions, with a focus on comparing our results to the Satellites Around Galactic Analogs (SAGA) and Exploration of Local VolumE Satellites (ELVES) surveys. I show that host mass is a driving factor in both satellite accumulation and satellite quenched fraction, while host environment may have significant impact in extreme isolation. This impact can vary in strength depending on the criteria one

uses to identify both the Milky Way analogs and their satellites. While the SAGA and ELVES surveys show conflicting results in regards to quenched fraction, I show that this discrepancy originates in low-mass satellites, as restricting quenching analysis to high mass satellites shows good agreement between our simulation and both observational surveys.

Finally, I present a study of morphology measurements for dwarfs in high-resolution zoom-in simulations. In comparing the observation-based method of isophote fitting to the simulation-based method of shape tensor calculation, I show that isophote fitting tends to imply more elongated shapes than shape tensor calculations, and this discrepancy is stronger at more edge-on orientations. I also implement observation-based methods of 3D shape inference presented in current literature to see how they compare to shape tensor calculation. I show that while these inference methods well recover our sample space and our in good qualitative agreement, there is some decent scatter on a galaxy-to-galaxy basis. All methods, however, independently imply that our simulations contain an oblate, high-mass population of satellite galaxies.

List of Tables

2.1	A Summary of the UDG Definitions Considered	42
2.2	Counts of UDGs at Face-On Orientation	44
2.3	Counts of UDGs at Any Orientation	49
3.1	A Summary of the Milky Way Analog and Satellite Definitions Considered	70

List of Figures

1.1	Empirical Relations of Galaxy Properties	3
1.2	Halo Properties Constrained by DMO Simulations	6
1.3	Outline for Measuring DM Physics with Cosmological Simulations	17
2.1	Morphologies of our UDGs and non-UDGs	33
2.2	Time Evolution of Stellar Morphology for UDGs and non-UDGs .	37
2.3	Time Evolution of Spin for UDGs and non-UDGs	38
2.4	A Visual Example of our 3D Rotation Grid	46
2.5	An Example of a Rotation-Depend UDG Status	47
2.6	Aggregate UDG Grids for all Definitions and Environments . . .	51
2.7	Breakdown of Individual UDG Percentages and Position in Definitions' Parameter Spaces	53
2.8	Mass Function of UDGs in Different Environments	55
2.9	Ellipticity Functions for our 2D Projected UDGs	56
2.10	Morphologies of our UDGs and non-UDGs Under a Less Restrictive Definition	58
3.1	Milky Way Analog Sample Comparison	72
3.2	Comparison of Romulus25 Milky Way Analogs to SAGA and Elves	74
3.3	Luminosity Functions of Milky Way Analogs	75
3.4	Milky Way Analog Satellite Abundance binned by Mass and Environment	77

3.5	Specific Frequency of Satellite Abundance normalized to Mass and Environment	79
3.6	Average Satellite Abundance binned by Environment	81
3.7	Quenched Fractions of Romulus25, SAGA, and ELVES	83
3.8	Specific Frequency of Quenched Fraction normalized to Mass	86
3.9	Average Quenched Fractions binned by Environment	88
4.1	Examples of Isophote Fitting and Masking	102
4.2	Comparison of Isophote and Shape Tensor axis-ratios at Face-on and Edge-on positions	104
4.3	Discrepancy between Isophote and Shape Tensor axis ratios as a Function of Viewing Orientation	105
4.4	Triaxiality of Stellar and Dark Matter Halos as a Function of Stellar Mass	107
4.5	Comparison of Morphologies measured by Shape Tensor and MCMC Deprojection	111
4.6	Full Sample Measurements of the Ellipticity-Surface Brightness Correlation	113
4.7	Individual Measurements of the Ellipticity-Surface Brightness Correlation	116
4.8	Preliminary Results of CDM-SIDM Comparison	118

Chapter 1

Introduction

1.1 Background

1.1.1 Formation of Galaxies through Hierarchical Growth

When studying galaxies, we are examining the universe at the largest scales, where the dominant force is gravity and the interactions of large potential wells that come with dense groupings of matter. The preferred model for galaxy formation is hierarchical growth within a Λ -Cold-Dark-Matter (Λ CDM) cosmology, wherein dark matter interacts with itself and baryonic matter (stars, dust, gas, etc.) only through gravity [1].

Within this paradigm, small over-densities in the early universe collapse under gravity to form small halos, which, over time, grow into larger halos via accretion of surrounding matter and/or mergers with other halos. This structure formation is driven by dark matter and its associated gravitational potential. As over-densities in dark matter are spun-up by tidal torquing, they begin to collapse under gravity, and this collapse is eventually halted upon reaching virialization (the gravitationally stable state in which the magnitude of the potential energy is twice that of the kinetic energy). The larger concentration of mass within dark matter, along with its dissipationless nature, means that it will collapse before the baryonic matter, which, in the case of the first halos, was only hydrogen and helium (in a 3:1 ratio). While the gas collapses into the potential well of the

dark matter halo, it both cools and decouples from the virialized dark matter halo, settling into a rotating disk [2, 3, 4, 5, 6]. In the pristine gas of the early universe, cooling was driven by recombination radiation, collisional excitation and emission, Bremsstrahlung radiation, and Compton radiation. However, at low temperatures ($< 10^4 K$), atomic hydrogen does not radiate, and it must instead rely on molecular hydrogen cooling. This form of cooling was dominant at high redshift during the formation of the first massive stars [7], a candidate source for the reionization of the universe [8, 9, 10, 11].

This framework of dark matter collapse followed by baryonic collapse, cooling, and star formation favored by many analytic models [2, 3, 12] can explain several empirical relations observed in the universe, such as the Tully-Fisher [13], Luminosity-Size [14, 15], and mass-metalicity relations [16, 17, 18] (see Figure 1.1). Yet, this model does not factor in mergers or interactions with other halos, which are a key part of a galaxy's evolution. In 1972, Toomre & Toomre [19] were one of the first to demonstrate how close interactions between galaxies can alter their evolution. With the advent of simulations that include gas dynamics as well as star formation and feedback, it has also been shown that mergers, both major and minor, can have a strong impact on the structure and evolution of the galaxies [20].

Following the formation of the first stars, galaxies continue to grow and merge, forming the large scale structures seen in the universe today. Dark matter forms the cosmic web: a filamentary structure of dense, connected nodes and empty voids. Baryonic matter follows the dark matter potential, with massive galaxy

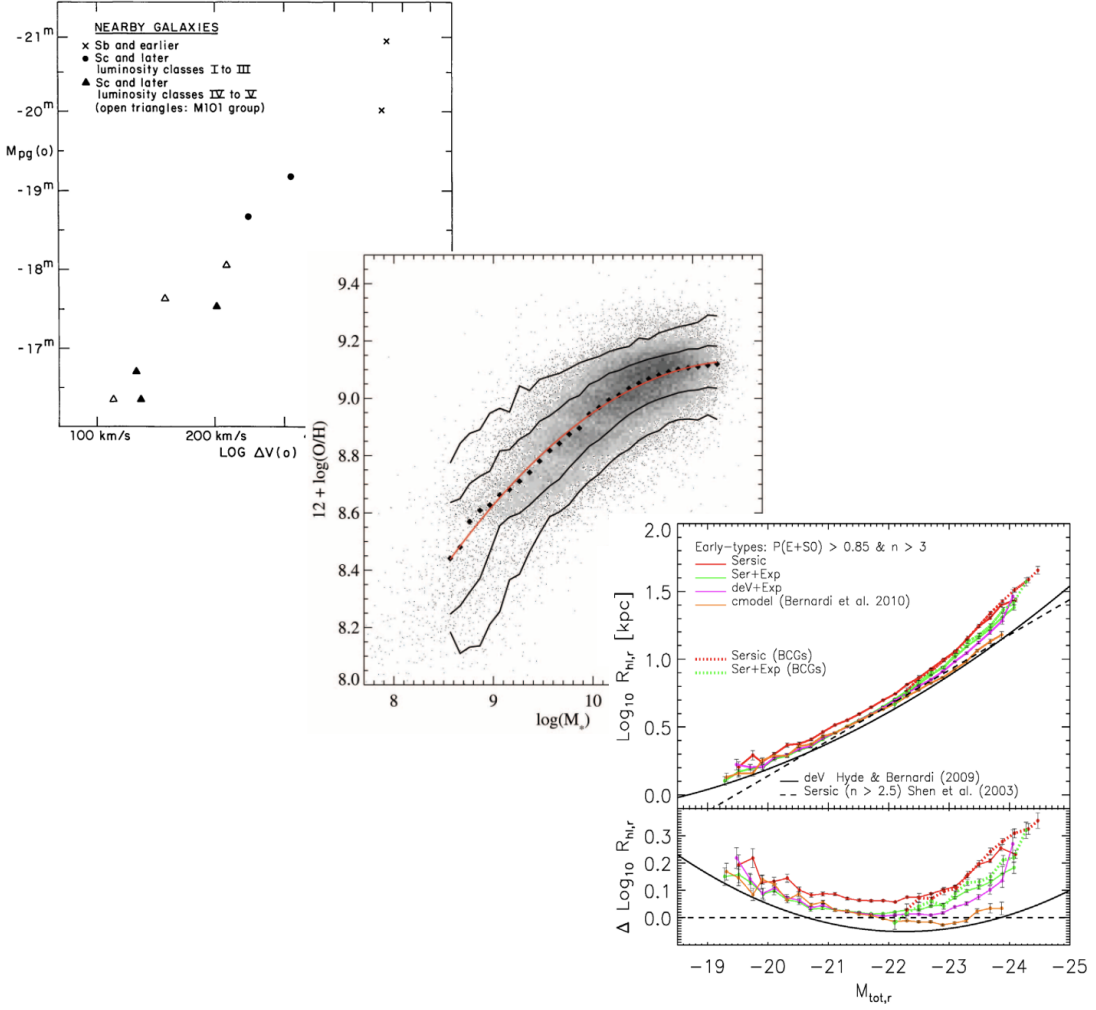


Figure 1.1: Examples of the derived empirical relations for galaxies. **(Top)** The Tully-Fisher relation correlating magnitude to global HI profile width, a distance-independent observable [13]. **(Middle)** The mass-metallicity relation correlating gas-phase oxygen abundance and stellar mass [17]. **(Bottom)** The Luminosity-Size relation correlating magnitude and half-light radius [15].

clusters and groups forming in the dark matter nodes, hosting large, elliptical galaxies at their centers and smaller, spiral galaxies farther out [21, 22, 23, 24, 25].

In looking at the lowest mass galaxies, they can be found within the substructure of larger galaxies, or in isolation within low-density regions of the universe [26, 27].

With this variety in size and morphology also comes variety in properties like color, metalicity, star formation history, and baryonic mass fraction. Spiral galaxies tend to be blue, gas rich, and actively star forming, while ellipticals are often red, gas poor, and contain an aging stellar population that is not forming new stars [28, 29, 30, 31]. The manifestation of these trends strongly prompts questions of how a galaxy’s formation and evolution result in its observed properties (e.g. “how does mass affect color?”, or “how does merger history affect morphology?”). Given the vast number of processes to consider (star formation history, merger history, gas accretion, etc.), and the fact that these processes operate on time-scales comparable to the age of the universe, cosmological N-body simulations present themselves as an extremely effective tool.

1.1.2 Cosmological Simulations

Under Λ CDM, dark matter operates as collisionless particles interacting only through gravity. Thus, they are ideal candidates for N-body simulations. Dark matter only (DMO) simulations are not only fast and computationally inexpensive (due to gravity being the only force considered), they are extremely valuable in modeling halo growth as it enters the non-linear regime, wherein matter density becomes high enough to break the linear approximations of gravitational

collapse. Due to their “computational simplicity”, DMO simulations are easily able to simulate large volumes of galaxies in order to study aspects of hierarchical formation [32, 33, 34, 35, 36, 37]. Armed with large populations of simulated galaxies, DMO simulations can help us understand universal properties such as the dark matter halo mass function (see Figure 1.2(a)) [38, 33, 39, 40, 41, 36], the mass power spectrum [4, 42, 43, 32, 36, 37], and galaxies’ merger histories as a functions of mass and environment [20, 44, 45, 36, 46, 47]. In addition to large sample analysis, DMO simulations can help illuminate characteristics of individual halos, such as the halo’s density profile (see Figure 1.2(b)) [48, 49, 50, 51, 52], angular momentum and morphology [53, 54, 55, 56, 57], and even its substructure [58, 59, 60, 35].

While DMO simulations have proven quite useful, they are beholden to the adage ”you get what you pay for”. While they are computationally inexpensive and quick to run, DMO simulations lack baryonic content, i.e. the matter than we can directly observe in our universe. So for comparisons to be made between observations and simulations, either observers need to extrapolate information about a galaxy’s dark matter halo based on its gravitational interaction with the baryonic content, or simulations need to extrapolate the baryonic matter that would be present in the simulated dark matter halo. In the latter scenario, there are a few primary methods that have been used in the past:

- **Abundance Matching:** matching the abundance of dark matter halos in a large cosmological volume to the luminosity function [61, 60, 62, 63]

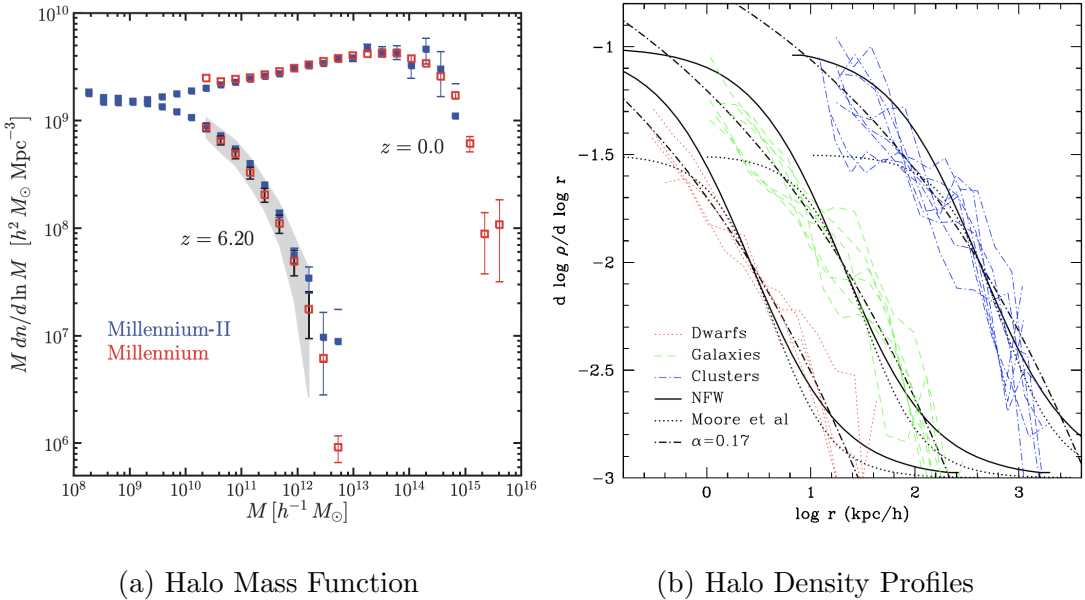


Figure 1.2: (a) Halo mass functions, i.e. the number density of dark matter halos as a function of halo mass, for the Millennium-I and -II DMO simulations [36]. (b) Halo density profiles, i.e. the slope of the dark matter density as a function of radius, from DMO simulated halos.

- **Halo Occupation Distribution:** matching the luminosities and distribution of galaxies in a cluster to the substructure in dark matter halos [64, 65, 66, 67, 68]
- **Semianalytic Modeling:** applying basic analytic models for baryonic processes, such as star formation, gas cooling, and supernova feedback, for a dark matter halo based on its mass and formation history [69, 70, 71, 72, 73, 33, 74, 75, 76]
- **N-body+Hydrodynamic Simulations:** fully self-consistent simulations of galaxy formation that include gravity and gas dynamics [77, 78, 79, 80, 81, 82, 83, 84]

All of the above methods come with their own advantages, and disadvantages, which one must consider before implementing them. By their very nature, abundance matching and the halo occupation distribution will be in very good agreement with observations, as the observational data is essentially being plugged into the simulation. They do not, however, provide any insight into the evolutionary processes that created the final state of the galaxies; rather, they provide a simple snapshot of the galaxies at the given time. On the other hand, semianalytic models and hydrodynamic simulations are able to model physical processes throughout the evolution of the galaxies [85, 86, 87]. Since semianalytic models are effectively applied on top of DMO simulations, they retain their speed and computational “ease”. However, they contain a large number of free parameters that must be hand tuned, each of which can introduce a large amount of variability in the results.

Hydrodynamic simulations have notably fewer parameters to tune compared to semianalytic models. Instead, they can fully trace the galaxy evolution with few assumptions as well as simulate the interactions between the baryonic and dark matter [88, 89, 90, 91, 92]. Although the dark matter content of a halo is significantly more than that of the baryonic matter, it has been shown that baryons can impact dark matter through gas loss/accretion, angular momentum redistribution, and dark matter core formation [1, 93, 94, 95, 96, 97].

While the hydrodynamic simulations can model the baryon-dark matter interactions with a minimal set of assumptions, they do come at a significant computational cost when compared to DMO simulations. In addition to the gravitational calculations for dark matter particles, these simulations include baryonic particles which utilize by fluid dynamics equations to determine properties such as gas temperature, pressure, and density. There are two prominent methods for implementing hydrodynamics into an N-body simulation: the Lagrangian (SPH) method [98, 99] and the Eulerian (AMR) method [100, 101]. The Eulerian method, used in codes like ENZO [102], FLASH [103], and RAMSES [104], implements an adaptive mesh over which the hydrodynamic equations are solved over grids of varying resolution within discrete volumes. The Lagrangian method, used in codes like GADGET2 [105] and GASOLINE/GASOLINE2 [82, 106], utilizes smoothed particle hydrodynamics wherein the hydrodynamic equations are used to trace the temperature, pressure, and density for individual particles that represent the gas. Additionally, there are hybrid codes ,such as AREPO [107] and GIZMO [108], that attempt to merge the best features of each method.

Within N-body+hydrodynamic simulations, there are processes that occur below the resolution limit. Since particles/meshes within the simulations represent volumes of gas instead of individual atoms (and populations of stars rather than individual ones), processes such as star formation, supernovae feedback, and metal enrichment are handled by analytic “subgrid models”. Despite resolution limits and the dependence on analytic subgrid models, hydrodynamic simulations have had great success in recreating observed empirical scaling relations such as the mass-metallicity relation [109], the size-luminosity and size-velocity relations [110], and the stellar mass-halo mass relation [111].

The simulations considered in this thesis are N-body+SPH run using the code CHANGA [112], which implements hydrodynamic models from GASOLINE2 [82, 106]. In Chapter 2, I introduce the ROMULUS25 and ROMULUSC simulations. ROMULUS25 [113] is a 25 Mpc-per-side uniform volume simulation (i.e. a box whose sides are 25 Mpc in length) containing hundreds of galaxies in field, group, and satellite environments, while ROMULUSC [114] is a zoom-in simulation of a galaxy cluster. Both of the ROMULUS simulations were run with a Λ CDM cosmology following the Planck Collaboration [115], and gravitational interactions are resolved with a spline force softening length of 350 pc that converges to Newtonian force at 700 pc. The initial dark matter and gas particle masses are $3.39 \times 10^5 M_\odot$ and $2.12 \times 10^5 M_\odot$, respectively. Star particles form at 30% the initial gas particles mass ($6 \times 10^4 M_\odot$). In Chapter 4, I introduce the “Marvel-ous Dwarfs” and “DC Justice League” suites of zoom-in simulations (Marvel and DCJL) [116]. Marvel is a suite of four simulations that recreate a few dozen dwarfs

in an environment similar to the Local Volume. They were run with a WMAP3 cosmology [117], have a force resolution of 60 pc, and have gas, initial star, and dark matter particle masses of $1410M_{\odot}$, $420M_{\odot}$, and $6650M_{\odot}$, respectively. DCJL is a suite of for zoom-in simulations of around 1 Mpc regions centered on Milky Way mass galaxies. They were run with a Planck cosmology [118], have a force resolution of 170 pc, and have initial gas, initial star, and dark matter particle masses of $2.7 \times 10^4M_{\odot}$, $8 \times 10^3M_{\odot}$, and $4.2 \times 10^4M_{\odot}$, respectively.

1.1.3 Dwarf Galaxies and Challenges to Λ CDM

The Λ CDM model has been a dependable framework for explaining our observed universe, and simulations have largely agreed. As mentioned in Sections 1.1.1 & 1.1.2, the hierarchical growth model within a CDM framework has well explained various empirical relations, and cosmological simulations have helped inform our understanding of individual halo structures as well as global statistics. Beyond this, Λ CDM has successfully predicted fluctuations in the Cosmic Microwave Background [119, 120] and the large-scale clustering of galaxies at different redshifts [121, 122, 123, 124]. However, these successes have largely been limited to the large-scale structures of our universe. As the small scale regime becomes more accessible to us through stronger observational instrumentation, higher resolution simulations, and better models for subgrid physics, some issues begin to arise.

The focus of this thesis is on dwarf galaxies, generally defined as having stellar masses below 10^9M_{\odot} . They are predicted to be the most abundant, dark matter dominated galaxies in the universe, so it is important that our theories about small

scale structure are in agreement with observations. There are some noteworthy observations, however, in which the theoretical results are in conflict. Possible solutions to these discrepancies have been put forward, and can involve anything from altering/improving the physics of simulations, to completely abandoning Λ CDM in favor of a different cosmology all together.

One of these discrepancies is known as the “missing satellites” problem. While the number of large galaxies in simulations matches what is observed in the universe, simulations tend to drastically over-predict the number of dwarf satellite galaxies [125, 59, 58]. Even as observations improved to detect ultra faint dwarfs [126, 127, 128], high resolution simulations vastly over predict the number of satellites [129, 130, 35, 131, 132]. Additionally, this problem extended beyond satellites into the low-density field with the “missing dwarfs” problem. Measurements of rotational velocity (as a kinematic tracer of mass) indicated a significant lack of low velocity (low mass) galaxies when compared to Λ CDM estimates [133, 134].

A potential solution to the missing satellites problem suggested that some satellites of the Milky Way were tidally disrupted/destroyed, thus the lower satellite count when comparing to simulations. This, however, introduces a new issue: the “too big to fail” problem. The supposed stripped satellites would reside in dark matter halos that are simply too large to facilitate the desired level of interference, or, put in another way, simulated satellites of Milky Way-like galaxies are notably larger than the ones observed around the Milky Way and Andromeda (M31) [135, 132, 136, 137, 138].

As a final note on satellite galaxies, there exists the “planes of satellites”

problem, in which a high fraction of satellites orbit their host in a relatively flat, rotating plane, a phenomenon rarely seen in Λ CDM simulations [139, 140, 141, 142]. The other “problems” discussed here can be related to the internal processes of individual galaxies, be it baryonic or dark matter. The planes of satellites problem is an exception to this, however, as the macroscopic orbital dynamics of host and satellite galaxies is dominated solely by gravity, making it a particularly difficult problem to solve. It has been suggested, however, that this is not significant issue as the planar nature of observed satellites is ambiguous, and that the current alignment of Milky Way satellites may only be temporary [143, 144].

Another point of contention is known as the “cusp-core” problem. When looking at the dark matter density profiles of simulated galaxy, they are all centrally dominated and “cuspy”, having steep logarithmic profiles. However, the observed rotation curves of galaxies in the dwarf to low-mass spiral regime indicate that the dark matter density profile is “cored” in the center, having flat logarithmic profiles [145, 146, 147, 148, 149]. An extension of this problem is seen when looking at the baryonic content of these galaxies. Λ CDM simulations typically produce dense, spherical stellar bulges as low-angular momentum material migrates to the center through accretion and mergers [150, 151, 152]. Observations, on the other hand, often suggest rotating stellar discs [153]. The cusp-core and missing dwarf/satellites problems may possibly be related, and, thus, simultaneously addressed, as centrally dominated, cuspy halos are harder to disrupt than cored halos, which could lead to greater halo substructure [154].

Looking again at the inner regions of galaxies, only now at their baryonic

content, we find the “rotation curve diversity problem”. Galaxies’ rotation curves (rotational velocity as a function of radius), are typically characterized by measurements of the maximum velocity (v_{\max}) and measurements of the inner region, typically at 2 kpc from the galaxies’ centers ($v_{2\text{kpc}}$). While the baryonic Tully-Fisher relation (see [155] and references within) shows a tight correlation between v_{\max} and total baryonic mass, measurements of $v_{2\text{kpc}}$ for galaxies with similar v_{\max} show significant diversity [156, 140]. This is at odds with Λ CDM predictions, wherein equivalent mass galaxies exhibit relatively equivalent rotation curves.

At the extreme end of solutions to these problems, theorists have considered replacing Λ CDM with an alternate cosmology. One considered alternate is Warm Dark Matter (WDM) [157], as simulations have shown it to be successful in lowering central halo concentrations and the number of satellites [158, 157, 159, 160]. However, a new problem arises when considering WDM, as observations of the Lyman- α forest indicates more power at small scales than WDM theory predicts [161, 162]. These observations rule out lighter mass WDM candidates, while higher masses have also been ruled for not suppressing enough structure at low masses to be compatible with the observed velocity function of galaxies [134, 163, 164].

Another cosmological model becoming favored alongside Λ CDM is self-interacting dark matter (SIDM) [165, 166, 167, 168, 169, 170, 171], wherein dark matter particles interact with each other over a non-negligible cross section of order $1 \text{ cm}^2 \text{g}^{-1}$. While this cross section is typically modeled as fixed, velocity-dependant cross section models have also been considered [172, 173, 174]. These collisions, which

would be most frequent in the halo’s center where dark matter density is highest, create an outward pressure that reduces the central density of the dark matter, forming a core and alleviating the core-cusp problem [168, 169]. As previously mentioned, this cored density could also alleviate the missing satellite problem by making the halo more susceptible to tidal disruption. The interactions of baryons in this cored inner region has also been shown to fix the diversity of rotation curves problems, allowing simulated galaxies to recreate diverse inner regions of observed galaxies. [175, 176]. This core formation in SIDM, however, is not stable over cosmic time scales. As scatterings transfer heat to the outer regions of the halo, the inner region experiences the infall of dark matter to tight, central orbits, where it becomes even hotter. This self-perpetuating process can “runaway”, causing core collapse [177, 169, 178]. This process, which in dark matter models is unique to SIDM, results in a sharply cuspy dark matter profile. While the timeline for this process under most modeled cross sections is longer than the age of the universe [179, 180, 181, 182], tidal disruptions have been shown to accelerate this process [178, 183, 182]. Thus, the coexistence of dark matter cores and cusps within SIDM can alleviate the core-cusp problem, the rotation curve diversity problem, as well as diversity within Milky Way dwarf spheroidal satellites [184, 185, 186, 182].

There are alternative solutions, however, that allow us to remain within the well tested Λ CDM paradigm. Simulations have been able to address these issues primarily through the increased fidelity of modeling the physical process undergone by baryons. The focus of these changes has largely been limiting star formation,

with an emphasis on feedback models. Implementing UV background radiation has been shown to reduce the number of small halos in simulations [187, 188, 189], though not enough to fully account for the missing satellites problem [190, 191]. Feedback from active galactic nuclei and supernovae have also been shown to reduce star formation in galaxies [74, 75, 192, 2, 6, 193]. While these feedback processes can reduce the number of low mass satellites (alleviating the missing satellite problem), they can also be strong enough to form dark matter cores through the baryon-dark matter interactions [97, 194, 195]. Thus, improved baryonic physics within simulations are able to rectify the discrepancies between Λ CDM theory and observations.

I note, however, that not yet needing to replace Λ CDM is no guarantee that it is correct. In a direct comparison of CDM and WDM, Governato et al. [164] show that the central distributions of galaxies, where several of the aforementioned small-scale problems arose, are driven primarily by the baryonic physics, not the dark matter model. Thus, alternate cosmological models, such as SIDM, while not requiring improved baryonic physics to solve some of these problems, remain viable after they have been implemented (see [196] for a direct CDM-SIDM comparison).

As cosmic probes of dark matter have helped constrain microscopic properties of dark matter (see [197] for an overview), focus on the particle nature of dark matter has only grown. Currently, there are several theorized dark matter models such as Fuzzy CDM [198], Decaying CDM [199], Annihilating CDM [200], primordial black holes [201, 202], and axion/axion-like particles [203, 204]. Even within a given framework, various particle natures of dark matter are being considered. In

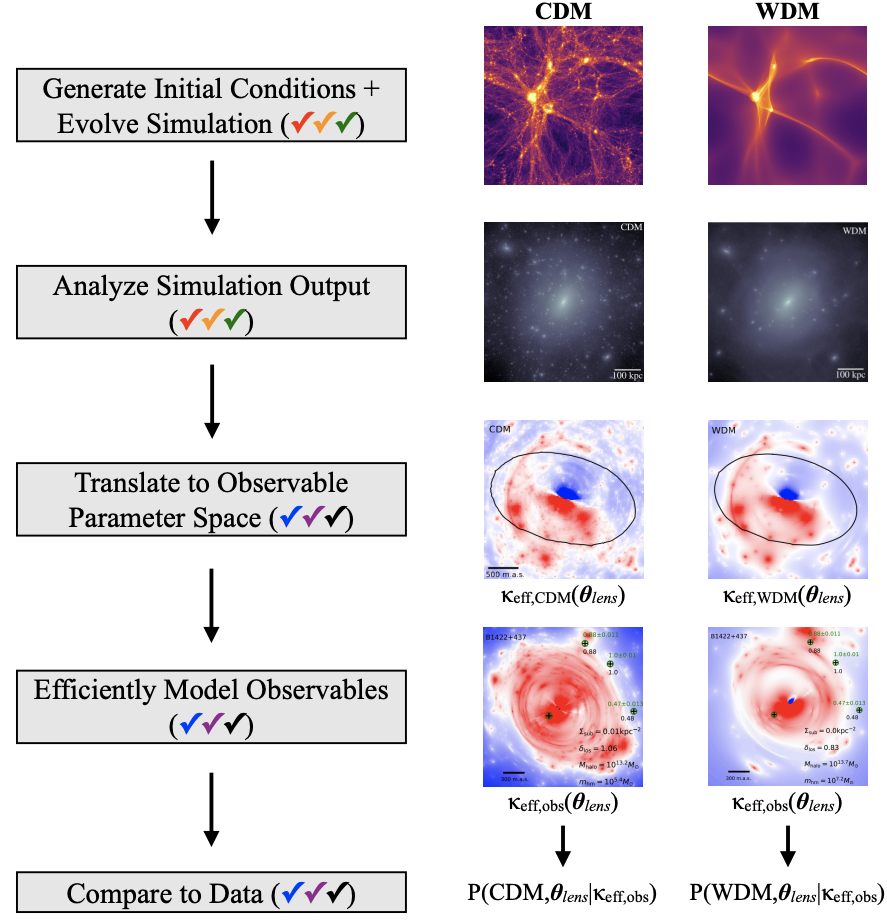
SIDM, for example, dark matter particles could be modelled as dark baryons, or as some fermion interacting with a light mediator within a Yukawa potential (see [171] for an overview of SIDM particle models). The advent of next generation observatories, like JWST [205] and The Rubin Observatory with its Legacy Survey of Space and Time (LSST) [206], will help significantly in constraining dark matter properties. However, the observed degeneracies between baryonic physics models and dark matter models all but necessitate the use of high resolution simulations to constrain dark matter properties [207, 208]. To this end, the Snowmass Community, in their 2021 meeting, put forward a simulation/modeling focused program, emphasizing collaboration at the intersection of observational astronomy, cosmological simulations, and particle physics, as a clear road into future measurements of dark matter constraints [209] (see Figure 1.3 for a general outline). While this focus on improved simulations and observational comparisons is not relegated only to the study of dwarf galaxies, the small-regime remains a vital area of focus for testing our understanding of the universe.

1.2 Outline

This thesis is primarily a study of dwarf galaxies within N-body+SPH simulations, both large volumes and zoom-ins, in Λ CDM cosmology. The following questions of dwarf formation and evolution are addressed in this work:

- Are ultra-diffuse galaxies a unique subset of dwarf galaxies, or the tail end of a distribution? Are there any observable properties or

Measuring Dark Matter Physics using Cosmological Simulations



Need #1: Collaboration between simulators and particle theorists

Need #2: Algorithm development and code comparison tests

Need #3: Hydrodynamic simulations for observational targets

Need #4: Compare simulations to data in observable parameter space

Need #5: Fast realizations of observed systems to constrain dark matter

Need #6: Provide guidance to observers about dark matter signatures

Figure 1.3: Figure 1 from the Snowmass21 White Paper [209]. A flowchart for measuring dark matter physics using cosmological simulations and connections to the Needs outlined in Snowmass21.

evolutionary differences that set them apart?

- **How are satellite galaxies around Milky Way analogs impacted by their hosts' masses and environments? Are the satellite distributions of the Milky Way and M31 “normal” within the universe at-large?**
- **How do “observation-based” and “simulation-based” methods of shape measurement compare? Are observational methods of 3D shape inference able to well recover intrinsic stellar structure?**

While various types and aspects of dwarf galaxies are presented throughout the following chapters, the following questions, which are difficult (if not impossible) to answer through observational astronomy, are also considered throughout the thesis as whole:

- **How does one's definition of an astronomical object affect the resultant population?** The time and tools available to astronomers are woefully finite when compared to the universe full of objects we wish to study and understand. As such, various research groups have access to different information and physical properties to select upon when classifying groups of objects (e.g. ultra-diffuse galaxies and Milky Way analogs, which are considered in this work). Does using one definition over another lead to different, or even conflicting, results?
- **Does changing an objects orientation relative to the observer affect the conclusions drawn?** As simulators, we have access to the intrinsic,

3D properties of a galaxy, and so we can observe it in whichever way is convenient. Observation data, however, is limited to a single 2D projection upon the plane of the sky, and as such, is quite limited. By considering all the orientations of simulated objects, do we discover new/differing results than those drawn from observations?

- **How can answering the above questions aid the efforts of observational astronomy?**

In Chapter 2, I present a study of ultra-diffuse galaxies (UDGs) within the ROMULUS25 and ROMULUSC volume simulations. As a result of only recently being detectable in large numbers, there is no strict, singular definition used when identifying UDGs. I show that these differences in definition, though slight, can have massive impacts on the resulting UDG population, and this is further complicated when considering the fact that galaxies may or may not be identified as UDGs depending on their inclination angle. As an example, under a particular UDG definition, I show that isolated UDGs are a distinct subset of dwarf galaxies that underwent early, high-spin mergers (identifiable via their oblate morphologies at redshift $z = 0$). However, when identifying UDGs under a more permissive definition, the distinct morphologies/merger histories between isolated UDGs and non-UDGs are lost as the two populations become homogenized.

In Chapter 3, I present a study of Milky Way (MW) analogs and their satellites within the ROMULUS25 volume simulation. I show that, as with UDGs, the choice of definition when identifying both MW analogs and their satellites can impact

the resultant populations. In studying how satellite abundance and quenched fraction relate to the properties of the MW analog, I show that both trend positively with MW analog mass while analog environment doesn't have a strong impact until extreme isolation. I show that these results are consistent with observations through direct comparison to the Satellites Around Galactic Analogs and Exploration of Local VolumE Satellites surveys.

In Chapter 4, I present a study of stellar morphology in the Marvel-ous Dwarfs and DC Justice League suites of zoom-in simulations. In comparing various methods of morphological measurement, I show that observational projection based methods (particularly isophote fitting) tend to imply more elongated shapes than more simulation based methods (particularly shape tensor measurements through angular momentum), and this discrepancy increases with inclination angle. I show that methods of inferring 3D morphologies from distributions of 2D projections, such as ellipticity-surface brightness correlation, are in good agreement with shape tensor measurements, and all 3D morphology measurement methods indicate the presence of an oblate, high-mass population within the simulations. I also present preliminary results of SIDM simulations, showing that the inner regions of the resultant halos are notably rounder than their CDM counterparts.

Finally, in Chapter 5, I summarize the main conclusions of this thesis and discuss future steps that can be taken to further this body of work.

Chapter 2

Quantifying the interplay between the Definition, Orientation, and Shape of Ultra-diffuse Galaxies Using the ROMULUS Simulations

Reproduced from Van Nest et al. 2022 [210] with permission from the AAS

We explore populations of ultra-diffuse galaxies (UDGs) in isolated, satellite, and cluster environments using the ROMULUS25 and ROMULUSC simulations, including how the populations vary with UDG definition and viewing orientation. Using a fiducial definition of UDGs, we find that isolated UDGs have notably larger semi-major (b/a) and smaller semi-minor (c/a) axis ratios than their non-UDG counterparts, i.e., they are more oblate, or diskier. This is in line with previous results that adopted the same UDG definition and showed that isolated UDGs form via early, high-spin mergers. However, the choice of UDG definition can drastically affect what subsets of a dwarf population are classified as UDGs, changing the number of UDGs by up to $\sim 45\%$ of the dwarf population. We also find that a galaxy's classification as a UDG is dependent on its viewing orientation, and this dependence decreases as environmental density increases. Overall, we conclude that some definitions for UDGs used in the literature manage to isolate a specific formation mechanism for isolated dwarfs, while less restrictive definitions erase a link to the formation mechanism. Thus, how we define UDG populations must be considered if we want to understand the formation and evolution of UDGs.

2.1 Introduction

A significant population of very low surface brightness ($\mu_0 > 24$ mag arcsec $^{-2}$) dwarf galaxies with large effective radii (> 1.5 kpc) were detected in the Coma cluster by van Dokkum et al. in 2015 [211] and classified as “ultra-diffuse galaxies” (UDGs). While we have known of the existence of low surface brightness (LSB) galaxies for some time (see [212, 213, 214, 215, 216]), hundreds of these particularly diffuse galaxies have been discovered both in cluster environments [217, 218, 219, 220, 221] and isolated environments [222, 223, 224]. Though these galaxies generally have standard dwarf luminosities and metallicities [223, 225], their sizes are more comparable to those of L_* galaxies like the Milky Way. However, other studies argue that these galaxies consist of the extreme end of the continuum of LSBs [226], and that their sizes are consistent with those of standard dwarf galaxies when considering the expected location of the gas density threshold for star formation [227, 228].

The recent conclusion that UDGs are so ubiquitous has prompted questions about their formation. Do they originate in standard dwarf mass dark matter halos, or are they failed L_* mass galaxies within larger dark matter halos that for some reason failed to build up their stellar populations? Is their formation driven by internal processes, such as bursty star formation and supernova feedback, or external processes, such as tidal interactions and mergers? Or is it possible that multiple types of UDGs exist, driven by different formation mechanisms? The globular cluster content of UDGs has resulted in both constraining UDGs to live

in both ‘failed’ L_* dark matter halos [229, 230, 231] and also in standard dwarf galaxy dark matter halos [232, 233, 234]. Some measurements even indicate UDGs with largely undermassive dark matter halos [235, 236, 237].

Idealized simulations (e.g. [238, 239]), analytic and semi-analytic models (e.g. [240, 224, 241, 242]), and cosmological simulations (e.g. [243, 244, 245, 246, 247]) have all been utilized in order to better understand UDG formation, resulting in multiple channels for their formation, including: dynamical origins, with UDGs forming through tidal heating and/or stripping from interactions (e.g. [241, 245, 246]); bursty star formation and supernova feedback, resulting in extended, diffuse stellar distributions and UDG-like properties (e.g. [243, 244, 247]); ram pressure stripping, resulting in a extended, passively evolving stellar populations in cluster galaxies [248]; and, finally, mergers, resulting in isolated UDG progenitors with extended effective radii, high spin, and low central star formation [249].

The above demonstrates that theory predicts multiple formation channels for UDGs, though conclusions may limited by both physical models in simulations and limited statistics in observations. However, there is no consensus about what constitutes the ‘ultra-diffuse’ designation; the questions of ‘how dim’ and ‘how large’ are all answered differently by different groups. Some identify UDGs by the central surface brightness (e.g. [211, 230]), while others use the effective surface brightness (e.g. [243, 250]) or the average surface brightness within the effective radius (e.g. [217, 251, 247]). Many groups require the effective radii of UDGs to be larger than 1.5 kpc (e.g. [211, 251, 230]) while others only require them to be larger than 1 kpc (e.g. [243, 250]). The question then becomes: are we comparing

apples to apples? Is each group identifying the same population of galaxies as ultra-diffuse? Is this consistent across environment? If not, does it matter?

To further complicate this question, we can consider the orientation of the galaxy when fitting surface brightness profiles. While observers are limited to observing galaxies from Earth, it is standard practice in simulations to orient galaxies to face-on positions before identifying UDGs in order to maximize the sample size [243, 245, 246, 248, 249]. But what role does orientation play in identifying a UDG? Does this vary with environment? If a dependence on orientation exists, it would stem from the morphology of the galaxies. Intuitively, one would expect a largely spherical galaxy to appear roughly equivalent at all viewing angles, whereas a ‘disky’ galaxy’s appearance would be very dependent on orientation. As with the criteria for being “ultra-diffuse”, there is no cohesive understanding about the shapes of UDG populations. Some groups speculate that isolated UDGs favor a prolate morphology (e.g. [252, 245]), while others claim an oblate-triaxial morphology is preferred (e.g. [253, 254]). Identifying a cohesive shape distribution for UDGs could provide insights into how they evolve and what formation channels exist.

In this work, we study the populations of galaxies that common definitions of UDGs identify, and whether they are consistent across definitions. We also explicitly test what effect the orientation of galaxies has on the UDG populations in the ROMULUS25 and ROMULUSC simulations. Using the large sample of dwarfs and UDGs in the Romulus simulations, which contain varying environments from field to cluster, we have the ability to explicitly test the above questions. In

doing so, we demonstrate that the physical processes separating UDGs from the underlying dwarf population can be explicitly dependent on definition. Thus, it is imperative to consistently identify UDGs in order to solve the mystery of their origin.

The paper is organized as follows. In Section 2.2, we detail the ROMULUS simulations and our sample of 1249 resolved dwarf galaxies in isolated, satellite, and cluster environments, with anywhere from 354 to 990 UDGs (depending on how they are identified). In Section 2.3, we study the shapes of the dwarf galaxies in different environments, and the correlation between a galaxy’s shape evolution and its status as a UDG. In Section 2.4 we explore the effects of changing the UDG criteria and the galaxies’ orientations on the resultant UDG population and our results in Section 2.3. Finally, we summarize our findings in Section 2.5.

2.2 The Romulus Simulations

All galaxies analyzed in this work come from the ROMULUS25 [113] and ROMULUSC [114] simulations. These are high-resolution cosmological simulations run using CHANGA, an N -body+Smooth Particle Hydrodynamics (SPH) code [112]. CHANGA implements several physics models from its predecessor GASOLINE [255]; however, its improved SPH implementation allows for better capture of fluid instabilities through reduced artificial surface tension [106]. Physics below the resolution limit, such as stellar formation and feedback, as well as supermassive black hole (SMBH) growth and feedback, are governed by sub-grid prescriptions.

The ROMULUS25 simulation is a 25 Mpc-per-side uniform volume simulation. The simulated galaxies match important $z = 0$ scaling relations, including the stellar mass-to-halo mass relation [256] and the stellar mass-to-SMBH mass relation [257]. Furthermore, Tremmel et al. [113] demonstrated the simulation’s ability to produce realistic galaxies across four orders of magnitude in halo mass, ranging from dwarf galaxies resolved with over 10,000 particles to groups, while reproducing observations of high-redshift SMBH growth and star formation.

The ROMULUSC simulation is a cosmological zoom-in simulation of a galaxy cluster. At $z = 0$ the cluster has an R_{200} (the radius at which the enclosed density is 200 times the critical density of the universe) of 1033 kpc and an M_{200} (the mass enclosed within R_{200}) of $1.15 \times 10^{14} M_{\odot}$. The initial conditions for the cluster were extracted from a 50 Mpc-per-side uniform volume simulation using the renormalization technique of Katz et al. [258].

Both of the ROMULUS simulations are evolved to $z = 0$ with a Λ CDM cosmology ($\Omega_0 = 0.3086, \Lambda = 0.6914, h = 0.6777, and \sigma_8 = 0.8288$) following the Planck Collaboration [115]. Gravitational interactions are resolved with a spline force softening length of 350 pc, which is a Plummer equivalent of 250 pc, that converges to Newtonian force at 700 pc. The simulations oversample dark matter particles, such that the initial high-resolution dark matter particle count is 3.375 times that of the gas particles. This oversampling results in dark matter and gas particles with similar masses, $3.39 \times 10^5 M_{\odot}$ and $2.12 \times 10^5 M_{\odot}$ respectively. The similar particle masses aid in reducing the numerical effects from two-body scattering and energy equipartition, both of which can lead to spurious growth

in galaxy sizes within simulations [259]. The increased resolution in dark matter also gives the simulations the ability to track the dynamics of SMBHs within galaxies [260]. Additionally, the simulations are allowed more realistic treatment of weak and strong shocks [106] through an on-the-fly time-step adjustment and time-dependent artificial viscosity [261]. The sub-grid parameters have been optimized to create galaxies across a halo mass range of $10^{10.5-12} M_{\odot}$, and an updated implementation of turbulent diffusion [106] allows for the formation of a realistic metal distribution within galaxies [262] and the intracluster medium [263, 264, 114].

2.2.1 Sub-grid Physics and Star Formation

To approximate reionization effects, the ROMULUS simulations include a cosmic UV background [265] with self-shielding from Pontzen et al. [266]. The simulations implement primordial cooling for neutral and ionized H and He. This cooling is calculated from H and He line cooling [267], photoionization, radiative recombination [268, 269], collisional ionization rates [270], and bremsstrahlung radiation. Although the ROMULUS simulations are high resolution, they lack the ability to resolve the multiphase interstellar medium (ISM) or track the creation and annihilation of molecular hydrogen. It has been shown that simulating metal-line cooling at low resolution and without the presence of molecular hydrogen physics can lead to overcooling in spiral galaxies [271], thus the simulations do not include high-temperature metal-line cooling (see Tremmel et al. [114] for more details of this omission). Low-temperature metal-line cooling is implemented following

Bromm et al. [272].

Star formation (SF) in the ROMULUS simulations is a stochastic process governed by sub-grid models. In simulations of this resolution [273], SF is regulated by parameters that determine the physical requirements for gas to become star forming, the efficiency of the SF, and the coupling of supernova (SN) energy to the ISM:

- Gas must have a minimum density of $n_{\text{SF}} = 0.2 \text{ cm}^{-3}$ and a temperature of no greater than $T_{\text{SF}} = 10^4 \text{ K}$ in order to form stars.
- The probability p of a star particle forming from a gas particle with dynamical time t_{dyn} is given by:

$$p = \frac{m_{\text{gas}}}{m_{\text{star}}} (1 - e^{-c_{\text{SF}} \Delta t / t_{\text{dyn}}}) \quad (2.1)$$

where c_{SF} is the star-forming efficiency factor (here set to 0.15) and Δt is the formation timescale (here set to 10^6 yr).

- The fraction of the canonical 10^{51} erg SN energy coupled to the ISM is $\epsilon_{\text{SN}} = 0.75$.

When star particles are formed, they have a mass equivalent to 30% of the initial gas particle mass, i.e., $M_{\star} = 6 \times 10^4 M_{\odot}$, and represent a single stellar population with a Kroupa initial mass function [274]. Stars whose masses are in the range of 8-40 M_{\odot} undergo Type II SNe that are implemented using ‘blastwave’ feedback, following Stinson et al. [273]. The SN injects thermal energy into nearby gas particles, where the adiabatic expansion phase is replicated by temporarily

disabling cooling. Mass and metal diffusion into the ISM follow Shen et al. [262] and Governato et al. [164]. Stars whose masses exceed $40 M_{\odot}$ are assumed to collapse directly into a black hole.

The ROMULUS simulations include a novel implementation of black hole physics [275, 260, 113, 276, 277, 114]. To ensure that SMBHs are seeded in gas collapsing faster than the star formation or cooling time scales, they only form in regions of pristine ($Z < 3 \times 10^{-4} Z_{\odot}$ for ROMULUS25 and $Z < 10^{-4} Z_{\odot}$ for ROMULUSC), dense ($n > 15n_{SF}$), and cool ($9.5 \times 10^3 < T < 10^4$ K) gas. The seed mass is $10^6 M_{\odot}$ and most SMBHs form within the first Gyr of the simulation. An implementation of a dynamical friction sub-grid model [260] allows the tracking of SMBH orbits as they move freely within their host galaxies. The growth of SMBHs is modeled via a modified Bondi-Hoyle accretion formalism that accounts for gas supported by angular momentum. Feedback from an active galactic nucleus is approximated by converting a fraction (0.2%) of the accreted mass into thermal energy and distributing it to the surrounding gas particles.

2.2.2 Halo Identification

The ROMULUS simulations use the Amiga Halo Finder (AHF) [278] to identify dark matter halos, subhalos, and their associated baryonic content. AHF uses a spherical top-hat collapse technique to determine the each halo's virial mass (M_{vir}) and radius (R_{vir}), following a procedure similar to Bryan & Norman [279]. Halos are considered resolved if they have a virial mass of at least $3 \times 10^9 M_{\odot}$, corresponding to a dark matter particle count of $\sim 10^4$, and a stellar mass of at

least $10^7 M_{\odot}$, corresponding to a star particle count of ~ 150 , at $z=0$. Galaxies are considered to be resolved dwarf galaxies if they meet the above criteria, as well as have a stellar mass less than $10^9 M_{\odot}$. When calculating stellar masses, we use photometric colors, following Munshi et al. [111] to better represent the values inferred from typical observational techniques. In ROMULUSC, we identify a sample of 201 dwarf galaxies in a cluster environment. In ROMULUS25, we have a sample of 377 dwarf galaxies in a satellite environment, where a galaxy is classified as a satellite if its center is within the virial radius of a larger halo. While we implement no restrictions on the satellite-to-host mass ratios when determining satellites, a check of our satellite population at $z=0$ shows that we avoid considering any significant fringe cases, such as two nearly equivalent mass halos merging. Of our 377 satellites, only 19 have a satellite-to-host mass ratio greater than 1:10, and only three have a ratio greater than 1:3. We also identify a sample of 671 dwarf galaxies in an isolated environment in ROMULUS25. The criteria for being isolated follows from Geha et al. [280], and requires being neither a satellite of another halo nor within 1.5 Mpc of any galaxy with $M_{\star} > 2.5 \times 10^{10} M_{\odot}$. Galaxies are analyzed using PYNBODY [281] and tracked across time using TANGOS [282], both of which are publicly available.

2.2.3 UDG Identification

The process of identifying UDGs follows the previous studies of UDGs in the ROMULUS simulations [248, 249]. When analyzing a galaxy, we first orient it in a face-on position based on the angular momentum. This calculation is performed

on the gas particles within the inner 5 kpc of the galaxy, or the star particles when less than 100 gas particles are present. Once oriented, we generate azimuthally averaged surface brightness profiles with 300 pc sampling (the spatial resolution of the Romulus simulations). We generate profiles in Johnson B , V , and R bands, and calculate g -band surface brightness from the B and V bands, following Jester et al. [283]. We then fit a Sérsic profile through all points brighter than 32 mag arcsec $^{-2}$, the general depth of sensitive observations [284, 285]. The Sérsic profile is defined as

$$\mu(r) = \mu_{\text{eff}} + 2.5(0.868n - 0.142) \left(\left(\frac{r}{r_{\text{eff}}} \right)^{1/n} - 1 \right) \quad (2.2)$$

where $\mu(r)$ is the surface brightness at radius r , r_{eff} is the effective radius (half-light radius), μ_{eff} is the effective surface brightness (surface brightness at the effective radius), and n is the Sérsic index [286]. When fitting a Sérsic profile, we allow the effective surface brightness to range between 10 and 40 mag arcsec $^{-2}$, the effective radius to range between 0 and 100 kpc, and the Sérsic index to range between 0.5 and 16.5. In Section 2.4 we explore different definitions of UDGs, but we first adopt our fiducial definition in Section 2.3. For our fiducial definition, a halo is considered ultra-diffuse if its central g -band surface brightness is dimmer than 24 mag arcsec $^{-2}$ and its effective radius is larger than 1.5 kpc, following van Dokkum et al. [211].

2.3 Shapes of UDGs and Non-UDGs

To study the possible differences between UDG and non-UDG morphology in different environments, we analyzed the b/a and c/a axis ratios for all dwarf galaxies, which correspond to the major axis ratios when looking at the galaxies from face-on and edge-on orientations, respectively. Hence, a $b/a \approx c/a \approx 1$ would be a spherical distribution, a $b/a \gg c/a$ would be an oblate (or ‘disky’) distribution, and a $b/a \approx c/a < 1$ would be a prolate distribution. Axis ratios are derived from the eigenvalues of the shape tensor, which is calculated by dividing the moment of inertia tensor by the total mass. Shape tensors are generated using star particles that are separated into radial bins. The values presented in this work come from the stellar particle bin located at twice the half-light radius.

Figure 2.1 shows the stellar c/a axis ratios plotted against the stellar b/a axis ratios for dwarf galaxies in all environments at $z = 0$. In general, we see that the isolated galaxies reside closer to the lower right-hand corner of the plot, indicating a more disk-like structure. We find that in the cluster and satellite environments, the b/a and c/a axis ratios for UDGs are in good agreement with non-UDGs, but the isolated galaxies show a notable disparity between the two populations. In general, the isolated UDG population is more oblate than the underlying dwarf population.

Our results seem to contrast with those of Jiang et al. [245], who found that field UDGs are more prolate than non-UDGs. However, the low-mass non-UDG axis ratios from Figure 4 of Jiang et al. [245] ($b/a \approx .7$, $c/a \approx .414$) are well within

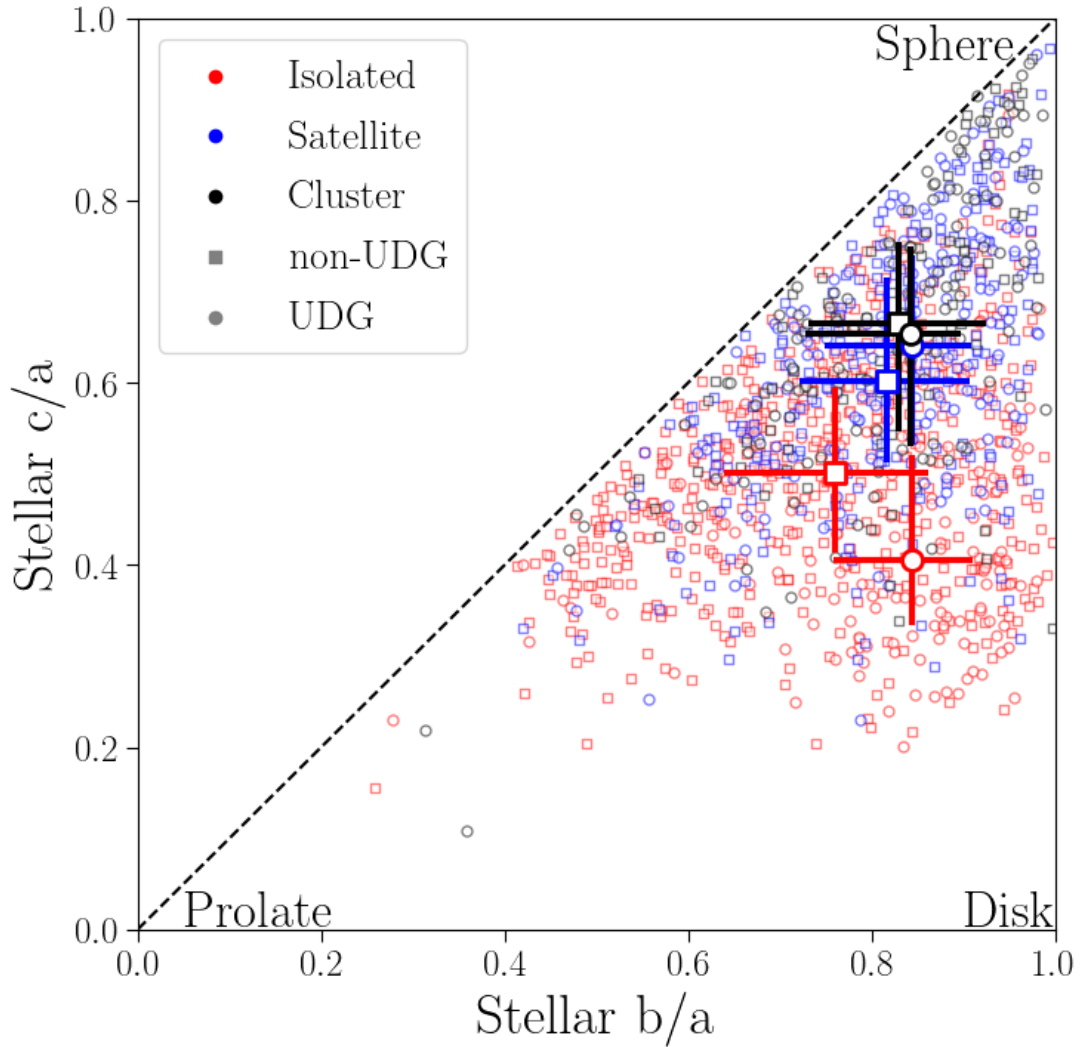


Figure 2.1: The c/a axis ratios plotted against the b/a axis ratios for the dwarf galaxies' stellar distributions at $z = 0$ in various environments. The populations are separated into UDGs and non-UDGs according to Section 2.2.3. The bold points represent the medians of the populations, while the error bars show the 25th to 75th percentiles. Isolated galaxies, in general, are ‘diskier’ in morphology than the satellite and cluster galaxies, though isolated UDGs are the most ‘disky’ population.

the errors of our isolated non-UDGs. While we are unsure why our UDG results differ, there are some probable causes that can be ruled out. In this work, we perform shape measurements using stellar particles in a bin around two half-light radii, while Jiang et al. [245] used all stellar particles within one half-light radius. However, if we calculate our shapes using a similar method, we still find that our isolated UDGs are more oblate than the non-UDGs. Another possible explanation for our differing results is the ROMULUS simulations’ inability to form cores. The ROMULUS simulations do not resolve the multiphase ISM, thus stars must be allowed to form in gas that is relatively diffuse. As a result, the galaxies lack the bursty, clustered central star formation required to produce feedback strong enough to create a core in the dark matter halo (e.g. Dutton et al. [287]). However, in performing our shape analysis on the “Marvel-ous Dwarfs” zoom simulations [116], we find results consistent with the isolated galaxies in ROMULUS, where UDGs are more oblate. The median (b/a , c/a) values are (0.85, 0.29) for UDGs and (0.8, 0.56) for non-UDGs, though we note our zoom simulations contain only four UDGs. Since the “Marvel-ous” suite has the resolution to form cores, this suggests that core formation (or the lack thereof) is not influencing our shape analysis in ROMULUS. We note, however, that a recent study by Kado-Fong et al. [254] found that the inferred three-dimensional (3D) shapes of observed LSB galaxies are well characterized by oblate spheroids, with c/a values higher than those of high-mass dwarfs with thick disks. The LSB galaxies in the ROMULUS simulations (defined as having $r_{\text{eff}} > 1$ kpc and $\bar{\mu}_{\text{eff,g}} > 24.3$ mag arcsec $^{-2}$) were found to be in good agreement with the observations (see Figure 8 in Kado-Fong

et al. [254]).

This disparity in the isolated UDG and non-UDG morphologies suggests that the two populations have different formation histories. Wright et al. [249] found that isolated dwarfs in ROMULUS25 all undergo similar numbers of mergers, both major and minor, and that UDGs are primarily the products of early (> 8 Gyr ago) major mergers. Here we consider what effect this has on the shape evolution of the isolated galaxies. Figure 2.2 shows the stellar b/a and c/a axis ratios for the isolated galaxies as a function of the time elapsed since a galaxy’s last major merger. A time of $t = 0$ represents the time of a halo’s final major merger, with a time of $t < 0$ being the time preceding the final merger, and a time of $t > 0$ being the time elapsed since the merger. The time $t = 0$ is chosen to be the instant that the virial radii of the merging halos first overlap, following Hetznecker et al. [288], and only time bins with at least five data points are plotted. The bold lines represent the populations’ median values, while the shaded regions cover the 25th to 75th percentiles. Additionally, the galaxies are split into columns according to stellar mass. This binning, following Wright et al. [249], separates our population into dependencies on UDG criteria, with the low-mass bin (149 galaxies) being largely dependent on effective radius only, the high-mass bin (298 galaxies) being dependent on central surface brightness only, and the intermediate-mass bin (224 galaxies) being dependent on both. Note that all of the UDGs in the high-mass bin, and most of the other UDGs, undergo their last major merger (LMM) within the first 5 Gyr of the simulation, while the LMMs for non-UDGs are much more spread out in time. After their LMMs, both UDGs and non-UDGs experience a

gradual increase in b/a . Since UDGs more typically have early LMMs, this could result in a $z = 0$ b/a disparity between dwarfs and UDGs, as seen in Figure 2.1. However, when scaling to LMM time, we see that intermediate- and high-mass UDGs still evolve to higher b/a values than even their early-merging non-UDG counterparts, suggesting that something in addition to early mergers is driving a change in shapes. The divergence from this trend in the lowest mass bin is likely a combination of overquenching due to resolution effects and these galaxies being genuinely dispersion-supported.

While UDGs are more likely to experience earlier LMMs, this does not fully explain the discrepancy in shapes. This is consistent with Wright et al. [249], who found that while isolated UDGs were largely influenced by early mergers, that alone was not sufficient to explain their formation. In fact, Wright et al. [249] found that the mergers were not only earlier on average, but also tended to produce a larger increase in specific angular momentum. In Figure 2.3, we examine the evolution in halo spin, now also splitting the galaxy population based on early- and late-time mergers. Here the spin parameter is the Bullock spin [55]. Examining the early mergers (top row), we find that mergers that result in intermediate and massive UDGs at $z = 0$ have more angular momentum, which results in a significant increase in halo spin beginning at the last major merger. Galaxies that experience LMMs also see an increase in spin, but this is much less likely to produce a UDG at $z = 0$. We find that UDGs experience less of an increase in c/a post-LMM; however, we note that the slight difference in the c/a shape post-LMM may be attributed to the differences in spin of UDG and

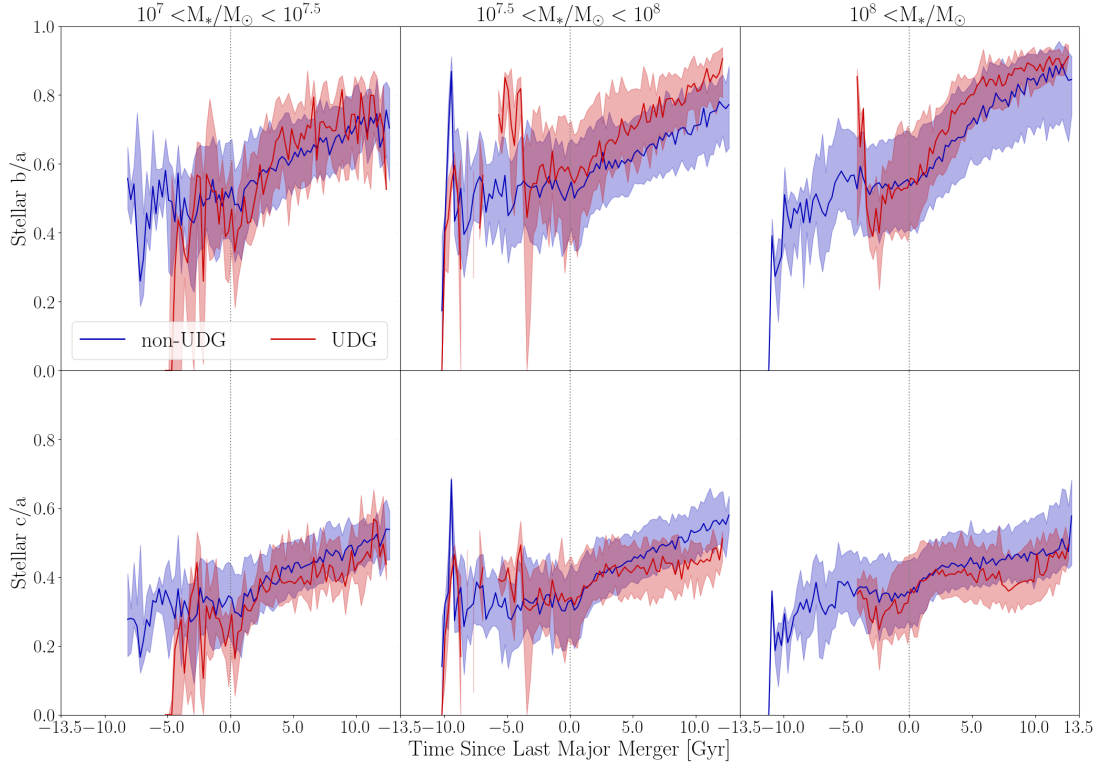


Figure 2.2: The isolated galaxies’ stellar b/a and c/a axis ratios as a function of the time elapsed since their final major merger ($t = 0$). The shaded regions represent the 25th to 75th percentiles of the UDG (red) and non-UDG (blue) populations. Only time bins with at least five data points are plotted. Intermediate- and high-mass UDGs evolve to higher b/a values and lower c/a values than their non-UDG counterparts.

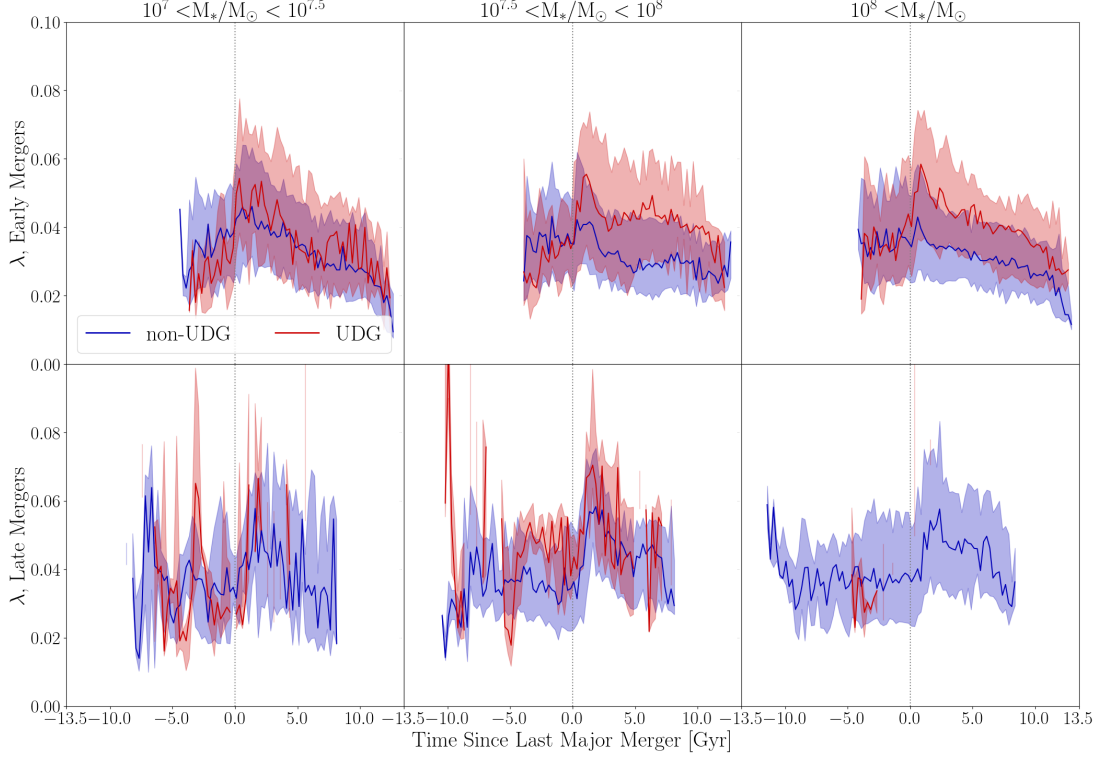


Figure 2.3: The spin parameter, λ , for isolated galaxies separated into UDGs and non-UDGs for the fiducial definition. The top row contains galaxies that finished merging within the first 5 Gyr of the simulation, while the bottom row contains galaxies with major mergers after 5 Gyr. The shaded regions represent the 25th to 75th percentiles. Only time bins with at least five data points are plotted. Intermediate- and high-mass, early-merging UDGs evolve to higher spin values after merging. While intermediate- and high-mass late-merging galaxies evolve to similarly high spins, they do not typically result in UDGs.

non-UDG LMMs. Thus, we confirm that the combination of early and high-spin mergers is required to form isolated UDGs, as demonstrated in Wright et al. [249], and that this is the driving force behind the difference in shapes between isolated UDGs and isolated dwarfs. To summarize: we show that post-LMM, a dwarf galaxy’s b/a value increases as the galaxy relaxes, such that those with earlier mergers (UDGs) have larger b/a values by $z = 0$ (see Fig. 2.2). For UDGs, c/a remains lower for UDGs when compared to dwarf galaxies because their mergers have higher spin (see Figs 2.2 and 2.3). As such, we predict that observations of stellar shape can be used to identify the major merger history of dwarf galaxies and a formation channel for UDGs (early, high-spin mergers).

2.4 Effects of Changing Definition and Orientation

In Section 2.3, we showed how the unique formation mechanism for isolated UDGs identified in Wright et al. [249] leads to differences in UDG and non-UDG morphology. During our study, we found that using alternate UDG criteria can cause these differences to disappear, removing any indication of the underlying formation mechanisms. To study the effect that the UDG definition has on both the above results and the resultant UDG population as a whole, we analyze our dwarf sample using multiple sets of UDG criteria.

2.4.1 Definitions of UDGs

To illustrate this point, we consider five different definitions of UDGs. Each of these definitions are used in the recent literature, and are summarized in Table

2.1:

- **G0-F**: this definition comes from van Dokkum et al. [211]. It requires the central g -band surface brightness to be fainter than $24 \text{ mag arcsec}^{-2}$ and the effective radius to be larger than 1.5 kpc. While performing the Sérsic fits for this definition, we allow the Sérsic index to vary as a free parameter. This is the definition outlined in Section 2.2.3 and used in the results presented in Section 2.3.
- **G0-1**: this definition is the same as G0-F, but when performing the Sérsic fits, the Sérsic index is fixed at a value of 1, keeping in line with the original method in van Dokkum et al. [211].
- **R0**: this definition comes from Forbes et al. [230]. It requires the central R -band surface brightness to be fainter than $23.5 \text{ mag arcsec}^{-2}$ and the effective radius to be larger than 1.5 kpc. While performing the Sérsic fits for this definition, we allow the Sérsic index to vary as a free parameter.
- **RE**: this definition comes from Di Cintio et al. [243]. It requires the effective R -band surface brightness to be fainter than $23.5 \text{ mag arcsec}^{-2}$ and the effective radius to be greater than 1 kpc. Additionally, the authors require the R -band absolute magnitude to be within -16.5 to -12. While performing the Sérsic fits for this definition, we allow the Sérsic index to vary as a free parameter. We note that the authors define the effective surface brightness as $L/(2\pi r_{\text{eff},R}^2)$ rather than $\mu_R(r_{\text{eff}})$ (the value returned by the Sérsic fit), so we adopt this method as well when identifying UDGs with this definition.

Using $\mu_R(r_{\text{eff}})$ results in a slight increase in the obtained value for μ_{eff} (≈ 1 mag arcsec $^{-2}$), but only results in a slight difference in the number of UDGs ($\approx 0 - 4\%$ of each environment's populations) and has no bearing on the results of this work.

- **R̄E:** this definition comes from van der Burg et al. [219]. It requires the average R -band surface brightness within the effective radius to be between 24-26.5 mag arcsec $^{-2}$ and the effective radius to be larger than 1.5 kpc. While performing the Sérsic fits for this definition, we allow the Sérsic index to vary as a free parameter.

2.4.2 Definition Effects

The numbers of galaxies that are identified as UDGs are given in Table 2.2 for each environment and definition. The process of identification follows from Section 2.2.3 for each definition (i.e., we first orient each galaxy to a face-on position, before exploring orientation effects below), with the appropriate size and surface brightness restrictions applied. Regardless of definition, the percentage of dwarf galaxies that would be identified as UDGs generally increases with the density of the environment. This trend with environment matches the predictions from Martin et al. [247] using the Horizon-AGN simulation [289]. The authors found that UDGs (here defined as $\langle \mu_R(r_{\text{eff}}) \rangle > 24.5$) represent a significant percentage of the galaxy population, and this percentage increases with environmental density. These results also agree with those from Jackson et al. [290], who found that

Table 2.1: A summary of the UDG definitions considered

Name	Surface Brightness ($\frac{\text{mag}}{\text{arcsec}^2}$)	r_{eff} (kpc)	Sérsic Index
G0-F	$\mu_g(0) > 24$	$r_{\text{eff}} > 1.5$	Free
G0-1	$\mu_g(0) > 24$	$r_{\text{eff}} > 1.5$	$n = 1$
R0	$\mu_R(0) > 23.5$	$r_{\text{eff}} > 1.5$	Free
RE	$\mu_{\text{eff},R} > 23.5$	$r_{\text{eff}} > 1$	Free
R \bar{E}	$26.5 > \langle \mu_R(r_{\text{eff}}) \rangle > 24$	$r_{\text{eff}} > 1.5$	Free
Name	Absolute Magnitude	Reference	
G0-F	N/A	van Dokkum et al. [211]	
G0-1	N/A	van Dokkum et al. [211]	
R0	N/A	Forbes et al. [230]	
RE	$-12 > M_R > -16.5$	Di Cintio et al. [243]	
R \bar{E}	N/A	van der Burg et al. [219]	

UDGs exist in large numbers in groups and the field within the NewHorizon Simulation [291], as well as agreeing with observational results (e.g. van der Burg et al. [292]).

Although the trend with environment is ubiquitous across most definitions, the total number of UDGs identified is not. The G0-F and R0 definitions are much more restrictive in their UDG identification compared to the RE definition, which identifies the largest population of UDGs in all environments. The G0-1 and R \bar{E} definitions tend to fill in the middle ground between the G0-F/R0 and RE definitions in terms of the size of the UDG populations.

2.4.3 Orientation Effects

Since all of our definitions of UDGs are derived from surface brightness profiles, a galaxy's status as a UDG is intrinsically dependent on its viewing orientation. It is standard practice when searching for UDGs within simulations to first orient the galaxy to a face-on position [243, 248, 249]. This, in theory, will maximize the galaxy's effective radius while minimizing its central surface brightness, optimizing its likelihood of being identified as a UDG. Here, we study whether this assumption holds true for all galaxies, and how a galaxy's orientation could affect its status as a UDG. Some previous studies (e.g. [244, 290, 250]) have considered multiple viewing angles (such as the three primary axes or a span of inclinations), but here we consider 288 positions from incremental rotations over two axes perpendicular to the line of sight (see Figure 2.5 for a visual guide). These positions, in their entirety, detail how the galaxy is viewed from any position in 3D space.

Table 2.2: The number of galaxies that are identified as UDGs at face-on orientation for each environment and UDG definition. The counts are also given as a fraction of the environment’s total dwarf population with Poisson error.

Definition	Environment	$N_{\text{UDG,faceon}}$	Percentage
G0-F	Isolated	134	19.97 ± 1.73
	Satellite	142	37.67 ± 3.16
	Cluster	122	60.70 ± 5.50
G0-1	Isolated	241	35.92 ± 2.31
	Satellite	230	61.01 ± 4.02
	Cluster	167	83.08 ± 6.43
R0	Isolated	125	18.63 ± 1.67
	Satellite	125	33.16 ± 2.97
	Cluster	104	51.74 ± 5.07
RE	Isolated	454	67.66 ± 3.18
	Satellite	309	81.96 ± 4.66
	Cluster	168	83.58 ± 6.45
$\bar{\text{RE}}$	Isolated	194	28.91 ± 2.08
	Satellite	180	47.75 ± 3.56
	Cluster	132	65.67 ± 5.72

As we describe in Section 2.2.3, when analyzing a galaxy, we first orient it to a face-on position. After the initial orientation, the galaxy is then rotated by an angle θ around an axis perpendicular to the line of sight (the angular momentum vector in the face-on position). Next, the galaxy is rotated by an angle ϕ around the axis perpendicular to the line of sight and previous axis of rotation. An azimuthally averaged surface brightness profile for the galaxy is generated and fit with a Sérsic profile that is used to determine whether the galaxy is identified as a UDG at the given orientation. The θ -rotations and ϕ -rotations considered in this work span the spaces of $[0^\circ, 180^\circ)$ and $[0^\circ, 360^\circ)$, respectively, both in increments of 15° . Since the radial surface brightness profile of a galaxy is unaltered under rotations around the line of sight, any (θ, ϕ) where $\theta < 180^\circ$ is analogous to a rotation of $(180^\circ + \theta, 180^\circ - \phi \text{ [mod}360\text{]})$ where $[\text{mod}360]$ (modulo 360°) means that if $180^\circ - \phi = -x < 0$, the value becomes $360^\circ - x$. Thus, the θ (ϕ) rotation space of $[180^\circ, 360^\circ)$ ($[0^\circ, 360^\circ)$) is bijectively mapped to the $[0^\circ, 180^\circ)$ ($[0^\circ, 360^\circ)$) space, and we have analyzed all unique positions. The top panel of Figure 2.4 illustrates the rotations considered in this work using a flat, circular disk.

The numbers of galaxies that are identified as UDGs when considering any orientation are given in Table 2.3 for each environment and definition. The percentages of dwarf galaxies that are UDGs still increase with environmental density, but the numbers of UDGs have increased by a significant margin in almost every case. The value Δ in Table 2.3 represents the number of UDGs gained when considering orientations other than face-on, i.e. the number of galaxies that are *not* classified as a UDGs at a face-on orientation but *are* classified as such at some

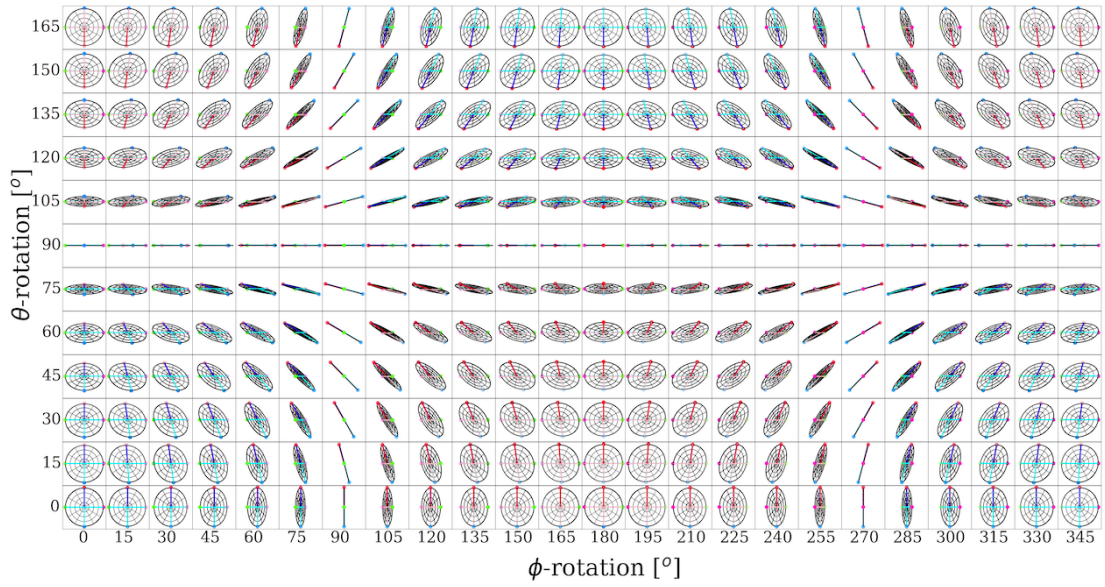


Figure 2.4: A visual representation of the rotated galaxy positions considered in this work. The sample ‘galaxy’ is a flat, circular disk with one face blue and the opposite face red. The disk has a single dark-colored radius and multicolored vertices to help visualize the rotations.

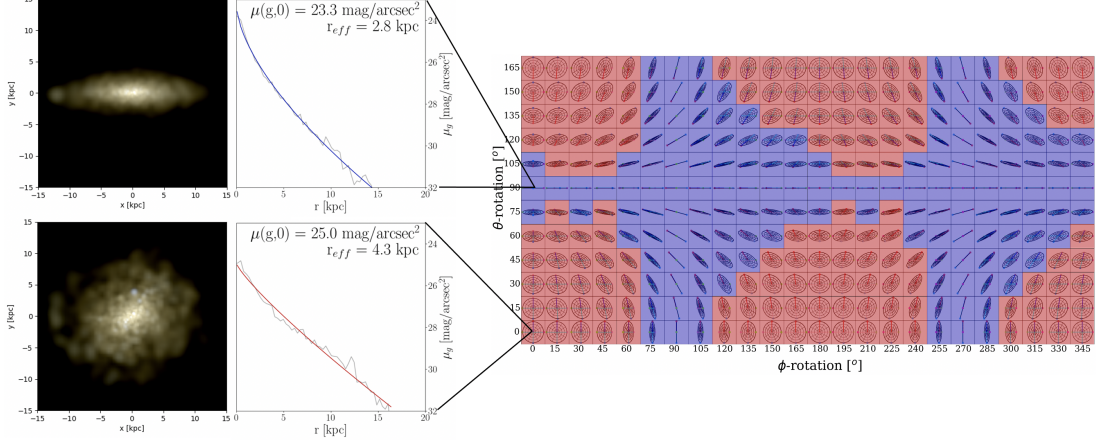


Figure 2.5: **Right:** an example of the rotation-dependent UDG status of an isolated galaxy from ROMULUS25 with $M_\star = 3.26 \times 10^8 M_\odot$. The grid shows whether the galaxy is identified as a UDG (red) or a standard dwarf (blue) at the given rotation under the G0-F definition. **Left:** example g -band surface brightness profiles and their associated Sérsic fits of the isolated galaxy for (θ, ϕ) rotations of $(0^\circ, 0^\circ$; i.e., face-on) and $(90^\circ, 0^\circ$; i.e., edge-on). The fit parameters are given in the upper right-hand corners of the surface brightness plots. To the left of the plots are UVI images of the galaxy at the two orientations showing all features brighter than 32 mag arcsec $^{-2}$ (the region being fit by the Sérsic profile).

other orientation. Although this value decreases with environmental density, it is present in all definitions, indicating that by analyzing all galaxies in a face-on position, one is likely to omit a significant fraction of the galaxies that could potentially be identified as UDGs. This fraction can be quite large in the isolated environment, ranging from 7-20% of isolated dwarf galaxies, but is more minor in the denser environments, ranging from 2-17% in satellites and 0-13% in the cluster. This also hints at isolated galaxies' classifications as UDGs being more sensitive to orientation, a result we would expect, based on their more “disky” morphology, seen in Figure 2.1.

To further investigate whether isolated UDGs are less robust to orientation, we look at the different environments' total UDG populations at each specific orientation. Figure 2.6 summarizes these results with a color grid for each environment and UDG definition. Each point on the grid represents the total number of galaxies that are identified as ultra-diffuse at that orientation as a fraction of the total number of UDGs in that environment ($N_{\text{UDG,any}}$ from Table 2.3). In all definitions, the isolated UDG populations demonstrate much stronger orientation dependence than their denser-environment counterparts. The more restrictive definitions, G0-F and R0, show the strongest orientation dependence, with the percentages varying by $\sim 55 - 60\%$ in the isolated environment. In contrast, the least restrictive definition, RE, also appears to be the least orientation-dependent, with the percentages varying by $\sim 15\%$ in the isolated environment and essentially 0% in the cluster environment (there are only two cluster galaxies that are identified as RE-UDGs at some orientations, but not all). The RE definition,

Table 2.3: The number of galaxies that are identified as UDGs at any orientation for each environment and UDG definition. The number is also given as a fraction of the environment’s total dwarf population with Poisson error. The value $\Delta_{\text{face-on}}$ is the fraction of UDGs that were not identified using the face-on orientation, as used in Table 2.2.

Def.	Env.	$N_{\text{UDG,any}}$	Percentage	$\Delta_{\text{face-on}} (\%)$
G0-F	Isolated	191	28.5 ± 2.1	29.5
	Satellite	186	49.3 ± 3.6	23.7
	Cluster	148	73.6 ± 6.1	17.6
G0-1	Isolated	379	56.5 ± 2.9	36.4
	Satellite	293	77.7 ± 4.5	21.5
	Cluster	186	92.5 ± 6.8	10.2
R0	Isolated	197	29.4 ± 2.1	36.5
	Satellite	176	46.7 ± 3.5	28.0
	Cluster	129	64.2 ± 5.7	19.4
RE	Isolated	502	74.8 ± 3.3	10.0
	Satellite	320	84.9 ± 4.7	3.4
	Cluster	168	83.6 ± 6.5	0.0
$R\bar{E}$	Isolated	260	38.8 ± 2.4	25.4
	Satellite	224	59.4 ± 4.0	19.6
	Cluster	155	77.1 ± 6.2	14.8

in general, seems to be identifying the highest fraction of dwarf galaxies as UDGs at all orientations, which is expected from its Δ values in Table 2.3 being the smallest (especially when considering that the RE $N_{UDG,any}$ values were typically larger than those for other definitions). Again, the G0-1 and $R\bar{E}$ definitions seem to fill out the middle ground, both in terms of orientation dependence and the average percentage of UDGs retained across orientations. In all cases, the UDG populations are maximized in the positions that are more face-on than edge-on. This suggests that if simulators were to analyze all galaxies from the same orientation in order to identify UDGs, choosing face-on would likely produce the largest UDG population, but we have shown that allowing for any orientation will produce the maximum possible number of UDGs.

In addition to studying how the statistics of UDG populations vary with orientation, we analyze how the individual galaxies vary under rotation with each definition, as well as how the definitions change the populations of galaxies identified as ultra-diffuse. Figure 2.7 shows this analysis for the G0-F, $R\bar{E}$, and RE definitions (the R0 and G0-1 definitions are approximated here by the G0-F and $R\bar{E}$ definitions, respectively). The top row shows the normalized distributions of individual galaxies' UDG percentages, i.e., what percentage of the time a galaxy would be identified as a UDG if its orientation were drawn at random ($\cos(\theta)$ uniform in $[-1,1]$ and ϕ uniform in $[0,2\pi]$). In the G0-F and $R\bar{E}$ definitions, the isolated galaxies tend to occupy the low-percentage space, particularly 0-15%, while a large fraction of satellite and cluster galaxies occupy the 95-100% bin. The $R\bar{E}$ definition shows very similar results to the G0-F definition, but sees some

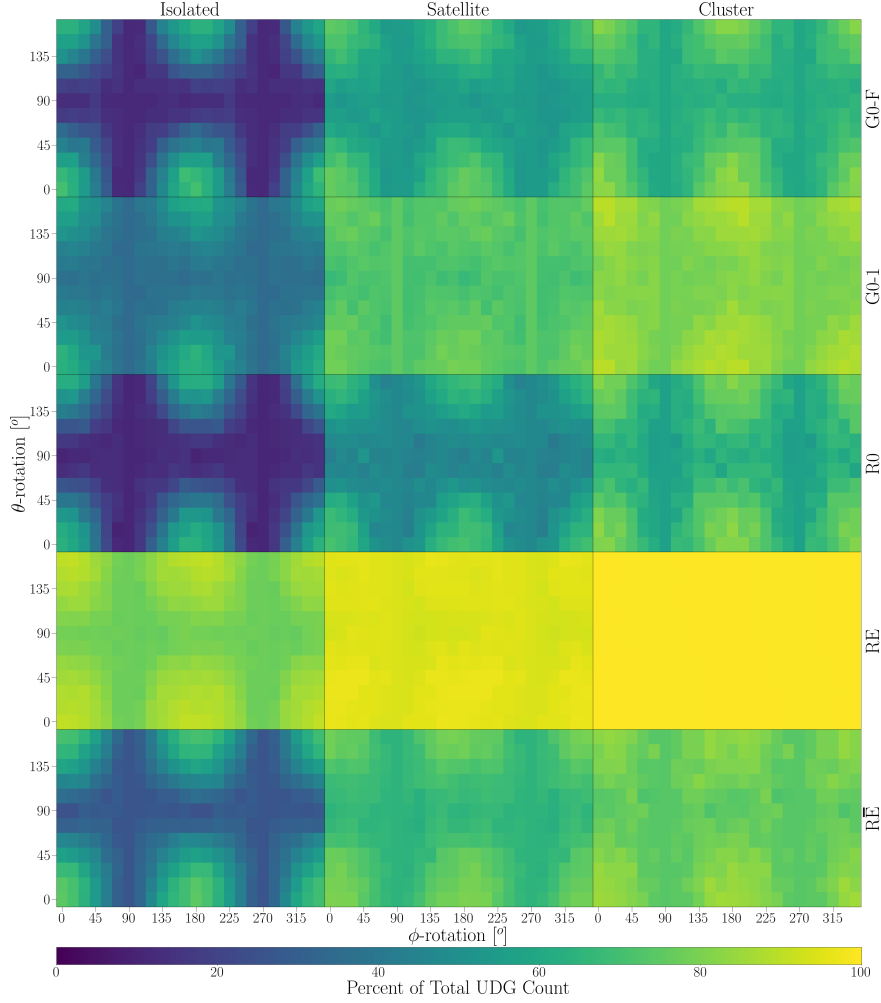


Figure 2.6: Color grids representing the UDG populations for each environment and definition of UDG. Each point on the grid represents the UDG population at that particular orientation. The value plotted is the number of galaxies that are identified as UDGs at that orientation as a percentage of the total number of galaxies that are identified as UDGs at any orientation (i.e., the “Total UDG Count” for that environment and definition). In all environments and definitions, the UDG count increases as you move from edge-on positions to face-on ones. In each definition, there is the most rotation dependence (color contrast) in the isolated environment and the least in the cluster environment.

galaxies in all environments shift from the lower percentages to the higher ones.

In contrast, the RE definition sees most galaxies in all environments occupying the 95-100% bin, mirroring the lack of orientation dependence seen in Figure 2.6. This implies that if a galaxy is identified as a UDG by the RE definition at some orientation, it is likely to be identified as such at any orientation.

The bottom row shows all of our dwarfs in surface brightness versus effective radius space with their face-on values. Also shown are the boundaries for UDG classification. The RE definition, while being the most robust to orientation, demarcates the largest area of our dwarf population as ultra-diffuse. A large number of galaxies are not identified as RE-UDGs only because they violate the absolute magnitude restriction.

Using the individual galaxies' UDG percentages, we can construct mass functions. Figure 2.8 shows the UDG mass functions for each environment using the G0-F definition, assuming each galaxy is oriented randomly. Rather than using the binary choice of UDG or non-UDG (adding a 1 or 0 to the mass function), a galaxy's contribution is determined by its UDG percentage (the value plotted in the top row of Figure 2.7) and the resultant mass function is normalized to the size of the environment's dwarf population. The dotted lines are the ‘maximum’ mass functions, representing the idealized situation where every galaxy that could be identified as a UDG at some orientation is counted. The bottom plot shows the fraction of the maximum mass function that is occupied by the random orientation mass function. In the isolated and cluster environments, the N/N_{\max} percentage is relatively constant between 10^7 and $10^8 M_{\odot}$, after which it starts to decrease.

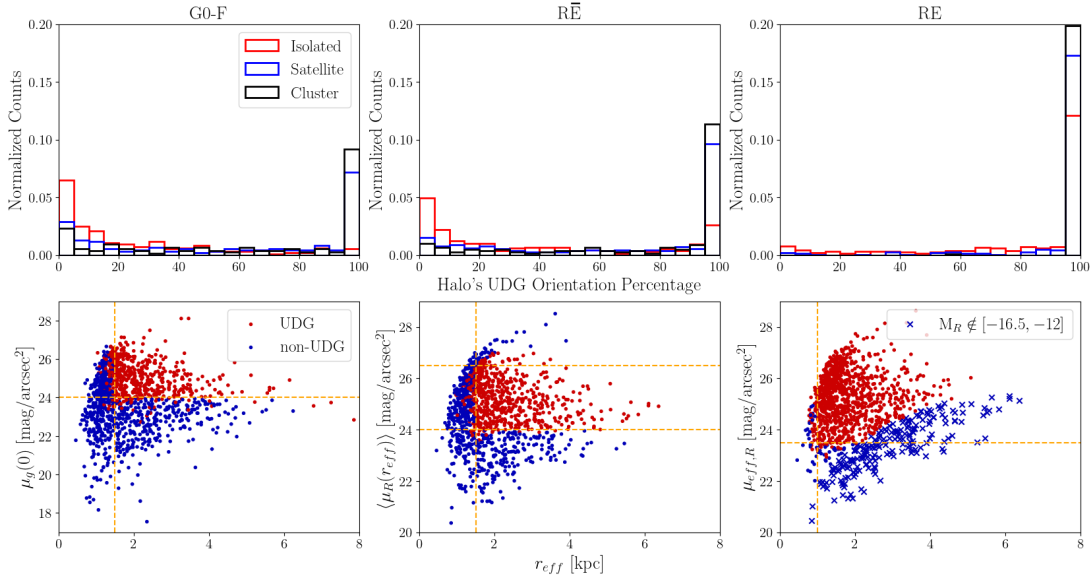


Figure 2.7: **Top:** normalized histograms of what percentage of the time a galaxy would be identified as a UDG when oriented randomly. Galaxies that are never considered ultra-diffuse are not included. From left to right, the UDG definitions used were G0-F, \bar{R} , and RE. In the G0-F definition (the most restrictive), a large number of galaxies in all environments exist in the 0-20% bins, indicating a high rotation dependence. In the RE definition (the least restrictive), most galaxies exist in the 95-100% bin, indicating little to no rotation dependence. **Bottom:** surface brightness versus effective radii plots, including dotted lines marking the selection criteria for UDGs. Galaxies are plotted using their face-on values. Points labeled as UDG (red) are those that are identified as such at any orientation, while points labeled as non-UDG (blue) are never classified as such. As above, the UDG definitions used were G0-F, \bar{R} , and RE. The blue “X”s denote galaxies that violate the R -band absolute magnitude restriction under the RE definition.

The satellite fraction steadily increases until $3 \times 10^8 M_\odot$ where the sample size approaches zero. When switching from the maximum mass function to one that accounts for random orientations, we see the greatest difference in the isolated UDGs, as demonstrated in the bottom panel of Figure 2.8. This is consistent with our shape results: compared to the cluster and satellite UDGs, isolated UDGs have a less spherical shape (more oblate), which implies that orientation will alter their classification. The more spherical populations are more robust to this, again as demonstrated in the bottom panel of Figure 2.8. None of the environments yield perfectly spherical populations, thus all populations have mass functions that depend on rotation. This is important to consider when comparing simulations to observations. Since simulations typically assemble their UDG populations from face-on analysis, it may not be appropriate to compare the resultant UDG mass function to one from observations, where galaxies are oriented randomly.

Recognizing that 3D shape may not be readily apparent in observations, we have also constructed ellipticity functions for all of our galaxies at random orientations. For each galaxy, a mock ellipsoid with the galaxy's b/a and c/a axis ratios is generated at a randomly selected orientation. The ellipsoid is then projected into a two-dimensional (2D) plane, and the projected ellipticity ($1-b/a$) (where a and b are now the projected major and minor axis ratios, respectively) is measured for the resultant ellipse traced out by the edge of the projection.

Figure 2.9 shows the median normalized ellipticity functions for all of our galaxies for 100 random orientations. The sample is split into mass bins (as with Figures 2.2 and 2.3), and a galaxy's status as UDG is determined at that particular

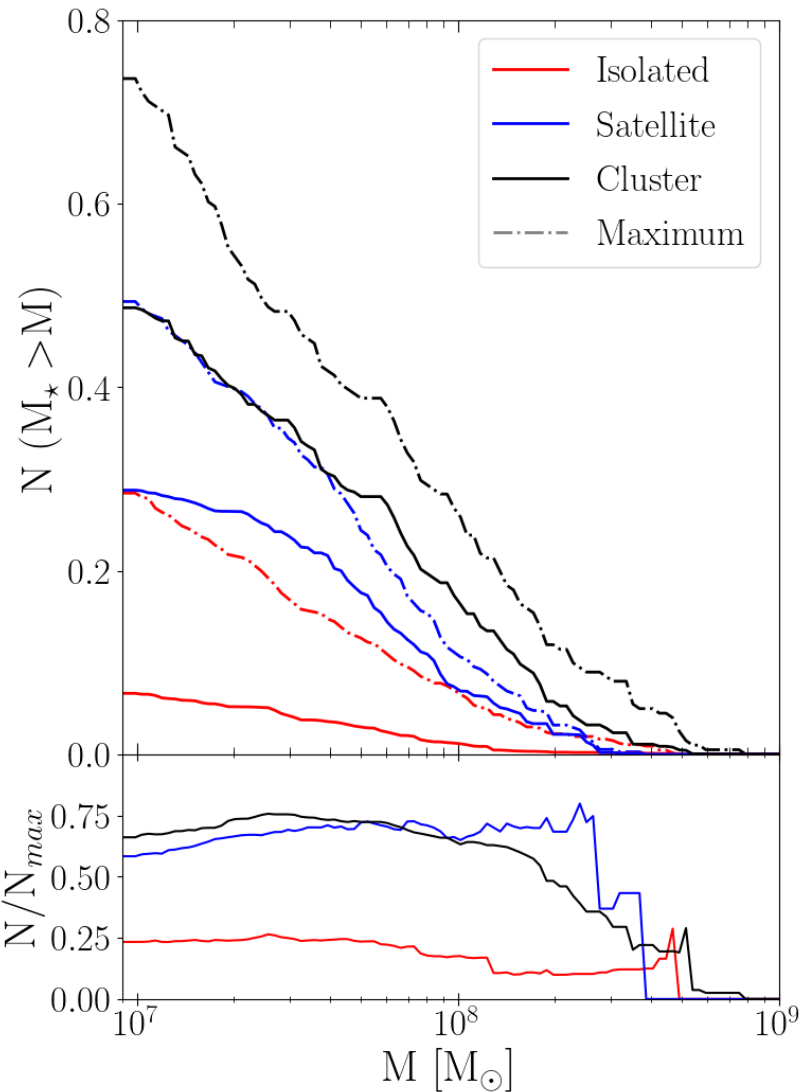


Figure 2.8: **Top:** the mass functions for G0-F-UDGs when all dwarfs are oriented randomly, normalized to the size of the environment’s dwarf population. The dotted lines are the maximum situation where every galaxy that could be identified as a UDG is oriented as such. **Bottom:** the UDG mass functions for randomly oriented galaxies divided by the maximum number mass function for each environment. The difference between the maximum and random orientation functions is largest in the isolated environment, where the UDGs are most rotation-dependent.

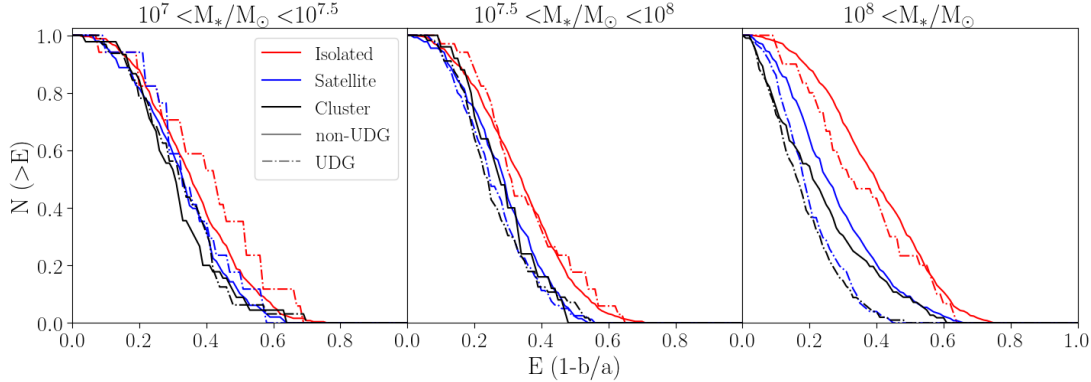


Figure 2.9: Normalized ellipticity functions for 2D projections of our galaxies at random orientations. The trends shown are the median values after 100 iterations of random orientations. We do not expect that measurements of 2D ellipticity will show the shape disparity between isolated UDGs and non-UDGs.

random orientation. In the intermediate- and high-mass bins, the difference in the distributions of isolated UDGs and non-UDGs is quite small, though the direction of the trends is the same as in our 3D results. The combination of our previously discussed orientation effects, along with the projection from 3D to 2D erase some of the shape difference we see in Section 2.3. We conclude that it may be difficult to use measurements of 2D ellipticity to infer a difference in isolated UDG and non-UDG morphologies. However, methods for obtaining 3D shapes, akin to those in Kado-Fong et al. [254], are promising avenues for inferring 3D shapes and thus confirming the shape differences we predict.

2.4.4 Effects on Previous Results

We have shown that altering the criteria for UDGs and accounting for different orientations can have a large effect on the resultant UDG population. This

effect means that various groups studying UDGs under varying definitions could potentially be looking at vastly different populations. This could make reaching a cohesive understanding of UDGs (including formation mechanisms and whether they exclusively reside in dwarf dark matter halos) difficult, if not impossible.

As an example: in Section 2.3, we found a disparity between isolated UDG and non-UDG morphologies that, after investigation, revealed the formation mechanism of early, high-spin mergers. This disparity, highlighted in Figure 2.1, was present when identifying UDGs according to the G0-F definition. However, recreating Figure 2.1 under the different definitions can provide drastically different results. Figure 2.10 shows the c/a versus b/a axis ratios for the dwarf halos with UDGs identified via the RE definition. We see now that the isolated galaxies show no disparity between UDGs and non-UDGs, with their medians and percentiles lying nearly on top of one another. Together, Figures 2.7 & 2.10 indicate that the RE definition is permissive to the extent that the UDG and non-UDG populations are effectively homogenized, thus no underlying formation mechanisms or physics would be unique to the UDG population.

2.5 Conclusions

We have selected 1249 dwarf galaxies in isolated, satellite, and cluster environments from the ROMULUS25 and ROMULUSC simulations. We analyze the shapes of these galaxies as well as the resultant UDG population under five definitions and 288 orientations. Our results can be summarized as follows:

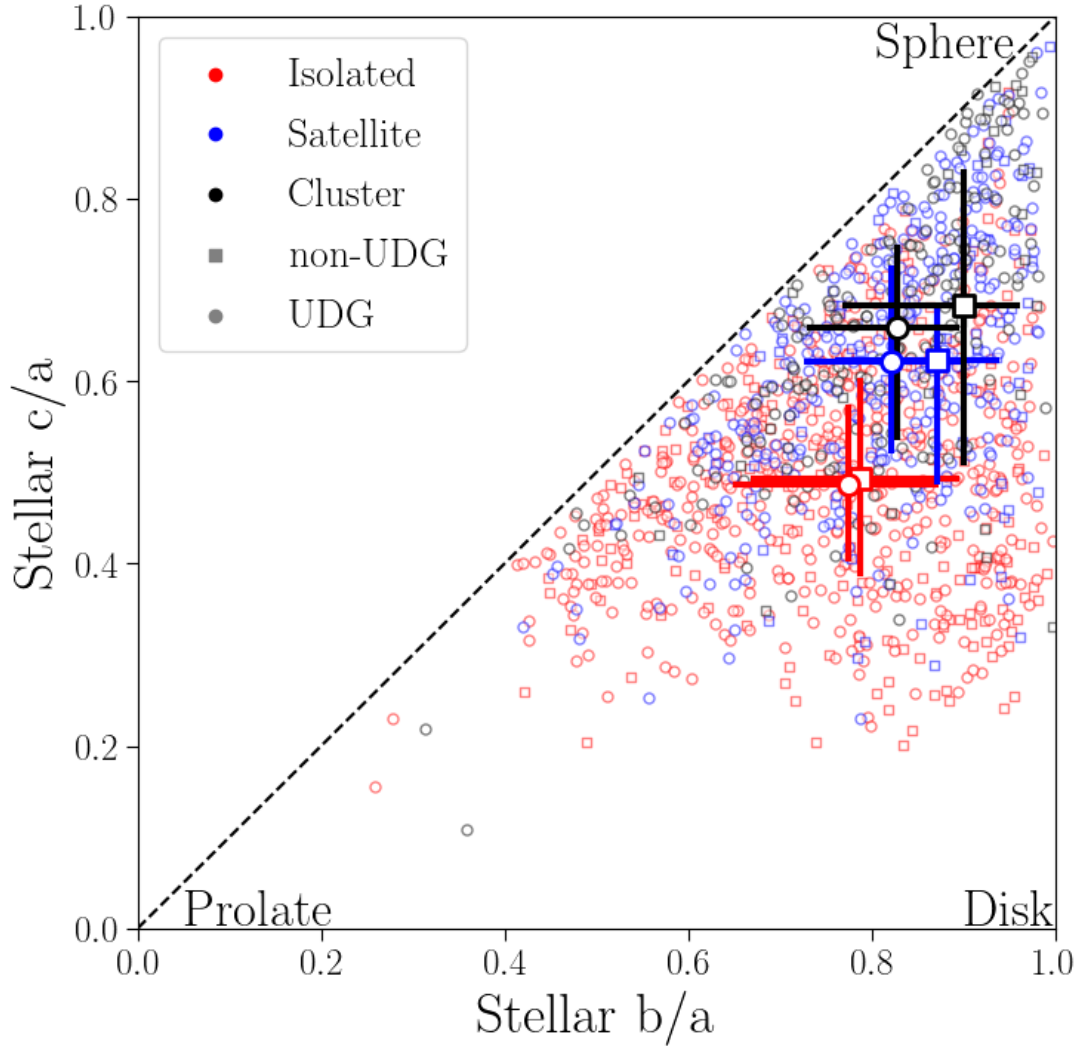


Figure 2.10: The stellar c/a axis ratios plotted against the b/a axis ratios for the galaxies' stellar distributions at $z = 0$ in all environments. The populations are separated into UDGs and non-UDGs under the RE definition. The bold points represent the medians of the populations, while the error bars show the 25th to 75th percentiles. Under the RE definition, the disparity in isolated UDG and non-UDG shapes seen in Figure 2.1 is no longer present.

- A morphological disparity exists between isolated UDGs' and non-UDGs' stellar distributions, with UDGs having notably larger b/a and smaller c/a axis ratios, both differing by ≈ 0.1 (see Figure 2.1). This more oblate-triaxial morphology is in agreement with Rong et al. [253] and Kado-Font et al. [254].
- Analysis of the isolated galaxies' morphological histories shows that UDGs are primarily the products of early mergers (see Figure 2.2). Further investigation shows that early mergers alone are not sufficient; high spins are also required (see Figure 2.3).
- Changing the criteria for being ultra-diffuse can result in largely different UDG populations, with the percentage of dwarfs that are identified as UDGs ranging from 19-65%, 33-70%, and 50-83% in the isolated, satellite, and cluster environments, respectively (see Table 2.2).
- A galaxy's status as a UDG is dependent on its orientation, and this dependence is strongest in the isolated environment (see Figures 2.5 & 2.6). Additionally, more restrictive definitions (like G0-F and R0) result in a stronger orientation dependence (see Figures 2.6 & 2.7). This orientation dependence also manifests when comparing the mass functions of all potential UDGs to those identified from a random orientation (see Figure 2.8).
- Although it is standard practice to identify UDGs from a face-on orientation, we find a significant number of galaxies that are identified as UDGs at some orientation, but do not meet the criteria when face-on. Depending on the

UDG definition, there are 48-138, 8-63, and 0-26 such galaxies in isolated, satellite, and cluster environments, respectively (see Table 2.3).

- Changing the definition of a UDG can change or obscure the underlying physics of the resultant UDG population. The unique formation mechanism of early, high-spin mergers in isolated UDGs under the restrictive definitions (like G0-F and R0) is not highlighted under the less restrictive RE definition, where the UDG and non-UDG populations are effectively homogenized (see Figures 2.1 & 2.10).

We have shown that the population of dwarfs that are considered UDGs, and whether that population exhibits a morphological distinction or formation channel from non-UDGs, is drastically dependent on choice of definition. With all of the outstanding questions around UDG formation, it is clear that different conclusions can be reached when identifying separate subsets of dwarfs as “ultra-diffuse”. In order for more advanced questions (like those of formation and evolution) to be answered cohesively, we must first come to a cohesive methodology for identifying UDGs. More restrictive definitions (like G0-F and R0) seem to identify a subset of isolated dwarf galaxies with unique shape histories, indicating a specific channel of formation through early, high-spin mergers, while less restrictive definitions identify such a large population of UDGs that the UDG and non-UDG populations are roughly identical. In short, it seems that whether UDGs are a true physical phenomenon or simply a product of definition depends on the definition itself.

Chapter 3

The Role of Mass and Environment on Satellite Distributions around Milky Way Analogs in the ROMULUS25 Simulation

Reproduced from Van Nest et al. 2023 [293] with permission from the AAS

We study satellite counts and quenched fractions for satellites of Milky Way analogs in ROMULUS25, a large-volume cosmological hydrodynamic simulation. Depending on the definition of a Milky Way analog, we have between 66 and 97 Milky Way analogs in ROMULUS25, a 25 Mpc per-side uniform volume simulation. We use these analogs to quantify the effect of environment and host properties on satellite populations. We find that the number of satellites hosted by a Milky Way analog increases predominantly with host stellar mass, while environment, as measured by the distance to a Milky Way-mass or larger halo, may have a notable impact in high isolation. Similarly, we find that the satellite quenched fraction for our analogs also increases with host stellar mass, and potentially in higher-density environments. These results are robust for analogs within 3 Mpc of another Milky Way-mass or larger halo, the environmental parameter space where the bulk of our sample resides. We place these results in the context of observations through comparisons to the Exploration of Local VolumE Satellites and Satellites Around Galactic Analogs surveys. Our results are robust to changes in Milky Way analog selection criteria, including those that mimic observations. Finally, as our samples naturally include Milky Way-Andromeda pairs, we examine quenched fractions in

pairs vs isolated systems. We find potential evidence, though not conclusive, that pairs, defined as being within 1 Mpc of another Milky Way-mass or larger halo, may have higher satellite quenched fractions.

3.1 Introduction

The satellites of the Milky Way and its neighbors in the Local Group, thanks to their proximity, have often served as our basis of understanding satellite and dwarf galaxy formation and evolution. In the past decades there has been an explosion in our understanding of satellites around our own Milky Way [294, 295, 296, 27] and Andromeda [297, 298, 299]. Further, in the age of ultra-faint galaxy detection, the low surface brightness end of the Milky Way’s satellite distribution continues to grow [300, 301, 296]. As we continue to discover fainter objects nearby, the question of the Milky Way’s uniqueness becomes an important one. Applying what we learn locally to the Universe at large would not be appropriate if the Local Group could be considered “atypical”.

To test for any potential discrepancy, surveys such as the “Satellites Around Galactic Analogs” (SAGA) [302, 303] and “Exploration of Local VolumE Satellites” (ELVES) [304, 305, 306, 307] study the satellite distributions of galaxies similar to our own, placing the Milky Way in a broader, cosmological context. The SAGA survey is an ongoing effort to compile spectroscopically complete satellite luminosity functions of 100 Milky Way analogs with distances between 20 and 40 Mpc, providing vastly improved statistics for the bright end of these satellite

distributions (down to $M_R=-12.3$). In complement to the SAGA survey’s probing of distant Milky Way-like systems, the ELVES survey seeks to fully map the satellite distributions of the hosts within the Local Volume fully (< 12 Mpc) down to $M_V=-9$.

Working in tandem, SAGA and ELVES will provide a better understanding of both what a “typical” Milky Way-like halo will look like and what influences an environment like the Local Volume can impart. The SAGA survey has found that the luminosity function of the Milky Way is consistent with their observations of other systems, but that the host-to-host scatter in the number of satellites is large [303]. SAGA also finds that the total number of satellites in a system correlates with the host’s K -band luminosity. Similar to SAGA, the ELVES survey finds that satellite abundance correlates with host mass and that the Milky Way is typical for its mass. However, Carlsten et al. [306] find that the observed luminosity functions of local hosts are typically “flatter” than predicted by the cosmological model; the stellar-to-halo mass relation tends to underpredict bright satellites and overpredict faint ones, a result found also by SAGA [302]. These results highlight the power of a larger sample of galaxies and their satellites to provide context for understanding satellite dwarf galaxies.

One of the most interesting discrepancies to be highlighted so far is that the quenched fraction of Local Group (Milky Way and Andromeda) satellites is not in agreement with SAGA’s results: the SAGA sample exhibits lower quenched fractions than those found in the Local Group. On the other hand, the ELVES survey finds higher quenched fractions amongst the Local Volume than in the

SAGA sample, though still not as high as the Local Group. Although Mao et al. [303] carefully attempt to quantify incompleteness in the SAGA survey, it remains an open question whether SAGA may be missing faint, red, or low surface brightness satellites which would be predominantly quenched [307, 308], or whether the Local Group is a true outlier in terms of quenched satellite fraction.

In general, various simulations of Milky Way-like galaxies tend to find good agreement in their resulting quenched satellite fractions, lying somewhere between the Local Group and Local Volume fractions [309, 310, 311, 312]. These simulations generally find that galaxies that infall into a host Milky Way with stellar masses above $M_* \sim 10^8 M_\odot$ are better able to retain their gas and continue star forming for extended periods. On the other hand, galaxies with stellar masses below $10^8 M_\odot$ instead tend to experience ram pressure stripping that strips gas and quenches their star formation (SF), and the quenching time scales can often be quite short (< 2 Gyr) [313, 314, 315, 309]. These results lead to high predicted quenched satellite fractions as luminosity decreases.

On the theoretical front, many analyses use zoom-in simulations of a handful of Milky Way analogs (e.g. Akins et al. [309] and Samuel et al. [312]), though Font et al. [308] use the ARTEMIS suite of 24 cosmological Milky Way-mass zooms to interpret the ELVES and SAGA results. Font et al. [308] find that applying a surface brightness limit to the ARTEMIS satellites can bring the quenched fractions and radial distributions into line with the SAGA results, suggesting that SAGA is missing faint surface brightness galaxies. Fainter surface brightnesses correlate with more quenching at a fixed luminosity in ARTEMIS, and thus bias the SAGA

results if true. On the other hand, Engler et al. [316] found that a surface brightness cut could not bring the TNG50 satellite quenched fractions fully into agreement with SAGA, though it did bring the simulation and observational results more into line. Engler et al. [316] were able to use TNG50, a 50 Mpc on-a-side uniform cosmological volume, to study a larger sample of Milky Way analogs and look for statistical trends. In this work, we use ROMULUS25, a 25 Mpc on-a-side uniform cosmological volume with comparable resolution to TNG50, to study similar trends. We particularly focus on the questions of how host mass and large-scale environment impact both satellite counts and quenched fractions for our simulated Milky Way analogs.

The paper is outlined as follows. We begin in Section 3.2 by describing the ROMULUS25 simulation. In Section 3.3 we outline our various methods for identifying Milky Way analogs, as well as their satellites. In Section 3.4 we present our primary results, focusing on the general size of the satellite populations and their quenched fractions. We then discuss and summarize our results in Sections 3.5 & 3.6, respectively.

3.2 Simulation

For this work, we use the ROMULUS25 simulation [113]. ROMULUS25 was run with CHANGA [112] which includes standard physics modules previously used in GASOLINE [255, 263, 317] such as a cosmic UV background [265] including self-shielding [266], SF, ‘blastwave’ supernova (SN) feedback [273], and low-

temperature metal cooling [272]. CHANGA implements an updated smoothed particle hydrodynamics (SPH) routine that uses a geometric mean density in the SPH force expression, allowing for the accurate simulation of shearing flows with Kelvin-Helmholtz instabilities [317]. Finally, a time-dependent artificial viscosity and an on-the-fly time-step adjustment [261] system allow for more realistic treatment of weak and strong shocks [317].

ROMULUS25 assumes a Λ cold dark matter (Λ CDM) model with cosmological parameter values following results from Planck [115] ($\Omega_0 = 0.3086$, $\Lambda = 0.6914$, $h = 0.6777$, and $\sigma_8 = 0.8288$). The simulation has a Plummer equivalent force softening of 250 pc (a spline softening of 350 pc is used, which converges to a Newtonian force at 700 pc). Unlike many similar cosmological runs, the dark matter particles were *oversampled* relative to gas particles, such that the simulation was run with initially 3.375 times more dark matter particles than gas. This increased dark matter resolution allows for the ability to track the dynamics of supermassive black holes within galaxies [260]. The result is a dark matter particle mass of $3.39 \times 10^5 M_\odot$ and gas particle mass of $2.12 \times 10^5 M_\odot$. These relatively low dark matter particle masses decrease numerical effects resulting from two-body relaxation and energy equipartition, which occur when particles have significantly different masses, both of which can affect the structure of simulated galaxies (e.g. Ludlow et al. [318]). ROMULUS25 has been shown to reproduce important galaxy and supermassive black hole scaling relations [113, 319, 320, 321].

3.2.1 SF and gas cooling

Gas cooling at low temperatures is regulated by metal abundance as in Guedes et al. [322], as well as SPHs hydrodynamics that include both thermal and metal diffusion as described in Shen et al. [262] and Governato et al. [164] (thermal and metal diffusion coefficients set to 0.3, see Tremmel et al. 2017 and 2019 [113, 114] for an in-depth discussion). SF and associated feedback from SNe are crucial processes that require subgrid models in cosmological simulations like ROMULUS25. Following Stinson et al. [273], SF is regulated with parameters that encode SF efficiency in dense gas, couple SN energy to the interstellar medium (ISM), and specify the physical conditions required for SF. These parameters were calibrated using several dozen zoom-in simulations of dwarf to Milky Way-mass galaxies [113] and are as follows.

1. The normalization of the SF efficiency, $c_{\text{SF}} = 0.15$, and formation timescale, $\Delta t = 10^6$ yr, are both used to calculate the probability p of creating a star particle from a gas particle that has a dynamical time t_{dyn}

$$p = \frac{m_{\text{gas}}}{m_{\text{star}}} (1 - e^{-c_{\text{SF}} \Delta t / t_{\text{dyn}}}). \quad (3.1)$$

2. The fraction of SN energy coupled to the ISM, $\epsilon_{\text{SN}} = 0.75$.
3. Minimum density, $n_{\star} = 0.2 \text{ cm}^{-3}$, and maximum temperature, $T_{\star} = 10^4 \text{ K}$, thresholds beyond which cold gas is allowed to form stars.

Star particles form with a mass of $6 \times 10^4 M_{\odot}$, or 30% the initial gas particle

mass. ROMULUS25 assumes a Kroupa initial mass function [274] with associated metal yields and SN rates. Feedback from SNe uses the ‘blastwave’ implementation [273], with thermal energy injection and a cooling shutoff period approximating the ‘blastwave’ phase of SN ejecta when cooling is inefficient.

3.2.2 Halo Identification

Amiga Halo Finder (AHF) [278] was applied to ROMULUS25 to identify dark matter halos, subhalos, and the baryonic content within. AHF uses a spherical top-hat collapse technique [279] to calculate each halo’s virial radius (R_{vir}) and mass (M_{vir}). Halos are considered resolved if their virial mass is at least $3 \times 10^9 M_{\odot}$ at $z = 0$. This corresponds to dark matter particle count of $\sim 10^4$, and a stellar mass of at least $10^7 M_{\odot}$ (star particle count of ~ 150). Following Munshi et al. [111], stellar masses were scaled by a factor of 0.5 as a photometric correction for a better comparison to values inferred from typical observational techniques, and all magnitudes use the Vega zero-point.

3.3 Analog and Satellite Identification

There is no concrete definition of what constitutes a Milky Way analog; observational surveys like SAGA and ELVES make sample cuts using K -band magnitudes as proxies for stellar mass, while simulations have access to more exact values for halo properties such as stellar mass and virial radius. In this work, we select samples of Milky Way analogs according to three different criteria sets in order to test if the selection criteria can influence the resultant satellite distribution. Our

samples are defined as follows.

- *A general M_{vir} restriction:* any halo where $10^{11.5} < M_{vir}/M_\odot < 10^{12.5}$.
- *A general M_* restriction:* any galaxy where $10^{10} < M_*/M_\odot < 10^{11}$. This corresponds to the host stellar mass range outlined in Section 2.1.2 of SAGA II [303]. A stellar mass of $10^{10} M_\odot$ also corresponds to the lower limit of the ELVES survey [307].
- *An $M_k + Environmental$ restriction:* any galaxy where $-24.6 < M_K < -23$. Additionally, no neighbor within 300 kpc can have $M_{K,\text{neighbor}} < M_{K,\text{MW}} - 1.6$. This corresponds to the K -band magnitude cut and environmental restrictions from SAGA II [303].

We also explore two different ways to identify a satellite galaxy. First, we consider galaxies within the host’s virial radius down to a stellar mass of $10^7 M_\odot$, the resolution limit for ROMULUS25. This corresponds to an magnitude limit of $M_R \approx -12.6$. We note that the magnitude limit for the SAGA survey is $M_R = -12.3$ (though they have four satellites below this limit; see SAGA [303]), so our samples do not probe the lowest-mass regions of the SAGA or ELVES sample spaces. In addition, we perform a selection where satellites are identified by being within 300 kpc of a Milky Way analog, rather than the analog’s virial radius, as a more direct comparison to the SAGA and ELVES surveys. We note, however, that these surveys use 2D projected distances while in this work we use true 3D distances. In the event that a satellite is hosted by multiple analogs, it is ascribed to the most massive host. Any satellites that fall into the criteria of a

Table 3.1: A Summary of Our Samples of Milky Way Analogs and Satellites

¹ Analog Criteria	² Analog Radius	³ N_{MW}	⁴ N_{Sats}	⁵ $\max(N_{Sat})$
M_{vir}		67	138	8
M_*	R_{vir}	97	210	13
$M_K + \text{Env.}$		77	148	13
M_{vir}		66	125	6
M_*	300 kpc	90	171	7
$M_K + \text{Env. (SAGA II)}$		77	137	6

Note. (1) The criteria for identifying Milky Way analogs; (2) the virial radius of the Milky Way analog for the purpose of identifying satellites; (3) the total number of Milky Way analogs; (4) the total number of satellites with $M_* > 10^7 M_\odot$; and (5) the largest number of satellites hosted by a single Milky Way analog. Milky Way analogs are not included in the satellite distribution. As a final step, any analogs that host a “satellite” more massive than themselves are removed from consideration. This cut is partially responsible for the slight variation in the number of Milky Way analogs under the same criteria when switching between the R_{vir} and 300 kpc satellite identifications. Our sample of Milky Way analogs and satellites are summarized for each criteria set in Table 3.1.

Figure 3.1 shows the three Milky Way analog samples that we focus on in this work: M_{vir} and M_* with R_{vir} and M_K with 300 kpc. While the samples largely overlap, we find that none of them are simple subsets of the others. As they approach the boundaries of the selection cuts, the samples diverge from one

another. For example, the stellar mass sample probes virial masses below the virial mass cut, and vice versa. This is the result of natural scatter within the stellar-halo mass relation, which was shown in Tremmel et al. [113] to match observations [87, 323]. Within the overlapping regions of the criteria, there are galaxies considered Milky Way analogs in some samples but not others. This occurs as a result of the environmental criteria in the SAGA sample, which could remove analogs that are still within the K -band magnitude limits.

In Figure 3.2, we compare the normalized distributions of hosts and satellites from our largest sample, M_* with simulated R_{vir} (in order to encapsulate the full magnitude range of our samples), to data from SAGA II and ELVES [303, 307]. We note that the ELVES satellites are weighted according to their likelihood estimates (P_{sat} in Table 9 of [307]), so each satellite adds its likelihood as a count rather than 1. In panel (a), we see that our hosts' span in K -magnitude space matches well with the ELVES sample, while the SAGA II sample (by definition) resides in $-24.6 < M_K < -23$. The peaks of the host distributions are in good agreement as well, though we note our peak is at a slightly dimmer magnitude than the observational data. In panel (b), we see that our satellite distribution is in very good agreement with the SAGA II data, though we have an interesting lack of satellites at $M_K \approx -17$. The ELVES data probe much dimmer satellites (due to the difference in observational limits), but when only considering satellites brighter than $M_K = -12$, the ELVES sample is still more concentrated at low-mass satellites when compared to SAGA II and ROMULUS25. This is consistent with ELVES finding steeper luminosity functions (fewer high-mass satellites and

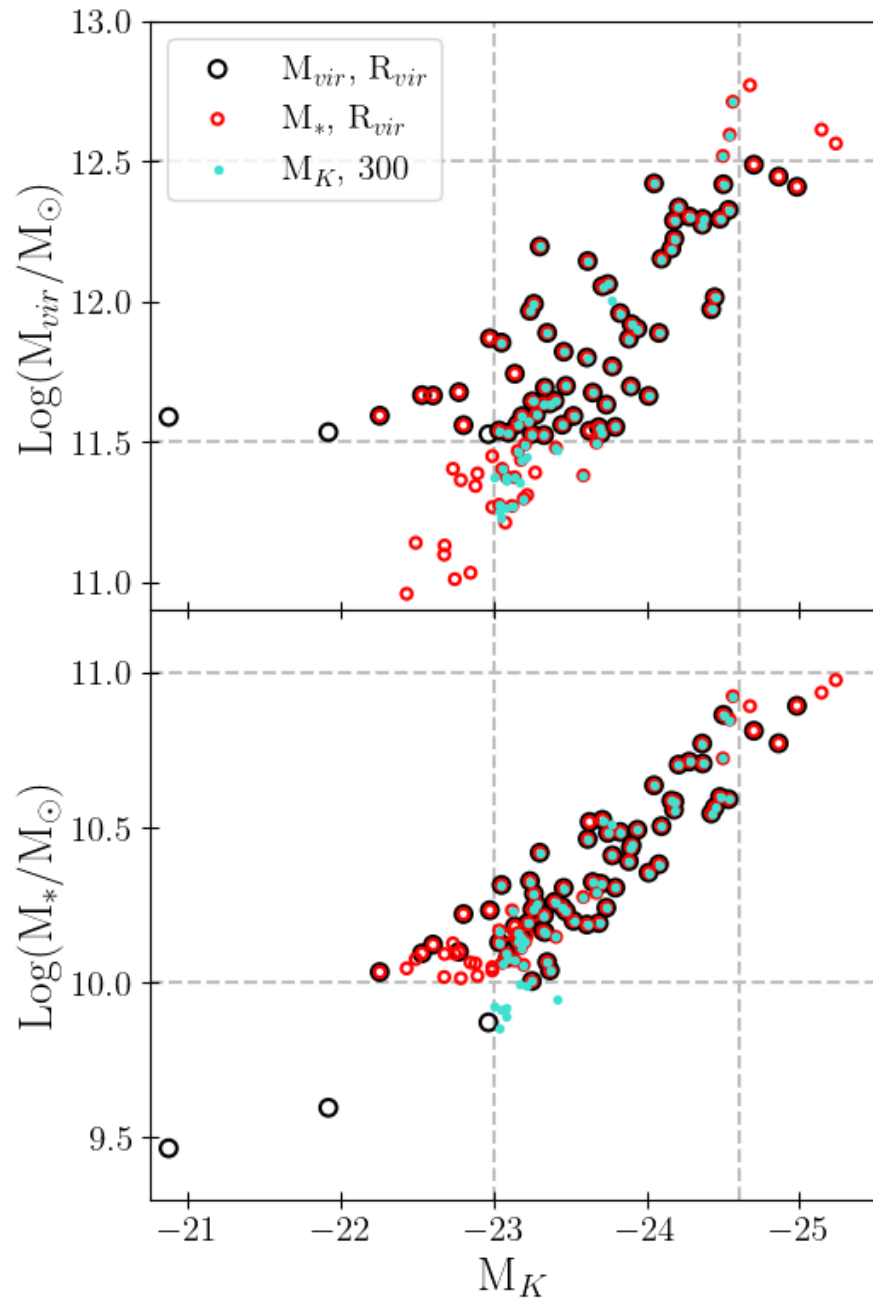


Figure 3.1: Virial and stellar masses plotted against K -band magnitudes for three of our Milky Way analog samples. The dotted lines denote the mass and magnitude cuts used in our samples. The samples diverge at the different boundaries, and even within the boundaries there are analogs that exist in some definitions but not others.

more low-mass ones) in their sample when compared to SAGA, and might also contribute to the different quenched fractions found by the two surveys (see Section 3.4.2 for discussion).

3.4 Results

Figure 3.3 shows the V -band satellite luminosity function for our sample of Milky Way analogs alongside data from the Milky Way and several Milky Way-like systems. The outer gray region outlines the space occupied by our M_* within R_{vir} sample, while the black line and inner dark gray region indicate the mean and standard deviation. The Milky Way and M31 data are taken from SAGA [302]. The NGC 4258 and NGC 4631 data were taken from Carlsten et al. [306], the M94 data from Smercina et al. [324], and the M101 data from Bennet et al. [325]. We find that our sample of Milky Way analogs is in good agreement with these observations. We note that the space occupied by our sample remains largely unaffected when changing the Milky Way analog criteria.

3.4.1 Host Effects on Satellite Accumulation

In order to study how the physical properties of our Milky Way analogs affect their satellite populations, we separated our sample according to their mass and environment. Figure 3.4 shows the average number of satellites hosted by the Milky Way analogs where the analogs are binned according to their stellar mass and minimum distance to a Milky Way-sized or larger halo, hereafter D_{MW+} . In calculating D_{MW+} , we consider the closest galaxy outside the system of the

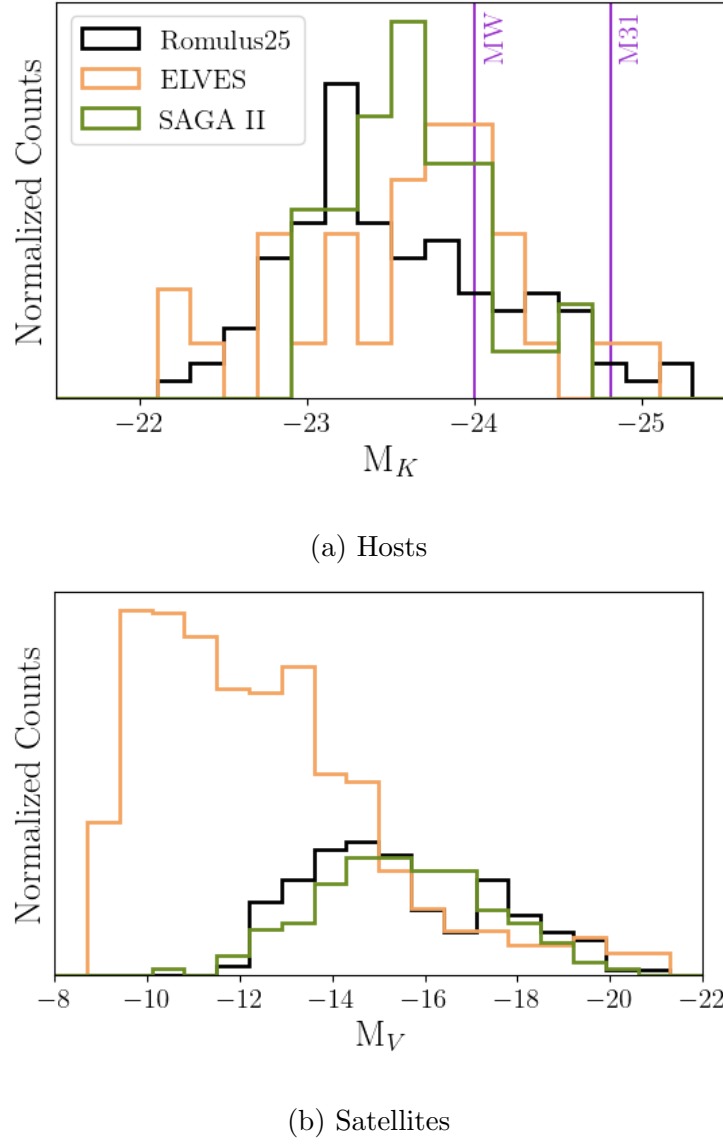


Figure 3.2: Normalized histograms of (a) hosts in K -band magnitude and (b) satellites in V -band magnitude for our M_* with simulated R_{vir} sample. We make direct comparisons to SAGA II [303] and ELVES [307] data, with the Milky Way and M31 values taken from the latter. The ELVES satellites are weighted according to their likelihood measurements. For a fair comparison, the satellite distributions in (b) are all normalized to the samples' number of satellites brighter than $M_V = -14$, the approximate completeness limit for ROMULUS25.

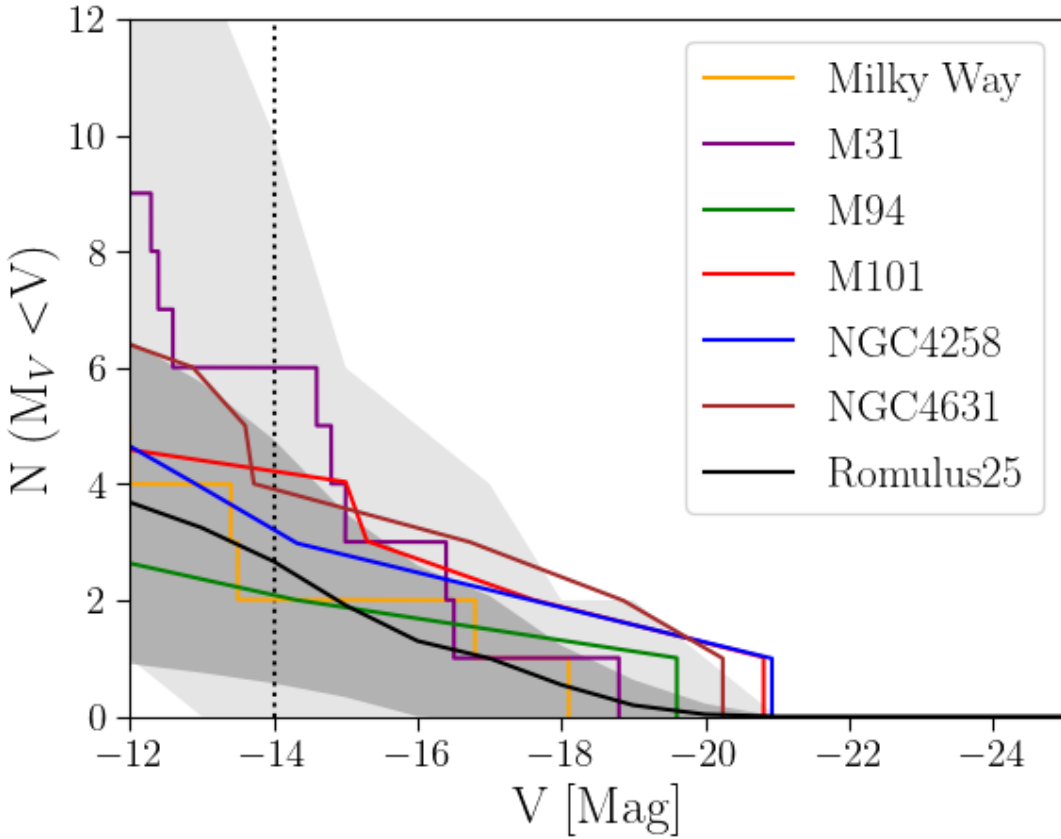


Figure 3.3: The V -band satellite luminosity function for our Milky Way analog sample under the M_* with simulated R_{vir} criteria. The black line and dark gray region represent the mean and single standard deviation of our sample, respectively, while the outer light gray region encompasses our entire sample. We compare to the Milky Way and M31 [302], M94 [324], M101 [325], and NGC 4258 and NGC 4631 [306]. The dotted vertical line marks the approximate completeness limit for ROMULUS25. Our sample is in good agreement with these observations.

analog (i.e., not a satellite) that exceeds the minimum criteria of Milky Way analog under the given criteria. The text in each bin details N (the number of analogs in that bin) and σ (the standard deviation of the number of satellites hosted by analogs in that bin). A plot is shown for both our M_{vir} with simulated R_{vir} (left) and SAGA II comparison (right) samples. In all of our samples, the number of hosted satellites appears to increase with host mass, and potentially with decreasing D_{MW+} . However, this latter trend cannot be verified by eye as the box size of ROMULUS25 yields a lack of data in the upper regions of this plot (i.e., highly isolated hosts), so the apparent trend is not statistically significant.

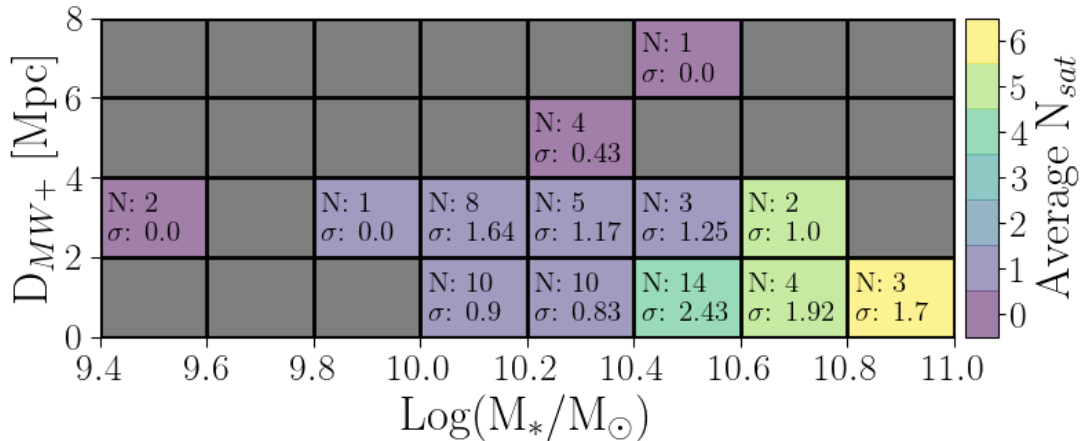
While these macroscopic trends are present across all of our simulated samples, there are some notable differences in the distributions. We see that while the M_{vir} definition includes analogs at a lower stellar mass, the number of analogs below $M_* = 10^{10} M_\odot$ is much larger in the SAGA II sample. Additionally, in the higher-mass bins there is fluctuation in both the number of analogs and hosted satellites due to the changing of the satellite selection radius from R_{vir} to 300 kpc.

In an effort to quantify the “by-eye” trends seen in Figure 3.4, we looked at the specific frequency of the number of satellites hosted by our Milky Way analogs, S_N , normalized to their mass and environment. We use the following specific frequency equations adapted from Harris et al. [326]:

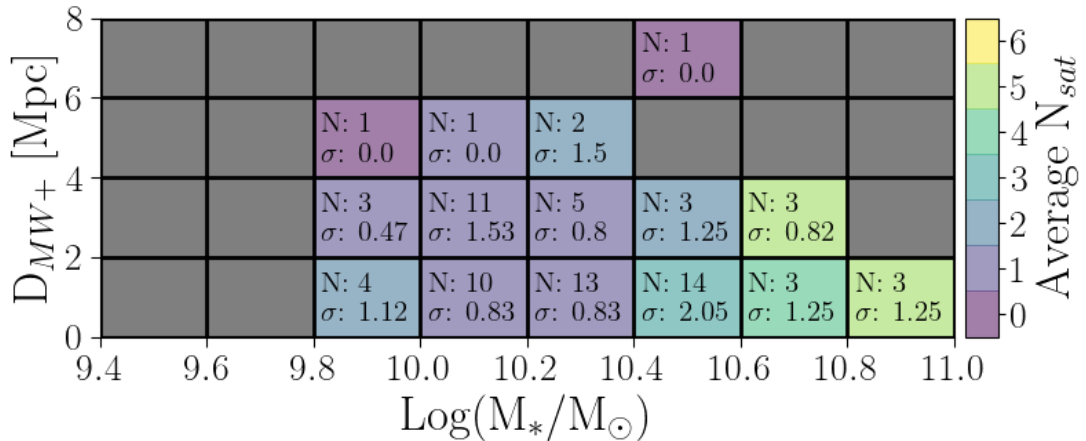
$$S_{N,\text{env}} = N_{\text{sat}} \times 10^{0.4(D-1.5)} \quad (3.2)$$

$$S_{N,\text{mass}} = N_{\text{sat}} \times 10^{0.4(M-10.3)} \quad (3.3)$$

Here, N_{sat} is the number of satellites hosted by the Milky Way analog, D is D_{MW+}



(a) M_{vir} with simulated R_{vir}



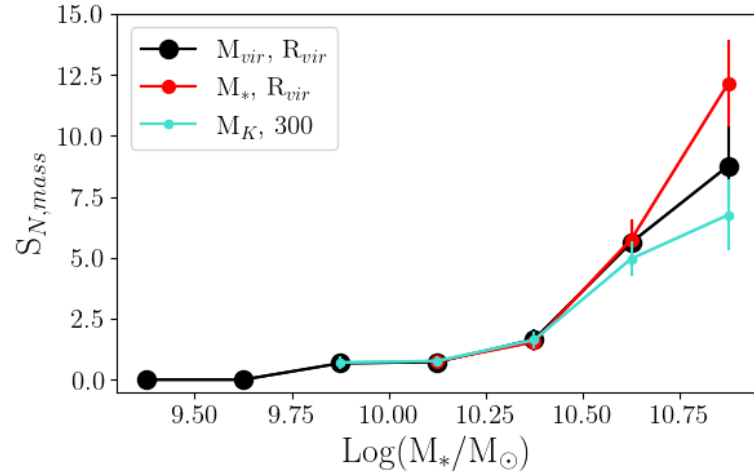
(b) SAGA II Comparison Sample

Figure 3.4: The average number of satellites hosted by Milky Way analogs as a function of stellar mass and environment (distance to a Milky Way-sized or larger halo). The text in each box indicates the number of Milky Way analogs in that parameter space, as well as the standard deviation amongst the number of satellites. The left plot shows the M_{vir} with simulated R_{vir} sample, while the right plot shows the sample most analogous to the SAGA Survey. In both cases, the number of satellites appears to increase as stellar mass increases.

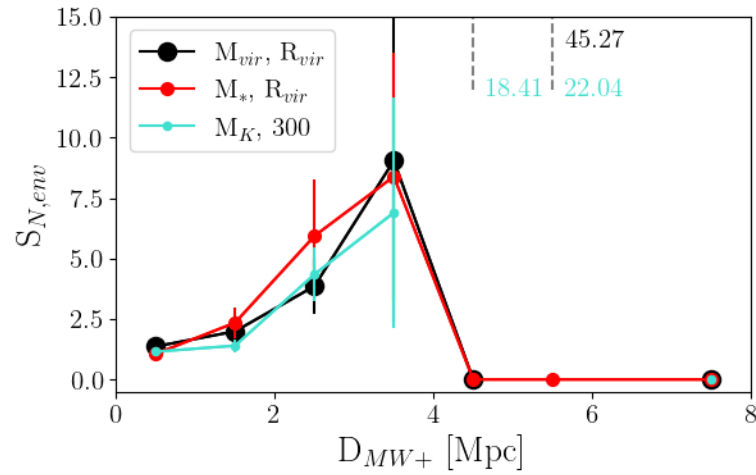
in units of Mpc, and M is $\log(M_*/M_\odot)$. The normalization values of 1.5 Mpc and 10.3 were chosen to be roughly the averages of the M_* with simulated R_{vir} sample.

Figure 3.5 shows the specific frequencies normalized to mass and environment for our M_{vir} and M_* with simulated R_{vir} sample, as well as our SAGA II comparison sample. In looking at the trend with mass, the S_N values consistently increase with the stellar masses of the Milky Way analogs. These results, which are present in all of our Milky Way analog samples, indicate that stellar mass exerts a large influence on satellite accumulation. The SAGA and ELVES surveys both observe this trend of satellite abundance increasing with host mass, though the trends they find are slightly weaker than ours (see Section 3.5.1 for discussion). Further, a study of seven nearby Milky Way-like systems with the Hyper Suprime-Cam on the Subaru telescope observes this trend as well [327]. The trend of satellite abundance with host mass was also found by Font et al. [328] using the ARTEMIS suite of zoom-in simulations [329], and by Engler et al. [310] using the TNG50 simulation.

In looking at the trend with environment, Figure 3.5(b), we see some interesting behavior. The S_N values increase somewhat linearly until $D_{MW+} \approx 3.5$ Mpc, where future points go either to zero or extreme outliers. This would suggest that N_{sat} increases as hosts become more isolated, but we note that a majority of our hosts (\sim 60%-70%) have $D_{MW+} < 2$ Mpc, so beyond this distance our samples get increasingly small, resulting in the large error bars and stochasticity of the higher- D_{MW+} points. Thus, we see no definitive trend of satellite accumulation with environment, though one might become present with a larger sample of



(a) Specific Frequency of N_{sat} normalized to mass



(b) Specific Frequency of N_{sat} normalized to environment

Figure 3.5: The specific frequencies of the number of satellites hosted by Milky Way analogs normalized to their (a) stellar mass and (b) distance to a Milky Way-sized or larger halo, D_{MW+} . The plots show the results for the M_{vir} (black) and M_* (red) with simulated R_{vir} and SAGA II (blue) samples. Error bars represent the standard error within each bin (σ/\sqrt{N}). With the exception of some large outliers, the $S_{N,\text{env}}$ values do not show statistically significant trends. However, the $S_{N,\text{mass}}$ values show a clear positive trend.

more isolated hosts. However, we do not believe that we can fully rule out an environmental impact on satellite accumulation through a measurement of specific frequency. Figure 3.6 shows the average number of satellites hosted by our analogs when binned by their D_{MW+} measurement. We see that if we split our analogs into subsamples of ‘pairs’ and ‘isolated’ based on having $D_{MW+} < 1$ Mpc or > 1 Mpc, the average numbers of hosted satellites, plotted as red diamonds, are notably different between the subsamples. This difference, which is present in all of our samples except $M_K + \text{Env.}$ with simulated R_{vir} , is driven primarily by the low number of satellites hosted by analogs in the $\sim 3 - 5$ Mpc bin. Although this is where our sample tapers off in D_{MW+} space, we can see that the number of analogs in this bin is certainly nonnegligible, and may be hinting at a strong environmental impact on satellite accumulation in more extreme isolation. The stochasticity of our trends in Figure 3.5(b) compared to the more direct information from Figure 3.6 leads us to believe that normalizing specific frequency to such an extremely variable parameter (in this case, large-scale environment) does not yield a reliable measurement.

3.4.2 Host Effects on Satellite Quenching

In addition to studying the number of satellites hosted by our analogs, we also analyzed the quenched fraction of the satellites. When studying the quenched fraction (f_q), we only consider satellites with a stellar mass of at least $10^8 M_\odot$, as ROMULUS25 may be subject to numerical overquenching below this mass [249]. A galaxy is considered quenched if its instantaneous specific star formation rate

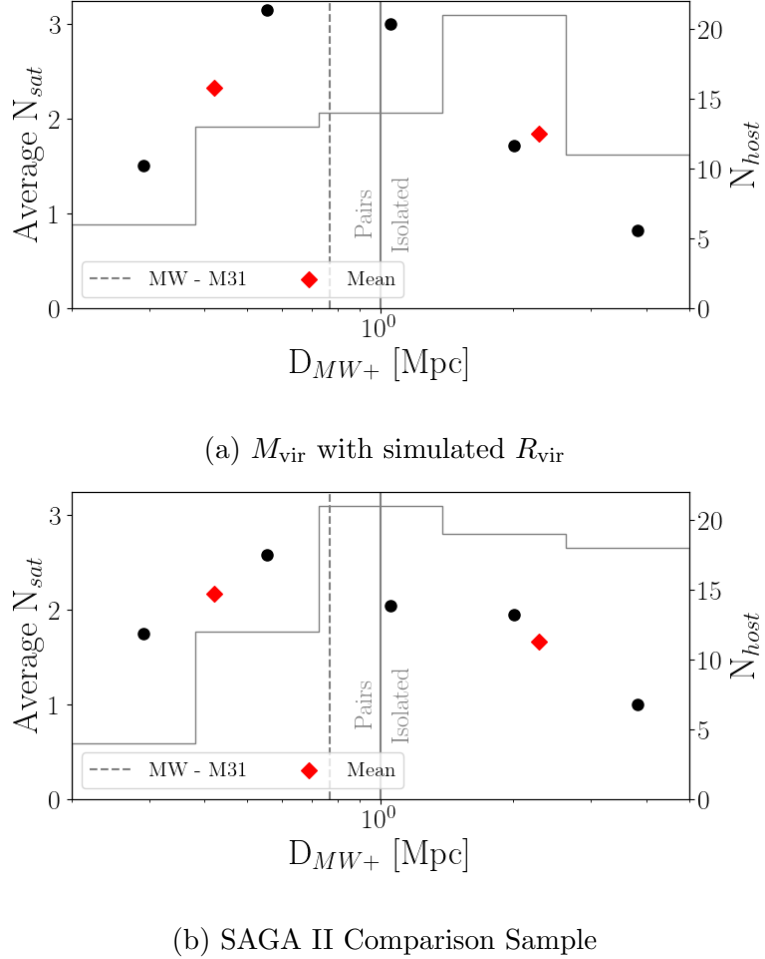
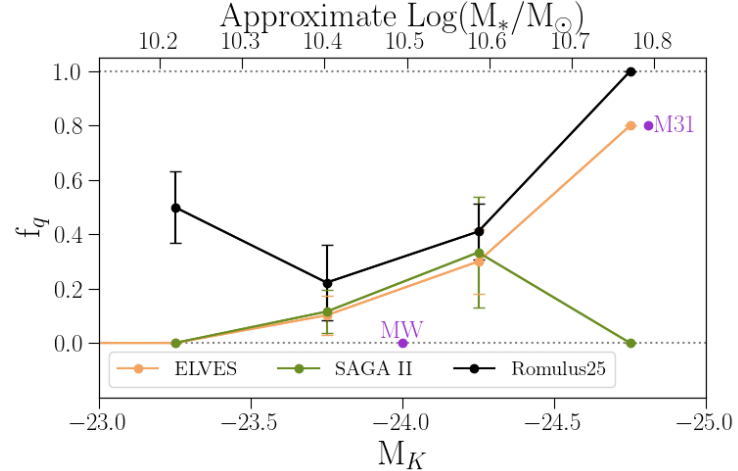


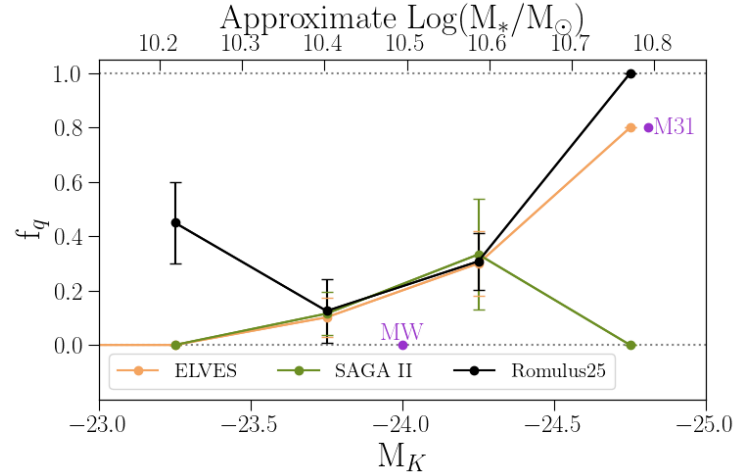
Figure 3.6: Points show the average number of satellites hosted by Milky Way analogs binned by D_{MW+} for our (a) M_{vir} with simulated R_{vir} and (b) SAGA II comparison sample. Hosts whose D_{MW+} measurements are within 1 Mpc are considered to be in “pairs”, while the rest are considered “isolated”, and the means of these two subsamples are plotted as red diamonds. The histogram data shows the number of hosts in each bin, and the Milky Way-M31 distance is plotted as a dashed vertical line for reference. In both samples the isolated subset hosts fewer average satellites than the pairs, and this is driven predominantly by the most isolated bin.

(sSFR) is below 10^{-11} yr $^{-1}$. The instantaneous sSFR is calculated using the expected SFR from gas particles meeting the temperature and density thresholds for SF given in Section 3.2.1. In Figure 3.7, we show our quenched fractions as a function of host K -band magnitude for the $M_K + \text{Env.}$ with 300 kpc satellite selection (our SAGA II comparison sample), and compare our results to data from the SAGA and ELVES surveys [303, 307]. For a direct comparison, we only consider SAGA and ELVES satellites with stellar masses above $10^8 M_\odot$. We note, however, that the SAGA and ELVES surveys' methods of determining quenching are different than ours: SAGA considers a satellite quenched if it lacks strong H α emission (equivalent width (EW) of H α < 2Å) and ELVES considers a satellite quenched if it exhibits an early-type morphology, i.e., not exhibiting clear star-forming structures such as blue clumps or dust lanes (this correlates with color as well; see Carlsten et al. [305] for an in-depth discussion). Our sSFR quenched definition was shown (see Sharma et al. [321]) to yield a good match to galaxies identified observationally as quenched using EW[H α]< 2Å and $D_{\text{n}}4000 > 0.6 + 0.1 \log_{10} M_*$ (as in Geha et al. [330]).

While all three samples show the quenched fractions increasing with host brightness, our simulated sample exhibits slightly larger quenched fractions than the observational surveys, with the exception of the lowest-mass bin where the difference becomes significant (see Section 3.5.2 for discussion). The SAGA and ELVES data are in very good agreement up to the brightest magnitude bin, where the sample sizes are only one host for ELVES (M31) and two hosts for SAGA (NGC 5792 and NGC 7541). This agreement within the high-mass satellite subset



(a) SAGA II Comparison Sample



(b) SAGA II Comparison Sample with Surface Brightness Cut

Figure 3.7: (a) Quenched fraction plotted against K -band magnitude for the $M_K + \text{Env.}$ sample from ROMULUS25 compared to SAGA II [303] and ELVES [307] data. (b) The same sample from ROMULUS25 with addition criteria of requiring satellites to have $\mu_{\text{eff},r} < 25 \text{ mag arcsecond}^{-2}$. As a direct comparison, the SAGA and ELVES data plotted here only contain satellites with stellar masses above $10^8 M_\odot$, and the Milky Way and M31 values are taken from ELVES. Error bars represent the standard error within each bin.

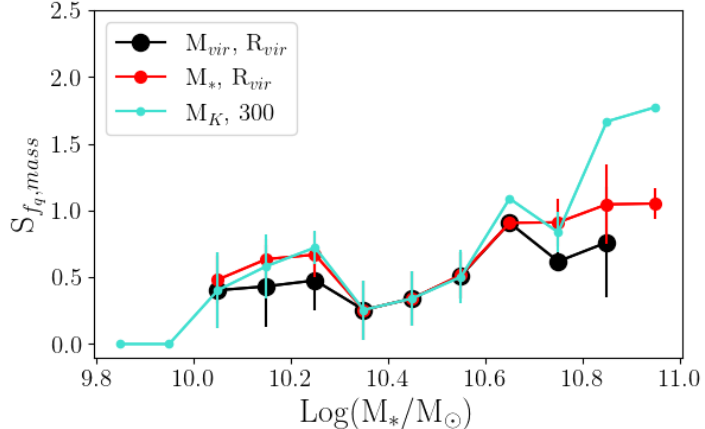
is interesting, as the SAGA and ELVES quenched fractions are quite different when considering their full samples. Carlsten et al. [307] find that the quenched fractions of the Local Volume are significantly higher than the SAGA sample (their figures 11 & 12), particularly in the low-mass satellite regime. In Figure 3.2(a), we see that the ELVES survey contains a much larger number of faint satellites when compared to SAGA, but also that ELVES hosts (along with those of ROMULUS25) probe fainter magnitudes.

In studying the ARTEMIS simulations, Font et al. [308] found that the SAGA detection methods may be preferentially selecting star forming or recently quenched satellites near their completeness limit, missing a notable population of quenched dwarfs. This detection bias could explain the difference between SAGA and ELVES low-mass satellites, both the abundances and quenched fractions. Following Font et al. [308], in Figure 3.2(b) we apply an additional cut to our SAGA II comparison sample by requiring satellites to have $\mu_{\text{eff},r} < 25 \text{ mag arcsecond}^{-2}$. As in the ARTEMIS simulations, we find that this cut lowers the resultant quenched fractions, and brings our results (particularly the middle bins) into excellent agreement with SAGA and ELVES.

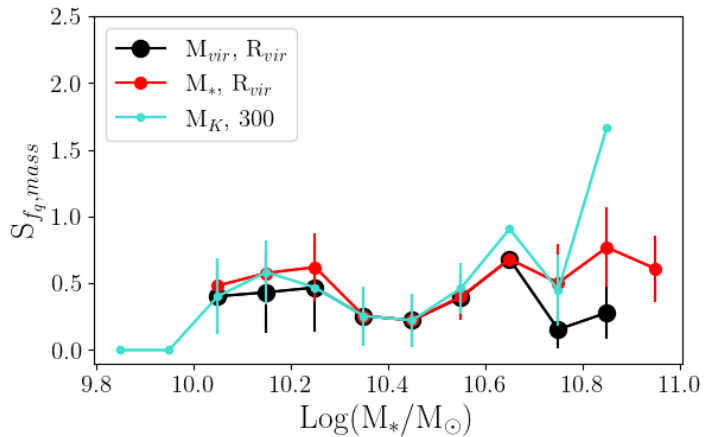
To quantify the trend of quenched fraction with mass seen in Figure 3.7, and to search for a trend with environment, we again used the specific frequency in Equation (2) with N_{sat} replaced by f_q . Figure 3.8(a) shows our quenched fraction specific frequencies for the M_{vir} and M_* with simulated R_{vir} samples, as well as our SAGA II comparison sample. We find that, as with the number of hosted satellites, we see a trend of S_N with host mass, indicating that larger hosts are

expected to yield higher quenched fractions. However, we note that this trend is not as strong as the one seen in Figure 3.5(a). Interestingly, when applying the satellite surface brightness criteria in Figure 3.8(b), we see that our trend of quenched fraction with host mass is effectively erased. As the high-mass end of Figure 3.8(b) is strongly affected by this surface brightness cut, it seems that the preferentially quenched satellites below this threshold are more common in higher-mass hosts, which is consistent with Figure 3.8(a) implying a larger number of quenched galaxies in this regime. Our results agree with Engler et al. [316] who, using the TNG50 run from the IllustrisTNG simulations, found that massive hosts exhibit systematically larger satellite quenched fractions. Further, Engler et al. [316] found no difference in quenching between isolated and paired analogs when considering satellites within 300 kpc of their host (see Section 3.5.3 for discussion).

To look for a trend with environment, we examined the quenched fractions of our systems plotted against D_{MW+} . Figure 3.9 bins our analogs in D_{MW+} space, and shows the quenched fraction of all satellites hosted by analogs in each bin. Again, pairs are identified as having $D_{MW+} < 1$ Mpc. The figure shows data for our M_* and $M_K + \text{Env.}$ samples (both R_{vir} and 300 kpc), where the color of each point represents the number of satellites in each bin. We find that the average quenched fraction is higher among pairs than isolated analogs, though the magnitude of this difference is not ubiquitous across our samples (see Section 3.5.3 for discussion). In fact, while not shown in the plot, the M_{vir} criteria exhibit no notable difference in the average quenched fractions of paired and isolated



(a) Specific Frequency of f_q normalized to mass



(b) Specific Frequency of f_q normalized to mass with Surface Brightness Cut

Figure 3.8: The specific frequencies of the quenched fraction of satellites hosted by Milky Way analogs normalized to their stellar mass. The plots show the results for the M_{vir} (black) and M_* (red) with simulated R_{vir} and SAGA II (blue) samples. Subplot (b) applies the surface brightness cut to satellites ($\mu_{\text{eff},r} < 25$ mag arcsecond $^{-2}$). Error bars represent the standard error within each bin. As with N_{sat} , there is a notable positive trend with Milky Way analog mass. However, applying the surface brightness cut to our satellites effectively removes the trend with mass.

analogs. We also find that in the switch from 300 kpc to R_{vir} when identifying satellites, hosts typically have either the same or lower quenched fractions and a higher satellite count. This indicates that restricting satellites to within 300 kpc for this host range is more likely to exclude satellites, and that the satellites beyond 300 kpc are predominantly star forming; though this is still only when considering satellites with $M_* > 10^8 M_\odot$.

Similar to Figure 3.6, this difference between our ‘pairs’ and ‘isolated’ subsamples is largely driven by the most isolated bin, where the quenched fractions are extremely low. This, again, could be alluding to a strong environmental effect on satellite quenching in the highly isolated regime that we do not quite capture in ROMULUS25. This result is at odds with the aforementioned study of TNG50 by Engler et al. [316], as well as the study of FIRE-2 by Samuel et al. [312], both of whom find no difference in quenching between isolated and paired analogs. However, the simulations studied in Samuel et al. [312] are zoom-in simulations, and thus would not capture the large-scale isolation in which we begin to see differences between paired and isolated hosts.

While this work does not consider signs of conformity within satellites, we did perform some cursory analysis on how the quenched fractions and number of hosted satellites relate to the instantaneous SFRs of our analogs. We find that the quenched fractions exhibit no notable trend with host SFR. In looking at the average number of hosted satellites, though, we do see a correlation of more populated systems having a higher host SFR. However, we believe this is just a reflection of the number satellites increasing with host mass, as scaling to sSFR

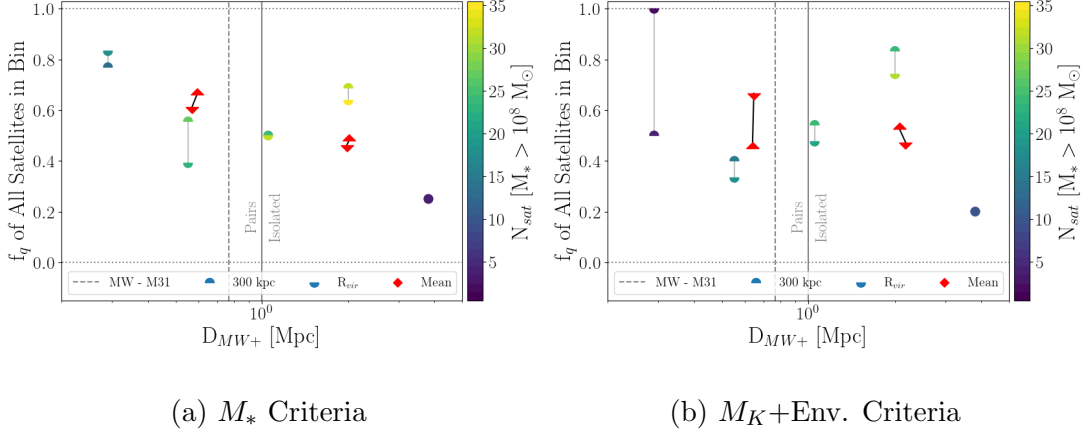


Figure 3.9: Quenched fraction plotted against the distance to the closest Milky Way halo or larger for the (a) M_* and (b) $M_K + \text{Env.}$ criteria. Analogs are binned by D_{MW+} and quenched fractions are taken from an aggregate of all satellites in each bin. The upper-hemisphere points represent analogs from the sample with a Milky Way radius of 300 kpc, while lower-hemisphere points represent the sample using the simulated virial radius with vertical lines bridging the two. The colors of each point represent the number of hosted satellites with stellar mass greater than $10^8 M_\odot$. The samples are separated into “Pairs” and “Isolated” by whether the closest Milky Way or larger halo is within 1 Mpc, and the means of each sample are denoted by the red diamonds. For reference, the Milky Way-M31 distance is plotted with a vertical dashed line.

largely removes this correlation.

3.5 Discussion

In Section 3.3, we discussed the various methods by which we identified Milky Way analogs and satellites. While shifting between these definitions has no effect on our conclusions, there are subtle impacts worth noting.

3.5.1 Satellites within R_{vir} versus 300 kpc

In Figures 3.4 & 3.5 we showed host stellar mass to be a driving factor in satellite accumulation, but this trend is less prominent when using our SAGA II comparison sample. This appears to be the result of using 300 kpc to identify satellites, not the selection on K -band magnitude, as our $M_K + \text{Env.}$ with R_{vir} sample actually exhibits the strongest trend. In fact, identifying satellites via a 300 kpc selection rather than R_{vir} reduces the strength of the mass trend in all criteria (though the trend is still prominent). The weakening of the trends is the result of analogs in the high-mass regime (where the trends manifest), which have virial radii larger than 300 kpc and exclude satellites in this shift to 300 kpc. This shift is in agreement with the ARTEMIS simulations [328], in which satellite abundance trends strongly with host mass, but the trend is weakened when SAGA observation selection criteria are applied ($M_{r,\text{sat}} < -12$, $\mu_{\text{eff},r} < 25 \text{ mag arcsecond}^{-2}$, and within 300 kpc of the host).

When considering quenched fractions, our choice of satellite selection radius also seems to have a noticeable effect on our $M_K + \text{Env.}$ sample. In Figure

3.9(b), the switch from R_{vir} to 300 kpc typically raises the quenched fraction while lowering the number of satellites (with the notable exception of the least isolated bin). Thus, within the context of satellites with $M_* > 10^8 M_\odot$, it seems applying a satellite cut of 300 kpc to the K -band magnitude analog selection primarily removes star-forming satellites from massive hosts, and biasing the global quenched fraction high.

Since the 300 kpc selection results in a more centrally located satellite population, it is likely that these satellites had an earlier infall time and underwent more ram pressure stripping when compared to satellites near or beyond 300 kpc from the host. This effect is present in Figure 3.8 as well, wherein the SAGA II comparison sample exhibits the strongest trend of quenched fraction with host mass. These results are consistent with those from the TNG50 simulation [316], another large-volume, uniform-resolution simulation with comparable resolution to ROMULUS25.

3.5.2 Quenched Fraction Discrepancy

The shift from R_{vir} to 300 kpc, however, does not explain why our quenched fractions are higher than those of SAGA and ELVES (Figure 3.7). Our SAGA II comparison sample uses 300 kpc as a selection radius, and our results indicate that if SAGA and ELVES had access to the virial radii of their hosts, their quenched fractions would be lower. Donnari et al. [331] find that the adopted definition of quenching and using 2D projected distances can both affect the resultant quenched fractions. Notably, the quenched fractions of ROMULUS25 are

in better agreement with the observations when satellites with $\mu_{\text{eff},r} < 25$ mag arcsecond $^{-2}$ are removed, in agreement with Font et al. [308]. The exception is the faintest bin, where a key factor may be the resolution of ROMULUS25. The lower resolution of the volume is unable to resolve a multiphase ISM, i.e., there is no extremely dense gas [114, 248]. Thus, all of the gas is “puffy” and overly susceptible to ram pressure stripping and quenching.

Dickey et al. [332] found that large-scale cosmological simulations overquench isolated galaxies below $M_* = 10^9 M_\odot$ when compared to Sloan Digital Sky Survey. The authors attribute this to overefficient feedback, which is typically tuned to recreate quenched fractions found in the Local Volume. In looking at ROMULUS25, Sharma et al. [321] also found that isolated dwarfs exhibit a higher quiescent fraction when compared to observations, but that this can be entirely attributed to the presence of massive black holes and their feedback. Although we are not studying isolated dwarfs in this work, it is still likely that these feedback properties are influencing our results. We note, however, that there are only six satellites in our SAGA II comparison sample with black holes and $M_* > 10^8 M_\odot$ so this does not notably affect our results.

3.5.3 Isolated vs. Paired Hosts

Figure 3.9 suggests that pairs exhibit higher quenched fractions than more isolated analogs, but there are some caveats preventing us from making a more robust statement about the environment’s effect on the quenched fraction. First, we are only considering satellites with $M_* > 10^8 M_\odot$. Within our SAGA II sample,

this is only \sim 56% of our total satellite population and they are hosted by \sim 72% of our Milky Way analogs with a nonzero satellite count (or \sim 49% of all Milky Way analogs), so a large section of our population is being removed. Secondly, our simulation box size prevents us from having a large sample of highly isolated analogs; only \sim 14% of our SAGA II sample analogs have $D_{MW} > 3$ Mpc. Finally, by ignoring low-mass satellites, we are looking at the quenched fractions of several systems with few satellites (only one or two satellites). Around 43% of the high-mass satellite-hosting analogs in our SAGA II sample contain only one satellite above our resolution limit, so their quenched fractions can only occupy the extremes of 0 and 1, and in Figures 3.8 & 3.9 these systems are being considered equally alongside systems with as many as eight high-mass satellites (though the binning in Figure 3.9 should alleviate this issue). These combined effects yield a sample that is lacking low-mass satellites (and thus the analogs' full satellite distributions) as well as highly isolated hosts, making it difficult for us to extrapolate our results to the Universe at large.

Recently, Engler et al. ([316]; TNG50) and Samuel et al. ([312]; FIRE-2) found no difference in the satellite quenched fractions of paired and isolated hosts in their simulations. Further, Garrison-Kimmel et al. ([333]; FIRE-2) found that the satellites of isolated Milky Way-mass galaxies have nearly identical SF histories to satellites of Milky Way analogs in Local Group-like pairs. However, these results were only considering satellites within 300 kpc of the host. In looking further out to 300-1000 kpc, Engler et al. [316] find that paired, Local Group-like hosts exhibit significantly larger quenched fractions than their isolated counterparts.

3.6 Conclusions

Using the ROMULUS25 simulation, we have created various samples of Milky Way analogs along with their satellite distributions. We explored the role of host mass and environment on satellite numbers and quenched fractions. Our results can be summarized as follows.

- When testing various criteria for defining a Milky Way analog, from more theoretically motivated (M_{vir}) to more observationally motivated (M_* and SAGA-like), we find that the resultant samples do not fully overlap. Within the overlapping regions, galaxies may also be defined as analogs in one sample but not in another due to environmental criteria (see Table 3.1 and Figure 3.1).
- The number of satellites hosted by a Milky Way analog increases predominantly with host stellar mass, while environment may have a significant impact in high isolation ($D_{MW+} > 3 \text{ Mpc}$; see Figures 3.4-3.6).
- The quenched fraction (for satellites with $M_* > 10^8 M_\odot$) of our analogs increases with host mass (see Figures 3.7(a) & 3.8(b)), but applying a surface brightness cut to satellites can erase this trend (see Figure 3.8(d)).
- Being in a pair may yield higher satellite quenched fractions, but it is hard to draw statistically robust results given the small volume of ROMULUS25 and the fact that we can only study satellites down to $M_* = 10^8 M_\odot$ to avoid numerical overquenching. (see Figure 3.9).

We find that the distributions of both the Milky Way and M31 are well explained by our sample, with M31 being at the highly populated edge of our sample space. This is in agreement with the SAGA and ELVES surveys, where ELVES found the Local Volume to be slightly more populated and exhibiting a steeper luminosity function when compared to the full SAGA sample. Additionally, we are in agreement with ELVES in finding that the stellar mass of a Milky Way analog seems to be the dominant factor in both the number of hosted satellites and the number of quenched satellites. Interestingly, in our study of quenching, we find that the SAGA and ELVES results are in good agreement for satellites with $M_* > 10^8 M_\odot$, suggesting that their discrepancy in quenched fraction comes from lower-mass satellites, which we are unable to probe here due to numerical effects that artificially quench simulated galaxies. However, our results support the notion put forward in Font et al. [308] that SAGA is missing a large population of low surface brightness satellites near its detection limit that are preferentially quenched.

Chapter 4

A Study of Stellar Shapes in the Marvel-ous Dwarfs and DC Justice League Simulations

We present a study of various 2D and 3D morphological measurements of dwarf galaxies in the “Marvel-ous Dwarfs” and “DC Justice League” N-body+SPH cosmological zoom-in simulations. We find that measurements of ellipticity based on measuring 2D isophotes typically return more elongated shapes compared to projections of the 3D shape tensor, and that this discrepancy grows stronger with inclination angle. Using the shape tensor, we calculate the Triaxiality parameter for both the stellar and dark matter components of our halos, and find the components are generally in good agreement. We recreate the deprojection method introduced in Kado-Fong et al. [334], and find that, while there is decent scatter on a halo-to-halo basis, it reasonably recovers the qualitative morphologies of our galaxies. We also calculate the ellipticity-central surface brightness correlation put forward by Xu et al. [335], and find that it also well recovers the qualitative morphology of our individual galaxies. All methods of 3D morphology measurement suggest that the simulations host a population of oblate, high mass dwarf satellite galaxies.

4.1 Introduction

Dwarf galaxies, being the most numerous and dark matter-dominated systems in the universe, have been a fertile testing ground for the Cold Dark Matter (CDM) paradigm. While the CDM framework has been largely successful in explaining

the observed universe (see [118]), several issues arose when observations and simulations began thoroughly exploring the small-scale regime. Contentions such as the “missing satellites” problem [125, 59, 58], the “too big too fail” problem [132, 336], and the “cusp-core” problem [145, 146, 140] all called into question the fidelity of both cosmological simulations and the CDM framework itself.

While these issues were primarily alleviated in a CDM paradigm through improved baryonic physics (with a focus on feedback mechanisms) in cosmological simulations [6, 187, 75, 97, 189, 193, 195], alternate dark matter models, such as self-interacting dark matter (SIDM), remain valid possibilities [165, 168, 169, 170]. Thus, the in-depth study of dwarf galaxies remains a promising avenue for constraining dark matter models.

Past studies of dwarf galaxies have largely focused on stellar populations, kinematics, and mass profiles in an effort to understand the underlying dark matter halos [337, 338, 339, 340, 341], and while focus on dwarf morphology is growing [342, 343, 344, 335, 334], a lot of work is left to be done, thanks to the technical challenges of obtaining clean morphological data for these faint objects and the difficulty in inferring the underlying 3D structure.

Dwarf morphology, however, can also be an insightful tool for probing dark matter halos and testing dark matter models. To date, CDM simulations have predominantly produced halos that are prolate [345, 346]. On the other hand, simulations of SIDM have shown that halos’ inner regions are notable more spherical than their CDM counterparts [169]. Since dwarf galaxies are so dominated by dark matter, we would expect this morphological difference in dark matter

to follow through into the stellar morphology. Dwarf spheroidals, as they have been shown to be relatively isotropic in velocity dispersion and not rotationally supported [294, 347, 348, 349, 335], would be particularly good test subjects. To do this however, we require reliable and accurate methods of quantifying dwarf galaxy morphology.

In this work, we compare various methods, both direct and indirect, of quantifying the 2D and 3D morphologies of dwarf galaxies in CDM simulations. We begin in Section 4.2 by outlining the Marvel and DCJL simulations and our sample of galaxies. In Section 4.3, we perform direct methods of shape measurement, including isophote fitting and shape tensor calculations. In Section 4.4, we perform indirect methods of inferring 3D morphology. Namely, we recreate the method of MCMC deprojection introduced in Kado-Fong et al. [334] (Section 4.4.1) and calculate the ellipticity-central surface brightness correlation put forward by Xu et al. [335] (Section 4.4.2). In Section 4.5, we discuss preliminary results of dark matter halo shape measurements in SIDM. Finally, we summarize our conclusions in Section 4.6.

4.2 Simulations

This work utilizes the “Marvel-ous Dwarfs” and “DC Justice League” simulation suites (hereafter “Marvel” and “DCJL”, respectively) [116]. Each suite consists of four cosmological zoom-in simulations, which, rather than simulating individual galaxies, simulate small volumes of multiple galaxies at high resolution. Marvel

and DCJL were both run with the Nbody+SPH code CHANGA [112] which utilizes the hydrodynamic modules from GASOLINE2 [255, 317].

The Marvel suite (CptMarvel, Elektra, Storm, and Rogue) simulates populations of dwarfs within an environment comparable to the Local Volume using a WMAP3 cosmology [117]. These simulations implement gas, initial star, and dark matter particle masses of $1410 M_{\odot}$, $420 M_{\odot}$, and $6650 M_{\odot}$, respectively, and have a force resolution of 60 pc. This high resolution allows galaxies in the range of $M_* \approx 3 \times 10^3 M_{\odot}$ to $10^{11} M_{\odot}$ to be considered resolved.

The DCJL suite (Sandra, Ruth, Sonia, and Elena) simulates ~ 1 Mpc regions centered on Milky Way-mass galaxies using a Planck cosmology [118]. These slightly lower, “Near Mint” resolution simulations implement initial gas, initial star, and dark matter particle masses of $2.7 \times 10^4 M_{\odot}$, $8 \times 10^3 M_{\odot}$, and $4.2 \times 10^4 M_{\odot}$, respectively, and have a force resolution of 170 pc. These combined suites yield resolved dwarf galaxies down to ultra-faint dwarf masses in field, satellite, and backsplash environments.

4.2.1 Star Formation and Gas Cooling

Marvel and DCJL utilize the star formation scheme and gas cooling from Christensen et al. [350], the metal line cooling and metal diffusion from Shen et al. [262], and the nonequilibrium formation and destruction of molecular hydrogen is followed. A spatially uniform, time-dependent cosmological UV field background was adopted following Haardt et al. [265] in order to model photoionization and heating.

Star formation occurs stochastically in the presence of molecular hydrogen, H_2 , when the gas is sufficiently cold ($T < 1000K$) and dense ($n > 100m_H \text{ cm}^{-3}$).

The probability of a star particle forming within a time Δt is given by:

$$p = \frac{m_{\text{gas}}}{m_{\text{star}}} (1 - e^{-c_0^* X_{H_2} \Delta t / t_{\text{form}}}) \quad (4.1)$$

where m_{gas} is the mass of the gas particle, m_{star} is the initial mass of the forming star particle, and t_{form} is the local dynamical time. The star formation efficiency parameter, c_0^* , is set to 0.1 so that, when multiplied by the fraction of nonionized hydrogen in H_2 (X_{H_2}), the normalization of the Kennicutt-Schmidth relation is followed [271].

Supernova feedback is governed by a “blastwave” model [273], wherein thermal energy, mass, and metals are deposited into neighboring gas following a supernova. The energy coupled to the gas per supernova is 1.5×10^{51} ergs. Following a supernova, gas cooling is shut off for a period of time equal to the momentum-conserving “snowplow phase” [351]. The combined processes emulate the energy deposited within the interstellar medium by all process related to young stars, including UV radiation (see [352, 353]).

4.2.2 Halo Identification and Sample

The Amiga Halo Finder (AHF) [278] was applied to Marvel and DCJL to identify dark matter halos, subhalos, and the baryonic content within. AHF utilizes a spherical top-hat collapse technique [279] to calculate each halo’s virial radius and mass. These simulations identify the virial radius as the radius at which the

halo density is 200 times the critical density of the universe at a given redshift.

The full Marvel+DCJL sample introduced in Munshi et al. [116] includes over 200 resolved dwarf galaxies, around 90 of which are satellites. However, in this work we are limited by our galaxies needing to be large enough for the various methods of morphological measurements to be reliable. The main limiting method here is the measurement of the shape tensor in Section 4.3.2. Our final selection contains 51 galaxies: 33 from Marvel and 18 from DCJL. Further, 13 of these galaxies are satellites, which we denote separately throughout this work.

4.3 Direct Measurements of Morphology

4.3.1 Isophote Fitting

For each galaxy, a V -band luminosity density image is generated across all unique viewing orientations. This process of changing orientations is described in detail with a visual example in Section 4.3, paragraph 2 of Van Nest et al. [210] and is summarized here. Each galaxy is oriented to a face-on position before being rotated by angles θ and ϕ around two perpendicular axes in the plane of projection. This process is done for θ and ϕ values ranging from $[0^\circ, 180^\circ)$ and $[0^\circ, 360^\circ)$ respectively, in increments of 30° . At each orientation, a radially averaged surface brightness profile is generated and fit with a Sérsic profile in order to determine the surface brightness at the effective radius. The isophote of the effective surface brightness is then plotted on the V -band image and fit with an ellipse to determine the projected b/a axis ratio of the galaxy (hereafter denoted as q). While this work is

only considering V -band luminosities, testing in other bands shows no noticeable difference in the general shapes or radial locations of the isophotes. The top row of Figure 4.1 shows an example of this process for three different orientations of a galaxy from the CptMarvel simulation.

Ellipses are fit automatically to isophotes using the `skimage.measure.EllipseModel` python package, and any fits with RMS values above a select threshold are flagged for manual masking. RMS is defined by

$$\text{RMS} = \sqrt{\frac{\sum_{i=0}^{i=n} r_i^2}{n}} \quad (4.2)$$

where n is the number of image pixels in the isophote and r_i is the residual of the i^{th} pixel. High RMS values can originate from noisy isophote data or extended structures such as spiral arms or isolated star forming regions. These features are masked out in order isolate the isophote of the main, central structure of the galaxy. The bottom row of Figure 4.1 shows an example of this masking for a galaxy from the Storm simulation.

4.3.2 The Shape Tensor

For each galaxy, a 3D morphology is calculated through its shape tensor [354], defined by

$$\mathcal{S}_{i,j} = \frac{1}{M} \sum_k m_k (\mathbf{r}_k)_i (\mathbf{r}_k)_j \quad (4.3)$$

where m_k is the mass of the k^{th} particle, $(\mathbf{r}_k)_i$ is the distance from the k^{th} particle to the center along axis i , and M is the total mass in the considered volume. Following the iterative algorithm outlined in Tomassetti et al. [355], we calculate

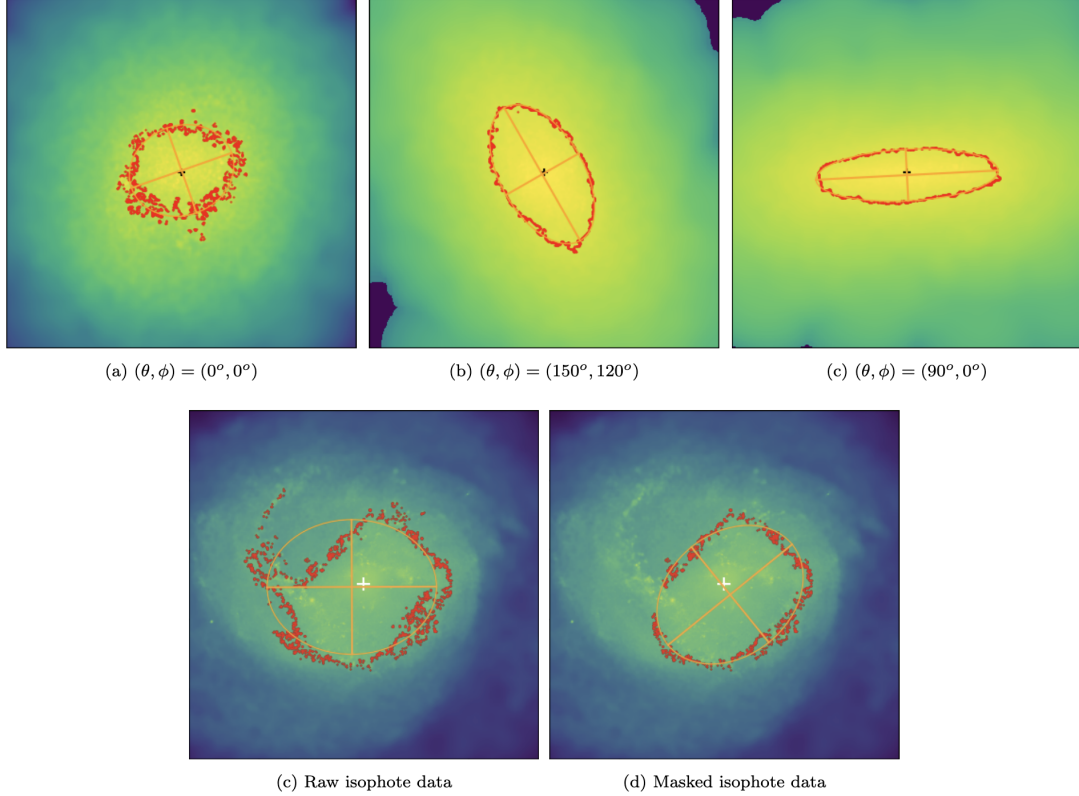


Figure 4.1: **(top)** V -band luminosity density images at three orientations for a sample galaxy from CptMarvel. The isophotes of effective surface brightness are shown in red, while the associated ellipse fits with semi-major and -minor axes are shown in orange. **(bottom)** An example galaxy from Storm showing extended structure in the isophote being masked out.

\mathcal{S} in radial shells where its eigenvalues (λ_i) yield the principle axes of the shell:

$$i = \sqrt{3 * \lambda_i} \text{ for } i = A, B, C \text{ and } \lambda_A \geq \lambda_B \geq \lambda_C \quad (4.4)$$

This process yields the intrinsic 3D axis ratios $Q = B/A$ and $S = C/A$ for each galaxy as a function of radius. We emphasize here that in this work, upper case letters are used for intrinsic, 3D morphologies while lower case letters are used for projected, 2D morphologies.

From here, we are able to project the 3D ellipsoids derived from the shape tensors into the 2D plane at the various orientations considered in Section 4.3.1. This allows us to directly compare shape tensor morphologies to those measured through isophote fits. The shape tensor is calculated at the radial bin matching the effective radius derived from the galaxy's Sérsic profile at the given orientation, and the resulting ellipsoid is then rotated to the matching position before being projected. In Figure 4.2, we compare these projected shape tensor values, q_{proj} , to the isophote values, q_{iso} , at two example orientations: a face-on position of $(\theta, \phi) = (0^\circ, 0^\circ)$ and an edge-on position of $(90^\circ, 0^\circ)$. We see that, for a vast majority of galaxies, the q_{iso} values are lower than their q_{proj} counterparts, often to a significant degree. This indicates that the isophotes are typically more elongated than their associated shape tensor projections. An example of this can be seen at the top of Figure 4.2 where we show the red isophotes from Figure 4.1(a,c) but with the projected shape tensor ellipse plotted in orange rather than the isophote fit. In looking at the satellite galaxies (plotted with triangles), we see that environment doesn't have any notable impact on this difference..

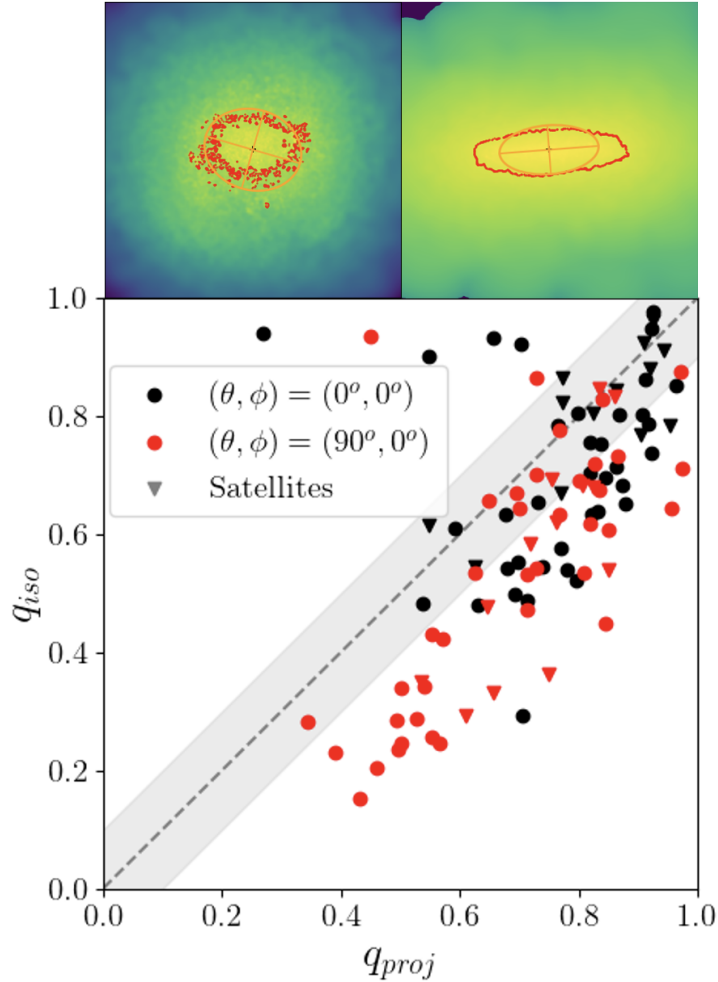
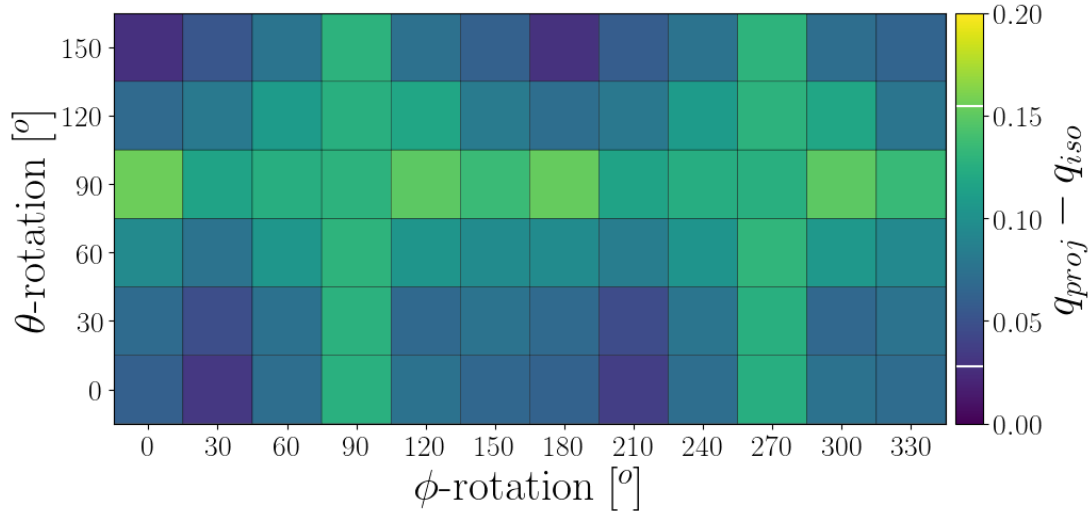
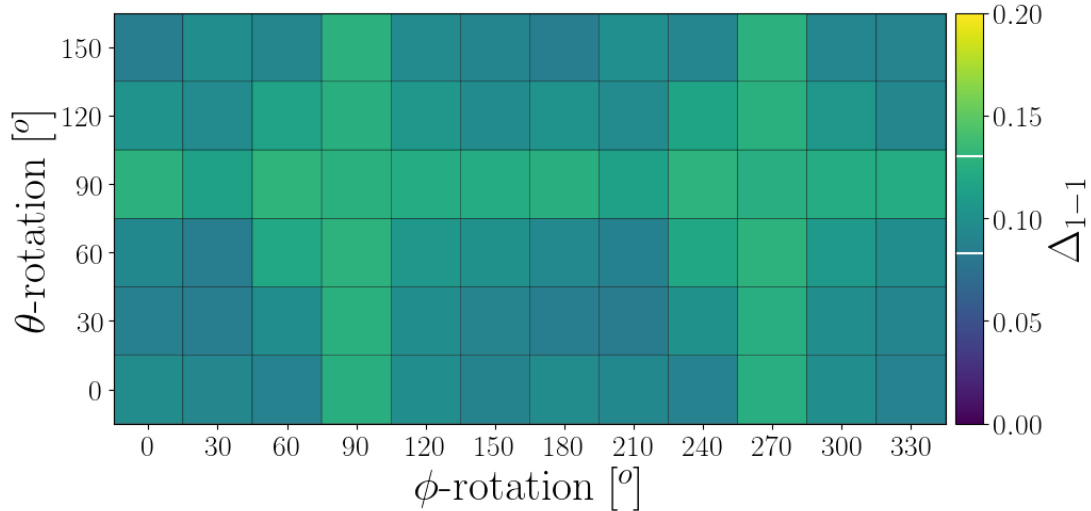


Figure 4.2: Comparisons between the q -axis ratio measured by isophote fitting and by projecting the 3D ellipsoid generated by the shape tensor. Points are shown for both a face-on orientation of $(\theta, \phi) = (0^\circ, 0^\circ)$ and an edge-on orientation of $(90^\circ, 0^\circ)$, along with a one-to-one line and gray region showing when the values are within 0.1 of each other. The top images show the example galaxy from Figure 4.1(a,c), only with the orange ellipse showing the projected shape tensor data rather than a fit to the red isophote. The isophote fits tend to return lower, more elongated (lower) q values compared to the shape tensor projections, and this effect is stronger at edge-on orientations.



(a)



(b)

Figure 4.3: **(a)** Average $q_{\text{proj}}-q_{\text{iso}}$ and **(b)** average distance of the values from the one-to-one line for our galaxies as a function of orientation. White lines on the color bar indicate the minimum and maximum values within the plot. We find that more edge-on orientations (angles around $\theta = 90^\circ$ and/or $\phi = 90^\circ, 270^\circ$) yield a higher discrepancy between q_{proj} and q_{iso} , with the isophotes being more elongated than the shape tensor projections.

Figure 4.2 also shows that this discrepancy between q_{iso} and q_{proj} is more extreme in the edge-on orientation compared to the face-on. To further illustrate this, Figure 4.3 shows the average $q_{\text{proj}} - q_{\text{iso}}$ values for each galaxy, as well as their distance from the one-to-one line ($\Delta_{1-1} = |q_{\text{proj}} - q_{\text{iso}}|/\sqrt{2}$), for every considered orientation. We see that orientations that are more edge-on (angles around $\theta = 90^\circ$ and/or $\phi = 90^\circ, 270^\circ$) are brighter in color, indicating a larger average discrepancy between q_{iso} and q_{proj} . This suggests that there is a systematic disagreement between these two methods of morphological measurement. Axis ratios measured via isophotes seem to be notably more elongated than those calculated with the shape tensor, and this discrepancy typically strengthens at higher inclinations.

4.3.3 Triaxiality

It is common for 3D morphologies to be quantified through their *triaxiality* parameter, T , as defined in Franx et al. [356]:

$$T = \frac{1 - Q^2}{1 - S^2} \quad (4.5)$$

where T values in $(0, \frac{1}{3}) / (\frac{1}{3}, \frac{2}{3}) / (\frac{2}{3}, 1)$ indicate a(n) oblate/triaxial/prolate morphology. By applying the shape tensor calculations from Section 4.3.2 to dark matter particles as well, we can obtain the axis ratios and triaxiality parameters of the dark matter halos in addition to the galaxies themselves.

Figure 4.4 shows the triaxiality parameters for both the stellar and dark matter content of our galaxies as a function of stellar mass. The T_* and T_{DM} values for individual galaxies are linked with vertical gray lines, and satellite galaxies are

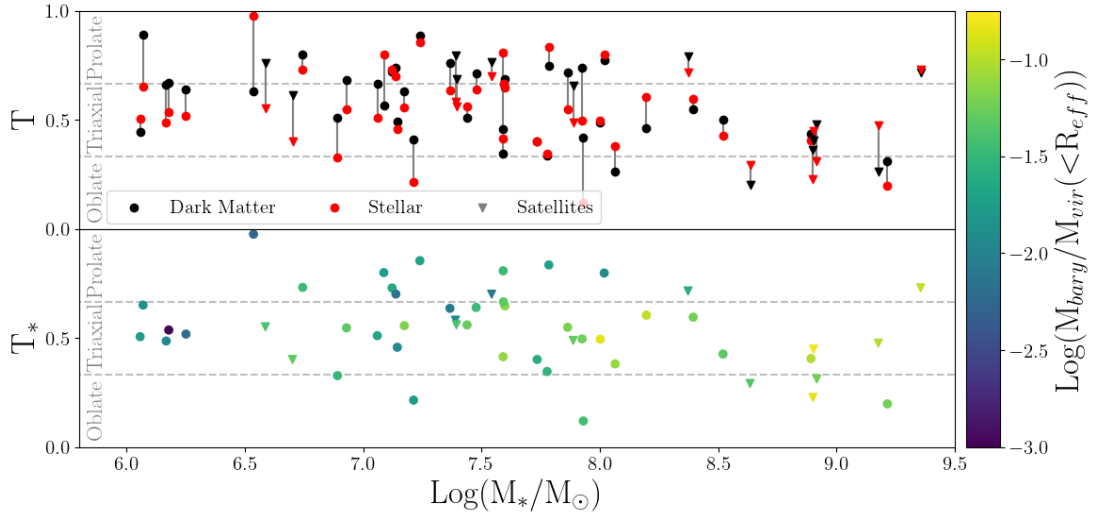


Figure 4.4: Triaxiality parameters for our galaxies as a function of stellar mass.

For each galaxy, a vertical line links the T -values for the dark matter particles and star particles. Satellite galaxies are denoted with triangles. T_* and T_{DM} are generally good agreement, with a few notable exceptions.

denoted with triangles. We see that the general morphologies of the galaxies follow that of the underlying dark matter halo, though with a fair bit of scatter. In looking at the satellite population, there doesn't seem to be any difference in how well stars trace DM when compared to their central counter parts, however, the higher-mass, more oblate galaxies seem to be predominantly satellites. In looking at stellar mass, we see that the more prolate morphologies, as well as the galaxies with large stellar-DM discrepancies, tend to have stellar masses below $\sim 10^8 M_\odot$. Interestingly, we have a notable population of galaxies in the more oblate region of the space ($T < 0.5$) that also have oblate DM halos, which we discuss further in Section 4.4.2.

4.4 Indirect Measurements of Morphology

4.4.1 Deprojection

Deprojecting 2D morphologies (such as observed isophotes) into 3D intrinsic morphologies is a non-trivial task. In the absence of additional data (such as kinematic information), it is an unconstrained problem to deproject a given 2D ellipse into a single 3D ellipsoid. However, Kado-Fong et al. [334] found that they were able to successfully infer the Q - and S -distributions of a large sample of dwarf galaxies by comparing the observed distribution of axis ratios, q , to the theoretical distribution produced by a sample of known 3D ellipsoids. Their methodology is summarized below.

The projected q of a 3D ellipsoid is dependent only on its principle axis ratios, (Q, S) , and the viewing angle, (θ, ϕ) :

$$f^2 = (S \sin\theta \cos\phi)^2 + (QS \sin\theta \sin\phi)^2 + (Q \cos\theta)^2 \quad (4.6)$$

$$\begin{aligned} g &= \cos^2\phi + \cos^2\theta \sin^2\phi \\ &+ Q^2(\sin^2\phi + \cos^2\theta \cos^2\phi) + (S \sin\theta)^2 \end{aligned} \quad (4.7)$$

$$h \equiv \sqrt{\frac{g - 2f}{g + 2f}} \quad (4.8)$$

$$q = \frac{1 - h}{1 + h} \quad (4.9)$$

Using this methodology, Kado-Fong et al. [334] were able to construct a distribution of “observed” q ’s for a sample of mock 3D ellipsoids with known Q and S axis ratios. From there, they construct a Poisson likelihood function of how likely

these known ellipsoids are to produce the q -distribution seen in the observational data:

$$\ln p(q|\mu_Q, \mu_S, \sigma_Q, \sigma_S) = \sum_i n_i \ln(m_i) - m_i - \ln(n_i!) \quad (4.10)$$

where n_i is the number of q from the observed distribution where $0.04i \leq q \leq 0.04(i+1)$, m_i is the number of q from the mock distribution in the same range, and μ, σ define the normal distributions over Q and S within the mock sample. Assuming flat priors over 0 to 1 for $\mu_{Q,S}$ (while enforcing $Q \geq S$) and 0 to 0.5 for $\sigma_{Q,S}$, the posterior probability distribution can be written as:

$$p(\alpha|q_{\text{obs}}) \propto p(q_{\text{obs}}|\alpha)p(\mu_Q)p(\mu_S)p(\sigma_Q)p(\sigma_S) \quad (4.11)$$

where $\alpha = \{\mu_Q, \mu_S, \sigma_Q, \sigma_S\}$. The posterior distribution is then sampled using the Markov Chain Monte Carlo (MCMC) ensemble sampler from the **emcee** python package [357] in order to find the maximally likely Q - and S - distribution that yields the observed q -distribution.

While the methodology put forward in Kado-Fong et al. [334] is built to deproject an ensemble of galaxies, we utilize it in this work to analyze a single galaxy by treating the various isophotes from different viewing orientations as an ensemble of q observations. The result of this analysis, rather than a normal distribution of Q and S values, would ideally give the singular Q and S values for the given galaxy (i.e. a normal distribution over the true value with a standard deviation of 0). However, we believe that the limit of our angular resolution in viewing orientations (in this case: 30° along both θ and ϕ) means that our space is too discrete to sample in this manor. To address this, we have implemented

`scipy.interpolate.RegularGridInterpolator` (RGI) to interpolate q values in between our imaged isophotes. In testing the RGI by imaging a sample galaxy with 10^o resolution we found it to be sufficiently accurate, with the difference between interpolated and hand measured q 's being predominantly within ± 0.05 . Thus, we are able to build our “observed q -distribution” (n from Eq. 4.11) by continuously sampling our image space 1000 times. We then run the MCMC sampler with 32 walkers for 3000 steps to obtain the deprojected axis ratios for each galaxy.

Figure 4.5 shows how the MCMC deprojected axis ratios (top) and triaxiality parameters (bottom) compare to those calculated from the shape tensor of the simulation particles. We see that, on the whole, the MCMC deprojections well recover the parameter space occupied by the shape tensor data. However, in looking at the shape tensor and deprojection measurements for individual galaxies (linked by gray lines), we see a lot of scatter. Further, the shape tensor data is more clustered in the spherical space (high Q and S) while the MCMC data has more points in the prolate region (low Q and S , high T) that is unoccupied by the shape tensor data. This discrepancy is not surprising, however, as the deprojections are inferred from isophote fits which were shown in Section 4.3.2 to be more elongated than the shape tensor projections. Thus, while this deprojection method can successfully return reasonable intrinsic 3D morphologies from 2D isophote data, it is still beholden to the discrepancy between isophote data and particle data (shape tensor projections).

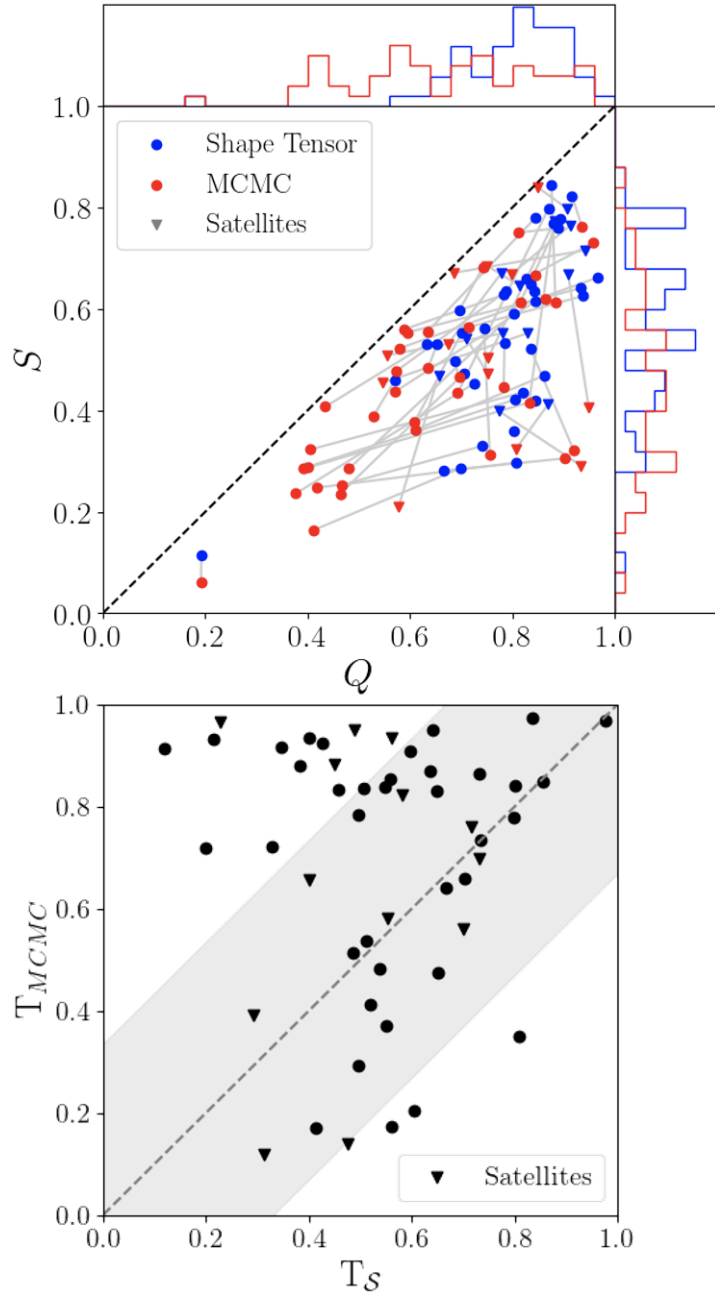


Figure 4.5: **(top)** A comparison of galaxies' B/A (Q) and C/A (S) axis ratios calculated from the shape tensor and MCMC deprojection. Gray lines connect the measurements for individual galaxies. **(bottom)** A comparison of galaxies' triaxiality parameters calculated from the shape tensor and MCMC deprojection. They gray region shows where the two methods qualitatively agree on morphology.

4.4.2 The $\epsilon - \Sigma_*$ Correlation

In a study of dwarf spheroidals (Dspfs) within the Local Group (LG), Xu et al. [335] illustrate a method of inferring 3D morphologies from projected observables. In Section 2, the authors outline how a galaxy's ellipticity ($\epsilon \equiv 1 - q$) and central surface brightness (Σ_*) are functions purely of the angle of observation (θ, ϕ) and the intrinsic 3D morphology (Q, S , and central density). Their modeling reveals that, under specific morphologies, ϵ and Σ_* yield a strong correlation. More specifically, a strong positive (negative) $\epsilon - \Sigma_*$ correlation indicates an overall oblate (prolate) morphology within the population. This correlation is quantified via a correlation coefficient defined by

$$r_{\epsilon\Sigma_*} = \frac{\sum_i (\epsilon_i - \bar{\epsilon})(\Sigma_{*,i} - \bar{\Sigma}_*)}{\sqrt{\sum_i (\epsilon_i - \bar{\epsilon})^2 \sum_i (\Sigma_{*,i} - \bar{\Sigma}_*)^2}} \quad (4.12)$$

where a bar indicates the arithmetic average. The authors apply this calculation to a sample of 26 Dspfs within the LG (see Table 1 in Xu et al. [335] for details), as well as a sample of 14 dwarf cosmological zoom-in simulations from the Feedback In Realistic Environments (FIRE) project [358, 359].

Here, we apply this correlation measurement to our own sample of simulated galaxies. When analyzing the FIRE galaxies, Xu et al. [335] randomly orient their sample before projecting into the 2D plane and taking a measurement of $r_{\epsilon\Sigma_*}$ for the population. This process is repeated 10^5 times in order to construct a distribution of correlation coefficients and compare it to the results of the LG Dspfs (Figure 7 in Xu et al. [335]). Following this procedure, we have constructed an $r_{\epsilon\Sigma_*}$ distribution for our own galaxies, and we compare our results directly to

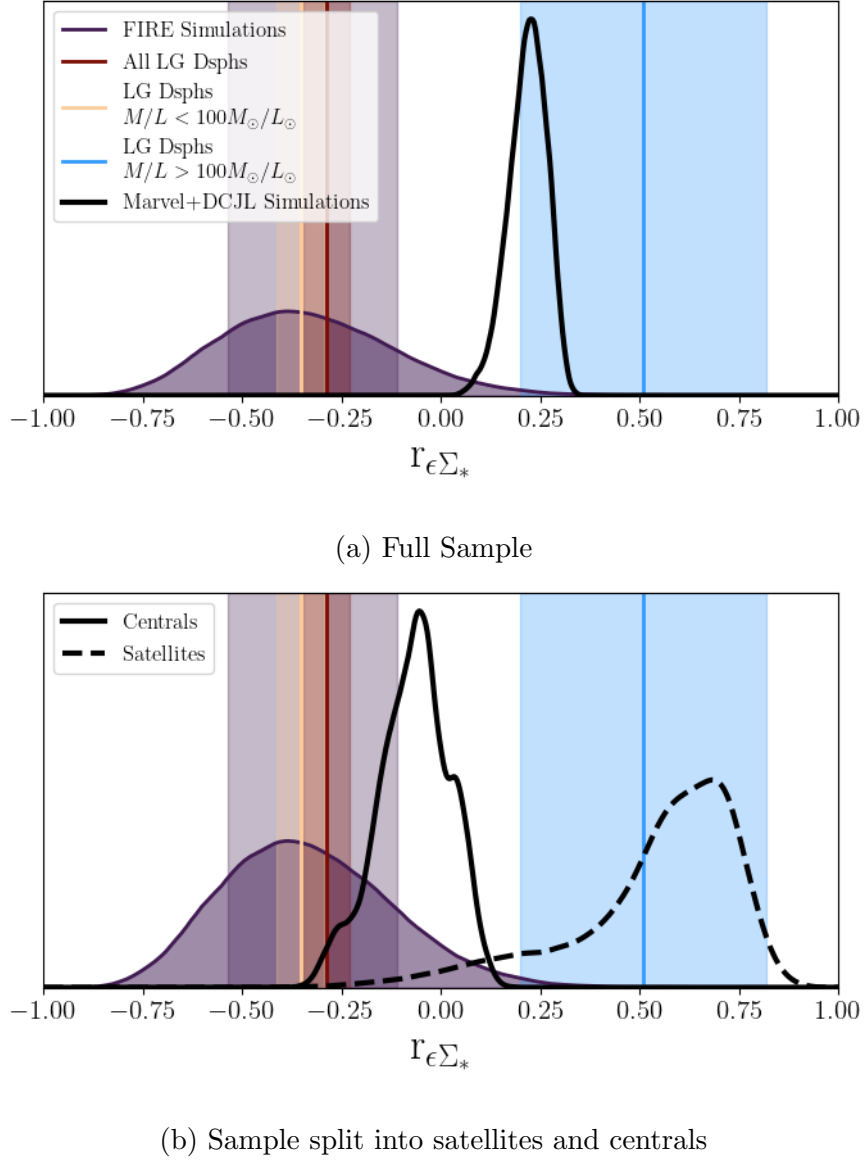


Figure 4.6: Measurements of the $r_{\epsilon\Sigma_*}$ -distribution for (a) our full sample and (b) our sample separated into satellites and centrals. Our data is compared directly to that of Xu et al. [335] (Figure 7). Our whole sample sits in the triaxial/oblate boundary space, while the FIRE sample is largely prolate. However, when splitting by environment, we see our satellite population is largely oblate while our centrals are predominantly triaxial.

those of Xu et al. [335] in Figure 4.6(a). Immediately, we see that our distribution is notably more concentrated and triaxial than the broad, prolate results of FIRE. In regards to the LG Dsphs, Xu et al. [335] found that they were largely prolate ($r_{\epsilon\Sigma_*} = -0.287 \pm 0.058$), which was in good agreement with the FIRE results ($r_{\epsilon\Sigma_*} = -0.322 \pm 0.213$). However, the authors found that within the LG Dsphs, there was a “dim” subset (defined as having M_{dyn}/L_V within one effective radius of over $100 M_\odot/L_\odot$) whose $r_{\epsilon\Sigma_*}$ values were notably more positive than their “bright” counterparts, indicating an oblate morphology. A thorough testing of possible explanations led the authors to believe these dim Dsphs are a true, morphologically distinct subset of oblate dwarf galaxies not found in cosmological simulations.

Unfortunately, the selection criteria from Section 4.2.2 removed all of our galaxies that meet the “dim” criteria. However, since this method of shape measurement only requires isophote fitting, we can relax our sample to consider all galaxies that are resolved enough to generate V -band luminosity density images. Doing so increases our sample to ~ 95 galaxies, ~ 26 of which meet the dim criteria (the numbers vary depending on the particular orientations drawn for each galaxy). In splitting our sample into bright and dim populations, we find that the dim population has a higher correlation coefficient, but not by a significant margin: $r_{\epsilon\Sigma_*}^{\text{bright}} = 0.079$ and $r_{\epsilon\Sigma_*}^{\text{dim}} = 0.157$; nowhere near the 0.862 difference observed in the LG Dsphs. Interestingly, if we separate our original sample into centrals and satellites, rather than bright and dim (Figure 4.6(b)), we find results similar to [335]. Our satellites show a significantly more positive $r_{\epsilon\Sigma_*}$ -distribution

than that of our centrals, which now appear more firmly triaxial (if not slightly prolate). While our centrals still yield more positive $r_{\epsilon\Sigma_*}$ values than that of FIRE, we have isolated a sample of significantly oblate galaxies whose $r_{\epsilon\Sigma_*}$ -distribution peak is higher than that of the dim LG Dsphs.

This method of measuring correlation coefficients, by necessity, operates on a population of galaxies, rather than a singular one, as multiple data points are required to compute a correlation. However, by treating our ensemble of isophotes from different orientations as a population, as we did in Section 4.4.1, we can use this method to obtain a qualitative measure of 3D morphology for all of our individual galaxies. Figure 4.7 shows the $r_{\epsilon\Sigma_*}$ values for our individual galaxies as a function of their stellar mass, as well as their triaxiality parameter as derived from the shape tensor. We see similar results here as we did in Figure 4.4, where the bulk of our galaxies above $M_* \sim 10^8 M_\odot$ are exhibiting a more oblate morphology, and, unsurprisingly, many of these galaxies are satellites. Below this mass threshold, our galaxies are fairly homogeneously spread around all $r_{\epsilon\Sigma_*}$ -values. This is slightly at odds with our T_S results from Figure 4.4, where there were no oblate morphologies at the lower-mass end of our sample. In looking at the direct comparison of $r_{\epsilon\Sigma_*}$ to T_S in the right side of Figure 4.7, we see general agreement on when the two methods are identifying an oblate, prolate, or triaxial galaxy (as indicated by the shaded gray band). There are, however, a notable few galaxies that the $r_{\epsilon\Sigma_*}$ measurements would identify as more oblate than the T_S measurements. These are primarily the aforementioned oblate, low-mass galaxies in Figure 4.7 that are more prolate in Figure 4.4.

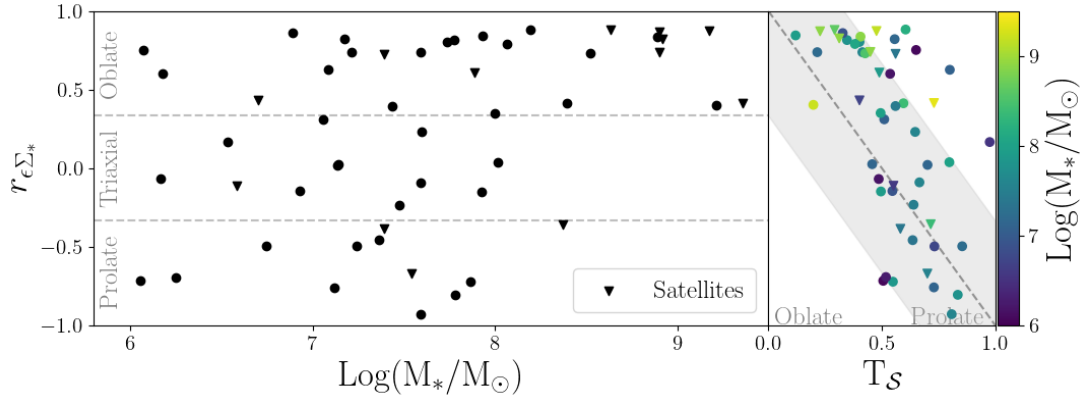


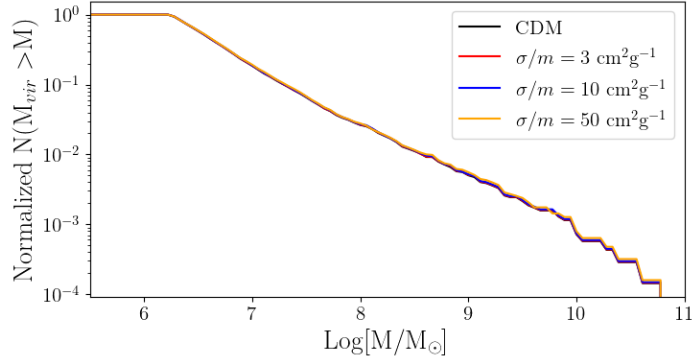
Figure 4.7: Measurements of $r_{\epsilon\Sigma_*}$ for individual galaxies as a function of stellar mass and the triaxiality parameter derived from the shape tensor. Satellite galaxies are denoted with triangles, and the gray band indicates when the values are in qualitative agreement on morphology. We see that a majority of the galaxies above $M_* = 10^8 M_\odot$ (most of which are satellites) reflect an oblate morphology, while those with lower masses show an even distribution across all $r_{\epsilon\Sigma_*}$ -values. The $r_{\epsilon\Sigma_*}$ -based morphologies and T_S -based morphologies are generally in good agreement with which halos are oblate, triaxial, or prolate. There are, however, a few, mostly low-mass, galaxies in the upper right hand corner of the subplot where the $r_{\epsilon\Sigma_*}$ value indicates a more oblate morphology than T_S .

4.5 Comparisons to SIDM

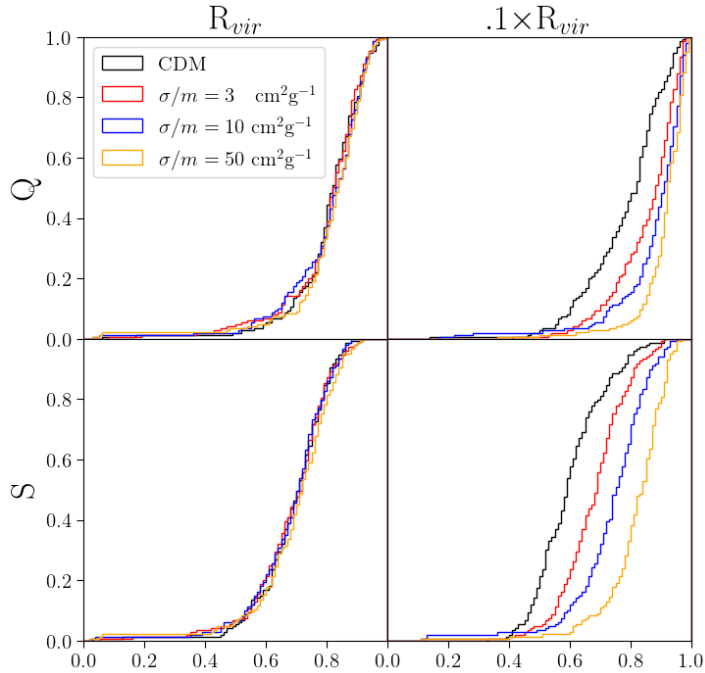
In addition to being run in a Λ CDM cosmology, the Storm simulation has also been run in SIDM with dark matter only. To date, we have tested various constant SIDM cross sections of interactions, and have preliminary results for $\sigma/m = 3, 10,$ and $50 \text{ cm}^2\text{g}^{-1}$. In Figure 4.8(a), we show the normalized halo mass functions for our CDM and various SIDM simulations, both types run only with dark matter. We see that all interaction cross sections perfectly recover the CDM mass function, indicating that there is no significant halo loss from internal interactions.

Following the process outlined in Section 4.3.2, we calculate the shape tensor for our dark matter halos, and show the Q and S axis ratio distributions in Figure 4.8(b). These calculations were performed at both the edge of the halo (R_{vir}) and the inner region ($.1R_{\text{vir}}$). In looking at the R_{vir} distributions, we see that the CDM and various SIDM models are moderately triaxial (median $(Q, S) \approx (.85, .7)$) and largely indistinguishable from one another. In looking at the inner region, we see that the CDM distribution becomes even more triaxial, with median $(Q, S) \approx (.8, .6)$. The inner SIDM distributions, however, become more spherical, with Q and S both moving towards unity. There is also a clear trend with interaction cross section, as the $50 \text{ cm}^2\text{g}^{-1}$ distribution is notably more spherical than the $3 \text{ cm}^2\text{g}^{-1}$ distribution.

These results are somewhat in agreement with Colín et al. [169], who find that the cores of SIDM halos are rounder than their CDM counterparts, but are not spherical. Interestingly, Colín et al. found that the more rounded nature of SIDM



(a) Normalized Halo Mass Function



(b) Comparisons of Shape at R_{vir} and $.1R_{vir}$

Figure 4.8: **(a)** The normalized halo mass functions of our CDM and various SIDM runs. **(b)** Comparisons of the cumulative Q - and S -distributions for our CDM and various SIDM runs. Measurements were calculated via the shape tensor at R_{vir} and $.1R_{vir}$. While the mass functions and outer shapes for our CDM and SIDM halos are in perfect agreement, the shapes of the inner region get notably rounder (higher Q and S) as the SIDM cross section increases.

halos extended all the way to the virial radius, something we are decidedly not seeing. We note, however, the Colín et al. are using an SIDM prescription with a non-constant, velocity-dependent cross section, so our comparison should not be taken as one-to-one. Both velocity-dependent cross sections, and SIDM simulations with full hydrodynamics are actively being worked on, and the question of whether the more spherical shapes remain is left for a future work.

4.6 Conclusions

Utilizing a sample of 51 high-resolution dwarf galaxies from the Marvel and DCJL zoom-in simulations, we perform a study of various methods for measuring morphology. We consider both observation-based methods based on isophote imaging and simulation-based methods using particle positions. Our results can be summarized as follows.

- Measurements of 2D morphology based on isophote fitting typically yield more elongated shapes when compared to projecting the intrinsic 3D shapes derived from the shape tensor, and this discrepancy increases with the inclination angle of the galaxy (see Figures 4.2 & 4.3).
- The triaxiality parameter (as derived from the shape tensor) for the morphologies of our galaxies typically follow the morphologies of their underlying dark matter halo (see Figure 4.4).
- The MCMC deprojection of isophote data outlined in Kado-Fong et al. [334] well recovers the parameter space occupied by shape tensor data, but the

individual deprojections are typically more prolate due to the isophote/shape tensor discrepancy (see Figure 4.5).

- Using the correlation of ellipticity and central surface brightness outlined in Xu et al. [335] yields a measure of morphology in good agreement with the shape tensor, and we find that our satellite galaxies are significantly more oblate than the rest of our sample (see Figure 4.6 & 4.7).
- Our various methods of measuring 3D morphology indicate a population of oblate, high-mass galaxies that are predominantly satellites (see Figures 4.4, 4.5, & 4.7).
- Preliminary results of SIDM simulations with constant interaction cross sections indicate that the inner regions of SIDM halos are notably more spherical than their CDM counterparts (see Figure 4.8).

Velocity-dependent cross sections and baryonic physics are currently being implemented into our SIDM simulations, and will be discussed in a future work(s). If the CDM-SIDM shape disparity persists in dark matter, our results from Section 4.3.3 suggest that the stellar shape would likely exhibit the same disparity. By utilizing the various morphology measurements discussed in this paper, we can determine whether said disparity in stellar shape would likely be detectable by observations, and therefore serve as an observable signature of SIDM cosmology.

Chapter 5

Conclusions

5.1 Summary

This thesis present a study of dwarf galaxies within N-body+SPH simulations across various environments, classifications, and orientations. Throughout this work, the following questions were addressed:

Are ultra-diffuse galaxies a unique subset of dwarf galaxies, or the tail end of a distribution? Are there any observable properties or evolutionary differences that set them apart?

In Chapter 2, I show that UDGs' status as unique from standard dwarf galaxies is largely dependent on the definition used to identify them, as more permissive definitions can homogenize the two groups. Under more restrictive definitions, isolated UDGs set themselves apart via a unique formation mechanism through early, high-spin mergers, the footprint of which is left in their more oblate morphology.

How are satellite galaxies around Milky Way analogs impacted by their hosts' masses and environments? Are the satellite distributions of the Milky Way and M31 “normal” within the universe at-large?

In Chapter 3, I show that both satellite abundance and satellite quenched correlate positively with host mass, while environment may play a significant role in greater isolation than our sample provides. Additionally, being in a pair, such as the

Milky Way and M31, may yield a higher satellite quenched fraction. I show that the Milky Way and M31 are well explained by our simulated sample of analogs.

How do “observation-based” and “simulation-based” methods of shape measurement compare? Are observational methods of 3D shape inference able to well recover intrinsic stellar structure?

In Chapter 4, I show that the observation based method of isophote fitting typically return more elongated shapes than simulated method of shape tensor calculation. While observational methods of 3D shape inference can well recover the qualitative morphology of our galaxies (prolate, oblate, or triaxial; as defined by the shape tensor), there is some decent scatter on a galaxy-to-galaxy basis as these methods are derived from the more elongated isophote fits.

Beyond the above considerations, each chapter took a step towards answering one or more of the following questions:

How does one’s definition of an astronomical object affect the resultant population?

In Chapter 2, I show that slight variations in the criteria for identifying UDGs can have massive impacts on the resultant populations. In ROMULUS25 and ROMULUSC, the considered definitions alter the UDG count from as low as 354 to as high as 931. Under more permissive definitions, the UDG and non-UDG populations become homogenized, as shown in Figures 2.1 & 2.10 where the morphological tracers of the isolated UDGs’ unique formation channels are erased.

In Chapter 3, I show how variations in identifying Milky Way analogs, and

especially identifying their satellites, can alter the observed impacts an analog has on its satellite population. This is shown in Section 3.5.1 where I discuss how assigning satellites as being with 300 kpc of the host, rather than within the host's simulated virial radius, the trend between host mass and satellite abundance. Selecting on 300 kpc also seems to primarily remove starforming satellites from massive hosts, biasing the global quenched fraction high.

Does changing an objects orientation relative to the observer affect the conclusions drawn?

In Chapter 2, I show that identifying UDGs is inherently dependant on viewing orientation, and as such dwarf galaxies don't truly exist in a singular dichotomy of UDG or non-UDG, but rather this status is a function of viewing angle. In Figure 2.6, I show that this angular dependence is strongest in isolated dwarfs (regardless of UDG definition) and weakest in cluster dwarfs, consistent with their more oblate and spherical morphologies, respectively.

In Chapter 4, I show that measurements of projected morphology via isophote fitting tend to return more elongated shapes when compared to projections of the 3D shape tensor. As shown in Figures 4.2 & 4.3, this discrepancy is stronger at more edge-on orientations.

How can answering the above questions aid the efforts of observational astronomy?

In Chapter 2, I discuss how the multitude of open questions in the study of UDG formation are unlikely to be answered cohesively when various research groups are not recovering consistent populations of UDGs. While it is almost certain

that UDGs are not a singular population with one formation channel, identifying these channels will be difficult when using permissive UDG definitions. Further, the field-UDGs' unique formation channel of early, high-spin mergers is likely not detectable through observed morphologies, as when the UDG and non-UDG populations are randomly oriented, the resultant distributions of projected axis ratios are indistinguishable. The methods of 3D morphology inference outlined in Chapter 4, however, are a promising avenue to recovering this morphological tracer.

In Chapter 3, I show that the tensions between the SAGA and ELVES surveys' quenched fraction results are coming from low mass satellites ($M_* < 10^8 M_\odot$, Figure 3.7). In Section 3.5.1, I discuss how identifying satellites based on the observationally motivated cut of 300 kpc can impact the results. Finally, I show that environmental trends are possibly starting to appear at the isolated-end of our sample space, so future observations, such as the full data release of SAGA, may wish to focus on extremely isolated analogs to search for these trends.

In Chapter 4, I show that the observation-based shape measurement of isophote fitting returns systematically more elongated morphologies compared to intrinsic measurements of the 3D shape tensor. While the various tested methods of 3D shape inference show good qualitative agreement on the general morphologies of our galaxies, there is still decent scatter on an individual galaxy level as these inference methods are operating on isophote measurements. I also show that our simulations host a populations of oblate dwarf galaxies that reside in oblate dark matter halos.

5.2 Future Work

As discussed in Section 1.1.3, there exist degeneracies with how varying baryonic physics and dark matter models manifest, thus meticulous, high resolution simulations are needed to constrain properties of dark matter. In Section 4.5, I show that halo shapes within SIDM simulations could potentially provide such a constraint. Before this can happen, however, further developments need to be completed within our simulations. Namely, we are implementing a velocity-dependent cross section model, as it has become preferred over constant cross section models since constant cross sections of $\leq 0.1 \text{ cm}^2\text{g}^{-1}$ are required at galaxy cluster scales, while cross sections of $\approx 1 - 2 \text{ cm}^2\text{g}^{-1}$ are preferred at galaxy scales [360]. With the velocity-dependent cross section model implemented, we plan to re-simulate zoom-ins from the Marvel Suite, as well as the ROMULUS25 volume, in DMO, and eventually with the inclusion of baryons and hydrodynamics. While these new SIDM simulations will prove useful in a variety of ways, I am personally focused on implementing the morphology calculations from Chapter 4 to see if the shape discrepancy in dark matter persists, and whether or not it is reflected in the stellar morphologies. If the intrinsic 3D shape distributions of dwarf galaxies in SIDM is different than that of CDM, stellar morphology could serve as an observable indicator of SIDM. However, actually observing these shape distributions and comparing them to the simulated predictions is not as simple as it sounds. In Section 4.3.2, I show that observational based methods of shape measurement tend to return more elongated shapes compared to the intrinsic calculations done

in simulations. This incongruity will need to be further studied and quantified before any direct comparison between simulations and observations can be made. Additionally, it is possible that a 3D morphological difference will be lost when observed as 2D projections (see Figures 2.1 & 2.9 for an example). Therefore, methods of 3D shape inference, like those discussed in Section 4.4, must continue to be studied and refined.

In regards to Milky Way analogs, the upcoming final data release of the SAGA Survey can potentially shed light on the possible high isolation environmental effects shown in Chapter 3. In addition, the upcoming LSST project plans to survey satellite populations around hosts out to several Mpc, adding a new observational set alongside SAGA and ELVES to which we can compare our ROMULUS25 samples. Returning to the Milky Way itself, recall that its satellite population has been the cause of multiple CDM tensions. This will almost certainly continue to be the case, given LSST’s ability to image the Milky Way and its satellites with extreme precision. LSST is expected to test dark matter in a wide variety of methods (see [205] for a comprehensive list), many of which are focused on Milky Way satellites. As an example, spectroscopic follow up observations of LSST discovered satellites could detect exceptionally dense or exceptionally diffuse ultra-faint satellites, which could provide a measurement of the SIDM cross section at low velocities [178, 205]. This could be compared to a study of UDGs in an SIDM-run ROMULUS25, are study of the inner regions of Milky Way analog satellites within SIDM-run DCJL. Armed ever improving baryonic physics, observational constrains on dark matter, and growing observational comparison

samples, studying dwarf galaxies within cosmological simulations has become vital to our understanding of the universe.

References

- [1] G. R. Blumenthal, S. M. Faber, R. Flores, and J. R. Primack, *The Astrophysical Journal* **301**, 27 (1986).
- [2] S. D. M. White and M. J. Rees, *Monthly Notices of the Royal Astronomical Society* **183**, 341 (1978).
- [3] S. M. Fall and G. Efstathiou, *Monthly Notices of the Royal Astronomical Society* **193**, 189 (1980).
- [4] M. Davis, G. Efstathiou, C. S. Frenk, and S. D. M. White, *The Astrophysical Journal* **292**, 371 (1985).
- [5] C. S. Frenk, S. D. M. White, M. Davis, and G. Efstathiou, *The Astrophysical Journal* **327**, 507 (1988).
- [6] S. D. M. White and C. S. Frenk, *The Astrophysical Journal* **379**, 52 (1991).
- [7] V. Bromm, N. Yoshida, L. Hernquist, and C. F. McKee, *Nature* **459**, 49 (2009).
- [8] R. Barkana and A. Loeb, *Physics Reports* **349**, 125 (2001).
- [9] V. Bromm and R. B. Larson, *Annual Review of Astronomy & Astrophysics* **42**, 79 (2004).
- [10] R. J. Bouwens, G. D. Illingworth, P. A. Oesch, M. Trenti, I. Labb  , M. Franx, M. Stiavelli, C. M. Carollo, P. van Dokkum, and D. Magee, *The Astrophysical Journal Letters* **752**, L5 (2012).
- [11] H. Atek, J. Richard, M. Jauzac, J.-P. Kneib, P. Natarajan, M. Limousin, D. Schaerer, E. Jullo, H. Ebeling, E. Egami, and B. Clement, *The Astrophysical Journal* **814**, 69 (2015).
- [12] J. J. Dalcanton, *The Astrophysical Journal* **495**, 251 (1998).
- [13] R. B. Tully and J. R. Fisher, *Astronomy & Astrophysics* **54**, 661 (1977).
- [14] S. Shen, H. J. Mo, S. D. M. White, M. R. Blanton, G. Kauffmann, W. Voges, J. Brinkmann, and I. Csabai, *Monthly Notices of the Royal Astronomical Society* **343**, 978 (2003).
- [15] M. Bernardi, A. Meert, V. Vikram, M. Huertas-Company, S. Mei, F. Shankar, and R. K. Sheth, *Monthly Notices of the Royal Astronomical Society* **443**, 874 (2014).
- [16] J. Lequeux, M. Peimbert, J. F. Rayo, A. Serrano, and S. Torres-Peimbert, *Astronomy & Astrophysics* **80**, 155 (1979).

- [17] C. A. Tremonti, T. M. Heckman, G. Kauffmann, J. Brinchmann, S. Charlot, S. D. M. White, M. Seibert, E. W. Peng, D. J. Schlegel, A. Uomoto, M. Fukugita, and J. Brinkmann, *The Astrophysical Journal* **613**, 898 (2004).
- [18] B. H. Andrews and P. Martini, *The Astrophysical Journal* **765**, 140 (2013).
- [19] A. Toomre and J. Toomre, *The Astrophysical Journal* **178**, 623 (1972).
- [20] V. Springel, T. Di Matteo, and L. Hernquist, *Monthly Notices of the Royal Astronomical Society* **361**, 776 (2005).
- [21] A. Dressler, *The Astrophysical Journal* **236**, 351 (1980).
- [22] I. B. Zeldovich, J. Einasto, and S. F. Shandarin, *Nature* **300**, 407 (1982).
- [23] J. Einasto, A. A. Klypin, E. Saar, and S. F. Shandarin, *Monthly Notices of the Royal Astronomical Society* **206**, 529 (1984).
- [24] G. De Lucia and J. Blaizot, *Monthly Notices of the Royal Astronomical Society* **375**, 2 (2007).
- [25] A. V. Kravtsov and S. Borgani, *Annual Review of Astronomy & Astrophysics* **50**, 353 (2012).
- [26] R. R. Rojas, M. S. Vogeley, F. Hoyle, and J. Brinkmann, *The Astrophysical Journal* **617**, 50 (2004).
- [27] A. Drlica-Wagner, K. Bechtol, S. Mau, M. McNanna, E. O. Nadler, A. B. Pace, T. S. Li, A. Pieres, E. Rozo, J. D. Simon, A. R. Walker, R. H. Wechsler, T. M. C. Abbott, S. Allam, J. Annis, E. Bertin, D. Brooks, D. L. Burke, A. C. Rosell, M. Carrasco Kind, J. Carretero, M. Costanzi, L. N. da Costa, J. De Vicente, S. Desai, H. T. Diehl, P. Doel, T. F. Eifler, S. Everett, B. Flaugher, J. Frieman, J. García-Bellido, E. Gaztanaga, D. Gruen, R. A. Gruendl, J. Gschwend, G. Gutierrez, K. Honscheid, D. J. James, E. Krause, K. Kuehn, N. Kuropatkin, O. Lahav, M. A. G. Maia, J. L. Marshall, P. Melchior, F. Menanteau, R. Miquel, A. Palmese, A. A. Plazas, E. Sanchez, V. Scarpine, M. Schubnell, S. Serrano, I. Sevilla-Noarbe, M. Smith, E. Suchyta, G. Tarle, and DES Collaboration, *The Astrophysical Journal* **893**, 47 (2020).
- [28] E. P. Hubble, *The Astrophysical Journal* **64**, 321 (1926).
- [29] G. de Vaucouleurs, *The Astrophysical Journal* **128**, 465 (1958).
- [30] S. M. Faber and J. S. Gallagher, *The Astrophysical Journal* **204**, 365 (1976).
- [31] R. G. Bower, J. R. Lucey, and R. S. Ellis, *Monthly Notices of the Royal Astronomical Society* **254**, 601 (1992).
- [32] A. E. Evrard, T. J. MacFarland, H. M. P. Couchman, J. M. Colberg, N. Yoshida, S. D. M. White, A. Jenkins, C. S. Frenk, F. R. Pearce, J. A. Peacock, and P. A. Thomas, *The Astrophysical Journal* **573**, 7 (2002).

- [33] V. Springel, S. D. M. White, A. Jenkins, C. S. Frenk, N. Yoshida, L. Gao, J. Navarro, R. Thacker, D. Croton, J. Helly, J. A. Peacock, S. Cole, P. Thomas, H. Couchman, A. Evrard, J. Colberg, and F. Pearce, *Nature* **435**, 629 (2005).
- [34] J. Diemand, M. Kuhlen, and P. Madau, *The Astrophysical Journal* **667**, 859 (2007).
- [35] V. Springel, J. Wang, M. Vogelsberger, A. Ludlow, A. Jenkins, A. Helmi, J. F. Navarro, C. S. Frenk, and S. D. M. White, *Monthly Notices of the Royal Astronomical Society* **391**, 1685 (2008).
- [36] M. Boylan-Kolchin, V. Springel, S. D. M. White, A. Jenkins, and G. Lemson, *Monthly Notices of the Royal Astronomical Society* **398**, 1150 (2009).
- [37] R. Teyssier, S. Pires, S. Prunet, D. Aubert, C. Pichon, A. Amara, K. Benabed, S. Colombi, A. Refregier, and J. L. Starck, *Astronomy & Astrophysics*, **497**, 335 (2009).
- [38] A. Jenkins, C. S. Frenk, S. D. M. White, J. M. Colberg, S. Cole, A. E. Evrard, H. M. P. Couchman, and N. Yoshida, *Monthly Notices of the Royal Astronomical Society* **321**, 372 (2001).
- [39] M. S. Warren, K. Abazajian, D. E. Holz, and L. Teodoro, *The Astrophysical Journal* **646**, 881 (2006).
- [40] D. S. Reed, R. Bower, C. S. Frenk, A. Jenkins, and T. Theuns, *Monthly Notices of the Royal Astronomical Society* **374**, 2 (2007).
- [41] J. Tinker, A. V. Kravtsov, A. Klypin, K. Abazajian, M. Warren, G. Yepes, S. Gottlöber, and D. E. Holz, *The Astrophysical Journal* **688**, 709 (2008).
- [42] S. D. M. White, M. Davis, G. Efstathiou, and C. S. Frenk, *Nature* **330**, 451 (1987).
- [43] A. Jenkins, C. S. Frenk, F. R. Pearce, P. A. Thomas, J. M. Colberg, S. D. M. White, H. M. P. Couchman, J. A. Peacock, G. Efstathiou, and A. H. Nelson, *The Astrophysical Journal* **499**, 20 (1998).
- [44] O. Fakhouri and C.-P. Ma, *Monthly Notices of the Royal Astronomical Society* **386**, 577 (2008).
- [45] O. Fakhouri and C.-P. Ma, *Monthly Notices of the Royal Astronomical Society* **394**, 1825 (2009).
- [46] P. F. Hopkins, R. S. Somerville, T. J. Cox, L. Hernquist, S. Joge, D. Kereš, C.-P. Ma, B. Robertson, and K. Stewart, *Monthly Notices of the Royal Astronomical Society* **397**, 802 (2009).

- [47] O. Fakhouri, C.-P. Ma, and M. Boylan-Kolchin, Monthly Notices of the Royal Astronomical Society **406**, 2267 (2010).
- [48] J. F. Navarro, C. S. Frenk, and S. D. M. White, The Astrophysical Journal **490**, 493 (1997).
- [49] B. Moore, F. Governato, T. Quinn, J. Stadel, and G. Lake, The Astrophysical Journal Letters **499**, L5 (1998).
- [50] S. Ghigna, B. Moore, F. Governato, G. Lake, T. Quinn, and J. Stadel, The Astrophysical Journal **544**, 616 (2000).
- [51] J. F. Navarro, E. Hayashi, C. Power, A. R. Jenkins, C. S. Frenk, S. D. M. White, V. Springel, J. Stadel, and T. R. Quinn, Monthly Notices of the Royal Astronomical Society **349**, 1039 (2004).
- [52] L. Gao, J. F. Navarro, S. Cole, C. S. Frenk, S. D. M. White, V. Springel, A. Jenkins, and A. F. Neto, Monthly Notices of the Royal Astronomical Society **387**, 536 (2008).
- [53] M. S. Warren, P. J. Quinn, J. K. Salmon, and W. H. Zurek, The Astrophysical Journal **399**, 405 (1992).
- [54] S. Cole and C. Lacey, Monthly Notices of the Royal Astronomical Society **281**, 716 (1996).
- [55] J. S. Bullock, A. Dekel, T. S. Kolatt, A. V. Kravtsov, A. A. Klypin, C. Porciani, and J. R. Primack, The Astrophysical Journal **555**, 240 (2001).
- [56] Y. P. Jing and Y. Suto, The Astrophysical Journal **574**, 538 (2002).
- [57] P. Bett, V. Eke, C. S. Frenk, A. Jenkins, J. Helly, and J. Navarro, Monthly Notices of the Royal Astronomical Society **376**, 215 (2007).
- [58] B. Moore, S. Ghigna, F. Governato, G. Lake, T. Quinn, J. Stadel, and P. Tozzi, The Astrophysical Journal Letters **524**, L19 (1999).
- [59] A. Klypin, A. V. Kravtsov, O. Valenzuela, and F. Prada, The Astrophysical Journal **522**, 82 (1999).
- [60] A. V. Kravtsov, A. A. Berlind, R. H. Wechsler, A. A. Klypin, S. Gottlöber, B. Allgood, and J. R. Primack, The Astrophysical Journal **609**, 35 (2004).
- [61] A. Vale and J. P. Ostriker, Monthly Notices of the Royal Astronomical Society **353**, 189 (2004).
- [62] B. P. Moster, R. S. Somerville, C. Maulbetsch, F. C. van den Bosch, A. V. Macciò, T. Naab, and L. Oser, The Astrophysical Journal **710**, 903 (2010).
- [63] A. R. Wetzel and M. White, Monthly Notices of the Royal Astronomical Society **403**, 1072 (2010).

- [64] A. A. Berlind, V. K. Narayanan, and D. H. Weinberg, *The Astrophysical Journal* **549**, 688 (2001).
- [65] A. Cooray, *The Astrophysical Journal Letters* **576**, L105 (2002).
- [66] X. Yang, H. J. Mo, and F. C. van den Bosch, *Monthly Notices of the Royal Astronomical Society* **339**, 1057 (2003).
- [67] L. Wang, C. Li, G. Kauffmann, and G. De Lucia, *Monthly Notices of the Royal Astronomical Society* **371**, 537 (2006).
- [68] C. Conroy and R. H. Wechsler, *The Astrophysical Journal* **696**, 620 (2009).
- [69] H. J. Mo, S. Mao, and S. D. M. White, *Monthly Notices of the Royal Astronomical Society* **295**, 319 (1998).
- [70] G. Kauffmann, J. M. Colberg, A. Diaferio, and S. D. M. White, *Monthly Notices of the Royal Astronomical Society* **303**, 188 (1999).
- [71] V. Springel, S. D. M. White, G. Tormen, and G. Kauffmann, *Monthly Notices of the Royal Astronomical Society* **328**, 726 (2001).
- [72] S. Hatton, J. E. G. Devriendt, S. Ninin, F. R. Bouchet, B. Guiderdoni, and D. Vibert, *Monthly Notices of the Royal Astronomical Society* **343**, 75 (2003).
- [73] X. Kang, Y. P. Jing, H. J. Mo, and G. Börner, *The Astrophysical Journal* **631**, 21 (2005).
- [74] R. G. Bower, A. J. Benson, R. Malbon, J. C. Helly, C. S. Frenk, C. M. Baugh, S. Cole, and C. G. Lacey, *Monthly Notices of the Royal Astronomical Society* **370**, 645 (2006).
- [75] R. S. Somerville, P. F. Hopkins, T. J. Cox, B. E. Robertson, and L. Hernquist, *Monthly Notices of the Royal Astronomical Society* **391**, 481 (2008).
- [76] Q. Guo, S. White, M. Boylan-Kolchin, G. De Lucia, G. Kauffmann, G. Lemson, C. Li, V. Springel, and S. Weinmann, *Monthly Notices of the Royal Astronomical Society* **413**, 101 (2011).
- [77] N. Katz, L. Hernquist, and D. H. Weinberg, *The Astrophysical Journal Letters* **399**, L109 (1992).
- [78] N. Katz, D. H. Weinberg, and L. Hernquist, *The Astrophysical Journal Supplement* **105**, 19 (1996).
- [79] F. R. Pearce, A. Jenkins, C. S. Frenk, J. M. Colberg, S. D. M. White, P. A. Thomas, H. M. P. Couchman, J. A. Peacock, G. Efstathiou, and Virgo Consortium, *The Astrophysical Journal Letters* **521**, L99 (1999).

- [80] R. Cen and J. P. Ostriker, *The Astrophysical Journal* **538**, 83 (2000).
- [81] V. Springel and L. Hernquist, *Monthly Notices of the Royal Astronomical Society* **339**, 289 (2003).
- [82] J. W. Wadsley, J. Stadel, and T. Quinn, *New Astronomy* **9**, 137 (2004).
- [83] D. Kereš, N. Katz, D. H. Weinberg, and R. Davé, *Monthly Notices of the Royal Astronomical Society* **363**, 2 (2005).
- [84] D. Sijacki, V. Springel, T. Di Matteo, and L. Hernquist, *Monthly Notices of the Royal Astronomical Society* **380**, 877 (2007).
- [85] A. A. Berlind and D. H. Weinberg, *The Astrophysical Journal* **575**, 587 (2002).
- [86] Q. Guo, S. White, C. Li, and M. Boylan-Kolchin, *Monthly Notices of the Royal Astronomical Society* **404**, 1111 (2010).
- [87] B. P. Moster, T. Naab, and S. D. M. White, *Monthly Notices of the Royal Astronomical Society* **428**, 3121 (2013).
- [88] N. Yoshida, F. Stoehr, V. Springel, and S. D. M. White, *Monthly Notices of the Royal Astronomical Society* **335**, 762 (2002).
- [89] A. Saro, G. De Lucia, S. Borgani, and K. Dolag, *Monthly Notices of the Royal Astronomical Society* **406**, 729 (2010).
- [90] P. D. Mitchell, C. G. Lacey, C. D. P. Lagos, C. S. Frenk, R. G. Bower, S. Cole, J. C. Helly, M. Schaller, V. Gonzalez-Perez, and T. Theuns, *Monthly Notices of the Royal Astronomical Society* **474**, 492 (2018).
- [91] L. Wang, D. Xu, L. Gao, Q. Guo, Y. Qu, and J. Pan, *Monthly Notices of the Royal Astronomical Society* **485**, 2083 (2019).
- [92] M. Ayromlou, D. Nelson, R. M. Yates, G. Kauffmann, M. Renneby, and S. D. M. White, *Monthly Notices of the Royal Astronomical Society* **502**, 1051 (2021).
- [93] O. Y. Gnedin and H. Zhao, *Monthly Notices of the Royal Astronomical Society* **333**, 299 (2002).
- [94] J. A. Sellwood and S. S. McGaugh, *The Astrophysical Journal* **634**, 70 (2005).
- [95] S. Mashchenko, J. Wadsley, and H. M. P. Couchman, *Science* **319**, 174 (2008).
- [96] S. Pedrosa, P. B. Tissera, and C. Scannapieco, *Monthly Notices of the Royal Astronomical Society* **395**, L57 (2009).

- [97] F. Governato, C. Brook, L. Mayer, A. Brooks, G. Rhee, J. Wadsley, P. Jonsson, B. Willman, G. Stinson, T. Quinn, and P. Madau, *Nature* **463**, 203 (2010).
- [98] L. B. Lucy, *Astronomical Journal*, **82**, 1013 (1977).
- [99] R. A. Gingold and J. J. Monaghan, *Monthly Notices of the Royal Astronomical Society* **181**, 375 (1977).
- [100] M. J. Berger and J. Oliger, *Journal of Computational Physics* **53**, 484 (1984).
- [101] M. J. Berger and P. Colella, *Journal of Computational Physics* **82**, 64 (1989).
- [102] G. L. Bryan and M. L. Norman, in *Computational Astrophysics; 12th Kingston Meeting on Theoretical Astrophysics*, Vol. 12 of *Astronomical Society of the Pacific Conference Series*, edited by D. A. Clarke and M. J. West (-, -, 1997), p. 363.
- [103] B. Fryxell, K. Olson, P. Ricker, F. X. Timmes, M. Zingale, D. Q. Lamb, P. MacNeice, R. Rosner, J. W. Truran, and H. Tufo, *The Astrophysical Journal Supplement* **131**, 273 (2000).
- [104] R. Teyssier, *Astronomy & Astrophysics* **385**, 337 (2002).
- [105] V. Springel and L. Hernquist, *Monthly Notices of the Royal Astronomical Society* **333**, 649 (2002).
- [106] J. W. Wadsley, B. W. Keller, and T. R. Quinn, *Monthly Notices of the Royal Astronomical Society* **471**, 2357 (2017).
- [107] V. Springel, *Monthly Notices of the Royal Astronomical Society* **401**, 791 (2010).
- [108] P. F. Hopkins, *Monthly Notices of the Royal Astronomical Society* **450**, 53 (2015).
- [109] A. M. Brooks, F. Governato, C. M. Booth, B. Willman, J. P. Gardner, J. Wadsley, G. Stinson, and T. Quinn, *The Astrophysical Journal Letters* **655**, L17 (2007).
- [110] A. M. Brooks, A. R. Solomon, F. Governato, J. McCleary, L. A. MacArthur, C. B. A. Brook, P. Jonsson, T. R. Quinn, and J. Wadsley, *The Astrophysical Journal* **728**, 51 (2011).
- [111] F. Munshi, F. Governato, A. M. Brooks, C. Christensen, S. Shen, S. Loebman, B. Moster, T. Quinn, and J. Wadsley, *The Astrophysical Journal* **766**, 56 (2013).

- [112] H. Menon, L. Wesolowski, G. Zheng, P. Jetley, L. Kale, T. Quinn, and F. Governato, Computational Astrophysics and Cosmology **2**, 1 (2015).
- [113] M. Tremmel, M. Karcher, F. Governato, M. Volonteri, T. R. Quinn, A. Pontzen, L. Anderson, and J. Bellovary, Monthly Notices of the Royal Astronomical Society **470**, 1121 (2017).
- [114] M. Tremmel, T. R. Quinn, A. Ricarte, A. Babul, U. Chadaayammuri, P. Natarajan, D. Nagai, A. Pontzen, and M. Volonteri, Monthly Notices of the Royal Astronomical Society **483**, 3336 (2019).
- [115] Planck Collaboration, P. A. R. Ade, N. Aghanim, C. Armitage-Caplan, M. Arnaud, M. Ashdown, F. Atrio-Barandela, J. Aumont, C. Baccigalupi, A. J. Banday, R. B. Barreiro, J. G. Bartlett, E. Battaner, K. Benabed, A. Benoît, A. Benoit-Lévy, J. P. Bernard, M. Bersanelli, P. Bielewicz, J. Bobin, J. J. Bock, A. Bonaldi, J. R. Bond, J. Borrill, F. R. Bouchet, M. Bridges, M. Bucher, C. Burigana, R. C. Butler, E. Calabrese, B. Cappellini, J. F. Cardoso, A. Catalano, A. Challinor, A. Chamballu, R. R. Chary, X. Chen, H. C. Chiang, L. Y. Chiang, P. R. Christensen, S. Church, D. L. Clements, S. Colombi, L. P. L. Colombo, F. Couchot, A. Coulais, B. P. Crill, A. Curto, F. Cuttaia, L. Danese, R. D. Davies, R. J. Davis, P. de Bernardis, A. de Rosa, G. de Zotti, J. Delabrouille, J. M. Delouis, F. X. Désert, C. Dickinson, J. M. Diego, K. Dolag, H. Dole, S. Donzelli, O. Doré, M. Douspis, J. Dunkley, X. Dupac, G. Efstathiou, F. Elsner, T. A. Enßlin, H. K. Eriksen, F. Finelli, O. Forni, M. Frailis, A. A. Fraisse, E. Franceschi, T. C. Gaier, S. Galeotta, S. Galli, K. Ganga, M. Giard, G. Giardino, Y. Giraud-Héraud, E. Gjerløw, J. González-Nuevo, K. M. Górski, S. Gratton, A. Gregorio, A. Gruppuso, J. E. Gudmundsson, J. Haissinski, J. Hamann, F. K. Hansen, D. Hanson, D. Harrison, S. Henrot-Versillé, C. Hernández-Monteagudo, D. Herranz, S. R. Hildebrandt, E. Hivon, M. Hobson, W. A. Holmes, A. Hornstrup, Z. Hou, W. Hovest, K. M. Huffenberger, A. H. Jaffe, T. R. Jaffe, J. Jewell, W. C. Jones, M. Juvela, E. Keihänen, R. Keskitalo, T. S. Kisner, R. Kneissl, J. Knoche, L. Knox, M. Kunz, H. Kurki-Suonio, G. Lagache, A. Lähteenmäki, J. M. Lamarre, A. Lasenby, M. Lattanzi, R. J. Laureijs, C. R. Lawrence, S. Leach, J. P. Leahy, R. Leonardi, J. León-Tavares, J. Lesgourgues, A. Lewis, M. Liguori, P. B. Lilje, M. Linden-Vørnle, M. López-Caniego, P. M. Lubin, J. F. Macías-Pérez, B. Maffei, D. Maino, N. Mandlesi, M. Maris, D. J. Marshall, P. G. Martin, E. Martínez-González, S. Masi, M. Massardi, S. Matarrese, F. Matthai, P. Mazzotta, P. R. Meinhold, A. Melchiorri, J. B. Melin, L. Mendes, E. Menegoni, A. Mennella, M. Migliaccio, M. Millea, S. Mitra, M. A. Miville-Deschénes, A. Moneti, L. Montier, G. Morgante, D. Mortlock, A. Moss, D. Munshi, J. A. Murphy, P. Naselsky, F. Nati, P. Natoli, C. B. Netterfield, H. U. Nørgaard-Nielsen, F. Noviello, D. Novikov, I. Novikov, I. J. O'Dwyer, S. Osborne, C. A. Oxborrow, F. Paci, L. Pagano, F. Pajot, R. Paladini, D. Paoletti, B. Partridge, F. Pasian, G. Patanchon, D. Pearson, T. J. Pearson, H. V. Peiris, O. Perdereau, L.

- Perotto, F. Perrotta, V. Pettorino, F. Piacentini, M. Piat, E. Pierpaoli, D. Pietrobon, S. Plaszczynski, P. Platania, E. Pointecouteau, G. Polenta, N. Ponthieu, L. Popa, T. Poutanen, G. W. Pratt, G. Prézeau, S. Prunet, J. L. Puget, J. P. Rachen, W. T. Reach, R. Rebolo, M. Reinecke, M. Remazeilles, C. Renault, S. Ricciardi, T. Riller, I. Ristorcelli, G. Rocha, C. Rosset, G. Roudier, M. Rowan-Robinson, J. A. Rubiño-Martín, B. Rusholme, M. Sandri, D. Santos, M. Savelainen, G. Savini, D. Scott, M. D. Seiffert, E. P. S. Shellard, L. D. Spencer, J. L. Starck, V. Stolyarov, R. Stompor, R. Sudiwala, R. Sunyaev, F. Sureau, D. Sutton, A. S. Suur-Uski, J. F. Sygnet, J. A. Tauber, D. Tavagnacco, L. Terenzi, L. Toffolatti, M. Tomasi, M. Tristram, M. Tucci, J. Tuovinen, M. Türler, G. Umana, L. Valenziano, J. Valiviita, B. Van Tent, P. Vielva, F. Villa, N. Vittorio, L. A. Wade, B. D. Wandelt, I. K. Wehus, M. White, S. D. M. White, A. Wilkinson, D. Yvon, A. Zacchei, and A. Zonca, *Astronomy & Astrophysics* **571**, A16 (2014).
- [116] F. Munshi, A. M. Brooks, E. Applebaum, C. R. Christensen, T. Quinn, and S. Sligh, *The Astrophysical Journal* **923**, 35 (2021).
- [117] D. N. Spergel, R. Bean, O. Doré, M. R. Nolta, C. L. Bennett, J. Dunkley, G. Hinshaw, N. Jarosik, E. Komatsu, L. Page, H. V. Peiris, L. Verde, M. Halpern, R. S. Hill, A. Kogut, M. Limon, S. S. Meyer, N. Odegard, G. S. Tucker, J. L. Weiland, E. Wollack, and E. L. Wright, *The Astrophysical Journal Supplement* **170**, 377 (2007).
- [118] Planck Collaboration, P. A. R. Ade, N. Aghanim, M. Arnaud, M. Ashdown, J. Aumont, C. Baccigalupi, A. J. Banday, R. B. Barreiro, J. G. Bartlett, and et al., *Astronomy & Astrophysics* **594**, A13 (2016).
- [119] C. B. Netterfield, P. A. R. Ade, J. J. Bock, J. R. Bond, J. Borrill, A. Boscaleri, K. Coble, C. R. Contaldi, B. P. Crill, P. de Bernardis, P. Farese, K. Ganga, M. Giacometti, E. Hivon, V. V. Hristov, A. Iacoangeli, A. H. Jaffe, W. C. Jones, A. E. Lange, L. Martinis, S. Masi, P. Mason, P. D. Mauskopf, A. Melchiorri, T. Montroy, E. Pascale, F. Piacentini, D. Pogosyan, F. Pongetti, S. Prunet, G. Romeo, J. E. Ruhl, and F. Scaramuzzi, *The Astrophysical Journal* **571**, 604 (2002).
- [120] J. Dunkley, E. Komatsu, M. R. Nolta, D. N. Spergel, D. Larson, G. Hinshaw, L. Page, C. L. Bennett, B. Gold, N. Jarosik, J. L. Weiland, M. Halpern, R. S. Hill, A. Kogut, M. Limon, S. S. Meyer, G. S. Tucker, E. Wollack, and E. L. Wright, *The Astrophysical Journal Supplement* **180**, 306 (2009).
- [121] M. Tegmark, M. R. Blanton, M. A. Strauss, F. Hoyle, D. Schlegel, R. Scoccimarro, M. S. Vogeley, D. H. Weinberg, I. Zehavi, A. Berlind, T. Budavari, A. Connolly, D. J. Eisenstein, D. Finkbeiner, J. A. Frieman, J. E. Gunn, A. J. S. Hamilton, L. Hui, B. Jain, D. Johnston, S. Kent, H. Lin, R. Nakajima, R. C. Nichol, J. P. Ostriker, A. Pope, R. Scranton, U. Seljak, R. K. Sheth, A. Stebbins, A. S. Szalay, I. Szapudi, L. Verde, Y.

- Xu, J. Annis, N. A. Bahcall, J. Brinkmann, S. Burles, F. J. Castander, I. Csabai, J. Loveday, M. Doi, M. Fukugita, I. Gott, J. Richard, G. Hennessy, D. W. Hogg, Ž. Ivezić, G. R. Knapp, D. Q. Lamb, B. C. Lee, R. H. Lupton, T. A. McKay, P. Kunszt, J. A. Munn, L. O'Connell, J. Peoples, J. R. Pier, M. Richmond, C. Rockosi, D. P. Schneider, C. Stoughton, D. L. Tucker, D. E. Vanden Berk, B. Yanny, D. G. York, and SDSS Collaboration, *The Astrophysical Journal* **606**, 702 (2004).
- [122] S. Cole, W. J. Percival, J. A. Peacock, P. Norberg, C. M. Baugh, C. S. Frenk, I. Baldry, J. Bland-Hawthorn, T. Bridges, R. Cannon, M. Colless, C. Collins, W. Couch, N. J. G. Cross, G. Dalton, V. R. Eke, R. De Propris, S. P. Driver, G. Efstathiou, R. S. Ellis, K. Glazebrook, C. Jackson, A. Jenkins, O. Lahav, I. Lewis, S. Lumsden, S. Maddox, D. Madgwick, B. A. Peterson, W. Sutherland, and K. Taylor, *Monthly Notices of the Royal Astronomical Society* **362**, 505 (2005).
 - [123] P. Paschos, T. Jena, D. Tytler, D. Kirkman, and M. L. Norman, *Monthly Notices of the Royal Astronomical Society* **399**, 1934 (2009).
 - [124] M. Viel, J. S. Bolton, and M. G. Haehnelt, *Monthly Notices of the Royal Astronomical Society* **399**, L39 (2009).
 - [125] G. Kauffmann, S. D. M. White, and B. Guiderdoni, *Monthly Notices of the Royal Astronomical Society* **264**, 201 (1993).
 - [126] T. Sakamoto and T. Hasegawa, *The Astrophysical Journal Letters* **653**, L29 (2006).
 - [127] D. B. Zucker, V. Belokurov, N. W. Evans, J. T. Kleyna, M. J. Irwin, M. I. Wilkinson, M. Fellhauer, D. M. Bramich, G. Gilmore, H. J. Newberg, B. Yanny, J. A. Smith, P. C. Hewett, E. F. Bell, H. W. Rix, O. Y. Gnedin, S. Vidrih, R. F. G. Wyse, B. Willman, E. K. Grebel, D. P. Schneider, T. C. Beers, A. Y. Kniazev, J. C. Barentine, H. Brewington, J. Brinkmann, M. Harvanek, S. J. Kleinman, J. Krzesinski, D. Long, A. Nitta, and S. A. Snedden, *The Astrophysical Journal Letters* **650**, L41 (2006).
 - [128] B. Willman, J. J. Dalcanton, D. Martinez-Delgado, A. A. West, M. R. Blanton, D. W. Hogg, J. C. Barentine, H. J. Brewington, M. Harvanek, S. J. Kleinman, J. Krzesinski, D. Long, J. Neilsen, Eric H., A. Nitta, and S. A. Snedden, *The Astrophysical Journal Letters* **626**, L85 (2005).
 - [129] J. Diemand, M. Kuhlen, and P. Madau, *The Astrophysical Journal* **657**, 262 (2007).
 - [130] M. Kuhlen, J. Diemand, and P. Madau, *The Astrophysical Journal* **686**, 262 (2008).
 - [131] P. Madau, J. Diemand, and M. Kuhlen, *The Astrophysical Journal* **679**, 1260 (2008).

- [132] M. Boylan-Kolchin, J. S. Bullock, and M. Kaplinghat, Monthly Notices of the Royal Astronomical Society **415**, L40 (2011).
- [133] E. Papastergis, A. M. Martin, R. Giovanelli, and M. P. Haynes, The Astrophysical Journal **739**, 38 (2011).
- [134] A. Klypin, I. Karachentsev, D. Makarov, and O. Nasonova, Monthly Notices of the Royal Astronomical Society **454**, 1798 (2015).
- [135] J. I. Read, M. I. Wilkinson, N. W. Evans, G. Gilmore, and J. T. Kleyna, Monthly Notices of the Royal Astronomical Society **367**, 387 (2006).
- [136] M. Boylan-Kolchin, J. S. Bullock, and M. Kaplinghat, Monthly Notices of the Royal Astronomical Society **422**, 1203 (2012).
- [137] E. J. Tollerud, M. Boylan-Kolchin, and J. S. Bullock, Monthly Notices of the Royal Astronomical Society **440**, 3511 (2014).
- [138] G. D. Martinez, Monthly Notices of the Royal Astronomical Society **451**, 2524 (2015).
- [139] M. Metz, P. Kroupa, and N. I. Libeskind, The Astrophysical Journal **680**, 287 (2008).
- [140] J. S. Bullock and M. Boylan-Kolchin, Annual Review of Astronomy and Astrophysics **55**, 343 (2017).
- [141] M. S. Pawłowski, Modern Physics Letters A **33**, 1830004 (2018).
- [142] L. V. Sales, A. Wetzel, and A. Fattahi, Nature Astronomy **6**, 897 (2022).
- [143] M. Cautun, S. Bose, C. S. Frenk, Q. Guo, J. Han, W. A. Hellwing, T. Sawala, and W. Wang, Monthly Notices of the Royal Astronomical Society **452**, 3838 (2015).
- [144] L. V. Sales and J. F. Navarro, Nature Astronomy **7**, 376 (2023).
- [145] B. Moore, Nature **370**, 629 (1994).
- [146] A. Burkert, The Astrophysical Journal Letters **447**, L25 (1995).
- [147] W. J. G. de Blok, S. S. McGaugh, A. Bosma, and V. C. Rubin, he Astrophysical Journal Letters **552**, L23 (2001).
- [148] J. D. Simon, A. D. Bolatto, A. Leroy, L. Blitz, and E. L. Gates, The Astrophysical Journal **621**, 757 (2005).
- [149] S.-H. Oh, C. Brook, F. Governato, E. Brinks, L. Mayer, W. J. G. de Blok, A. Brooks, and F. Walter, The Astronomical Journal **142**, 24 (2011).

- [150] B. Moore, T. Quinn, F. Governato, J. Stadel, and G. Lake, *Monthly Notices of the Royal Astronomical Society* **310**, 1147 (1999).
- [151] F. Governato, B. Willman, L. Mayer, A. Brooks, G. Stinson, O. Valenzuela, J. Wadsley, and T. Quinn, *Monthly Notices of the Royal Astronomical Society* **374**, 1479 (2007).
- [152] F. C. van den Bosch, X. Yang, H. J. Mo, S. M. Weinmann, A. V. Maccò, S. More, M. Cacciato, R. Skibba, and X. Kang, *Monthly Notices of the Royal Astronomical Society* **376**, 841 (2007).
- [153] A. A. Dutton, *Monthly Notices of the Royal Astronomical Society* **396**, 121 (2009).
- [154] J. T. Kleyna, M. I. Wilkinson, G. Gilmore, and N. W. Evans, *The Astrophysical Journal Letters* **588**, L21 (2003).
- [155] S. S. McGaugh, *Astronomical Journal* **143**, 40 (2012).
- [156] K. A. Oman, J. F. Navarro, A. Fattahi, C. S. Frenk, T. Sawala, S. D. M. White, R. Bower, R. A. Crain, M. Furlong, M. Schaller, J. Schaye, and T. Theuns, *Monthly Notices of the Royal Astronomical Society* **452**, 3650 (2015).
- [157] P. Bode, J. P. Ostriker, and N. Turok, *The Astrophysical Journal* **556**, 93 (2001).
- [158] P. Colín, V. Avila-Reese, and O. Valenzuela, *The Astrophysical Journal* **542**, 622 (2000).
- [159] J. Zavala, Y. P. Jing, A. Faltenbacher, G. Yepes, Y. Hoffman, S. Gottlöber, and B. Catinella, *The Astrophysical Journal* **700**, 1779 (2009).
- [160] A. V. Maccò and F. Fontanot, *Monthly Notices of the Royal Astronomical Society* **404**, L16 (2010).
- [161] M. Viel, G. D. Becker, J. S. Bolton, M. G. Haehnelt, M. Rauch, and W. L. W. Sargent, *Physical Review Letters* **100**, 041304 (2008).
- [162] A. Boyarsky, J. Lesgourgues, O. Ruchayskiy, and M. Viel, *Journal of Cosmology and Astroparticle Physics* **2009**, 012 (2009).
- [163] C. B. Brook and A. Di Cintio, *Monthly Notices of the Royal Astronomical Society* **453**, 2133 (2015).
- [164] F. Governato, D. Weisz, A. Pontzen, S. Loebman, D. Reed, A. M. Brooks, P. Behroozi, C. Christensen, P. Madau, L. Mayer, S. Shen, M. Walker, T. Quinn, B. W. Keller, and J. Wadsley, *Monthly Notices of the Royal Astronomical Society* **448**, 792 (2015).

- [165] D. N. Spergel and P. J. Steinhardt, Physical Review Letters **84**, 3760 (2000).
- [166] C. Firmani, E. D’Onghia, V. Avila-Reese, G. Chincarini, and X. Hernández, Monthly Notices of the Royal Astronomical Society **315**, L29 (2000).
- [167] N. Yoshida, V. Springel, S. D. M. White, and G. Tormen, The Astrophysical Journal Letters **544**, L87 (2000).
- [168] R. Davé, D. N. Spergel, P. J. Steinhardt, and B. D. Wandelt, The Astrophysical Journal **547**, 574 (2001).
- [169] P. Colín, V. Avila-Reese, O. Valenzuela, and C. Firmani, The Astrophysical Journal **581**, 777 (2002).
- [170] K. Ahn and P. R. Shapiro, Monthly Notices of the Royal Astronomical Society **363**, 1092 (2005).
- [171] S. Tulin and H.-B. Yu, Physics Reports **730**, 1 (2018).
- [172] M. Vogelsberger, J. Zavala, and A. Loeb, Monthly Notices of the Royal Astronomical Society **423**, 3740 (2012).
- [173] M. Rocha, A. H. G. Peter, J. S. Bullock, M. Kaplinghat, S. Garrison-Kimmel, J. Oñorbe, and L. A. Moustakas, Monthly Notices of the Royal Astronomical Society **430**, 81 (2013).
- [174] E. O. Nadler, A. Banerjee, S. Adhikari, Y.-Y. Mao, and R. H. Wechsler, The Astrophysical Journal **896**, 112 (2020).
- [175] A. Kamada, M. Kaplinghat, A. B. Pace, and H.-B. Yu, Physical Review Letters **119**, 111102 (2017).
- [176] P. Creasey, O. Sameie, L. V. Sales, H.-B. Yu, M. Vogelsberger, and J. Zavala, Monthly Notices of the Royal Astronomical Society **468**, 2283 (2017).
- [177] D. Lynden-Bell and R. Wood, Monthly Notices of the Royal Astronomical Society **138**, 495 (1968).
- [178] H. Nishikawa, K. K. Boddy, and M. Kaplinghat, Physical Review D **101**, 063009 (2020).
- [179] S. Balberg, S. L. Shapiro, and S. Inagaki, The Astrophysical Journal **568**, 475 (2002).
- [180] O. D. Elbert, J. S. Bullock, S. Garrison-Kimmel, M. Rocha, J. Oñorbe, and A. H. G. Peter, Monthly Notices of the Royal Astronomical Society **453**, 29 (2015).
- [181] R. Essig, S. D. McDermott, H.-B. Yu, and Y.-M. Zhong, Physical Review Letters **123**, 121102 (2019).

- [182] Z. C. Zeng, A. H. G. Peter, X. Du, A. Benson, S. Kim, F. Jiang, F.-Y. Cyr-Racine, and M. Vogelsberger, Monthly Notices of the Royal Astronomical Society **513**, 4845 (2022).
- [183] C. A. Correa, Monthly Notices of the Royal Astronomical Society **503**, 920 (2021).
- [184] F. Kahlhoefer, M. Kaplinghat, T. R. Slatyer, and C.-L. Wu, Journal of Cosmology and Astroparticle Physics **2019**, 010 (2019).
- [185] M. Kaplinghat, M. Valli, and H.-B. Yu, Monthly Notices of the Royal Astronomical Society **490**, 231 (2019).
- [186] O. Sameie, H.-B. Yu, L. V. Sales, M. Vogelsberger, and J. Zavala, Physical Review Letters **124**, 141102 (2020).
- [187] T. Quinn, N. Katz, and G. Efstathiou, Monthly Notices of the Royal Astronomical Society **278**, L49 (1996).
- [188] N. Y. Gnedin, The Astrophysical Journal **542**, 535 (2000).
- [189] D. C. Hambrick, J. P. Ostriker, P. H. Johansson, and T. Naab, Monthly Notices of the Royal Astronomical Society **413**, 2421 (2011).
- [190] M. Hoeft, G. Yepes, S. Gottlöber, and V. Springel, Monthly Notices of the Royal Astronomical Society **371**, 401 (2006).
- [191] T. Okamoto, L. Gao, and T. Theuns, Monthly Notices of the Royal Astronomical Society **390**, 920 (2008).
- [192] P. F. Hopkins, L. Hernquist, T. J. Cox, and D. Kereš, The Astrophysical Journal Supplement **175**, 356 (2008).
- [193] P. F. Hopkins, E. Quataert, and N. Murray, Monthly Notices of the Royal Astronomical Society **417**, 950 (2011).
- [194] C. B. Brook, F. Governato, R. Roškar, G. Stinson, A. M. Brooks, J. Wadsley, T. Quinn, B. K. Gibson, O. Snaith, K. Pilkington, E. House, and A. Pontzen, Monthly Notices of the Royal Astronomical Society **415**, 1051 (2011).
- [195] A. Pontzen and F. Governato, Monthly Notices of the Royal Astronomical Society **421**, 3464 (2012).
- [196] A. B. Fry, F. Governato, A. Pontzen, T. Quinn, M. Tremmel, L. Anderson, H. Menon, A. M. Brooks, and J. Wadsley, Monthly Notices of the Royal Astronomical Society **452**, 1468 (2015).

- [197] A. Drlica-Wagner, C. Prescod-Weinstein, H.-B. Yu, A. Albert, M. Amin, A. Banerjee, M. Baryakhtar, K. Bechtol, S. Bird, S. Birrer, T. Bringmann, R. Caputo, S. Chakrabarti, T. Y. Chen, D. Croon, F.-Y. Cyr-Racine, W. A. Dawson, C. Dvorkin, V. Gluscevic, D. Gilman, D. Grin, R. Hložek, R. K. Leane, T. S. Li, Y.-Y. Mao, J. Meyers, S. Mishra-Sharma, J. B. Muñoz, F. Munshi, E. O. Nadler, A. Parikh, K. Perez, A. H. G. Peter, S. Profumo, K. Schutz, N. Sehgal, J. D. Simon, K. Sinha, M. Valluri, and R. H. Wechsler, arXiv e-prints -, arXiv:2209.08215 (2022).
- [198] W. Hu, R. Barkana, and A. Gruzinov, Physical Review Letters **85**, 1158 (2000).
- [199] R. Cen, The Astrophysical Journal Letters **546**, L77 (2001).
- [200] M. Kaplinghat, L. Knox, and M. S. Turner, Physical Review Letters **85**, 3335 (2000).
- [201] B. Carr, F. Kühnel, and M. Sandstad, **94**, 083504 (2016).
- [202] S. Bird, A. Albert, W. Dawson, Y. Ali-Haïmoud, A. Coogan, A. Drlica-Wagner, Q. Feng, D. Inman, K. Inomata, E. Kovetz, A. Kusenko, B. V. Lehmann, J. B. Muñoz, R. Singh, V. Takhistov, and Y.-D. Tsai, Physics of the Dark Universe **41**, 101231 (2023).
- [203] L. F. Abbott and P. Sikivie, Physics Letters B **120**, 133 (1983).
- [204] N. Du, N. Force, R. Khatiwada, E. Lentz, R. Ottens, L. J. Rosenberg, G. Rybka, G. Carosi, N. Woollett, D. Bowring, A. S. Chou, A. Sonnenschein, W. Wester, C. Boutan, N. S. Oblath, R. Bradley, E. J. Daw, A. V. Dixit, J. Clarke, S. R. O’Kelley, N. Crisosto, J. R. Gleason, S. Jois, P. Sikivie, I. Stern, N. S. Sullivan, D. B. Tanner, G. C. Hilton, and ADMX Collaboration, Physical Review Letters **120**, 151301 (2018).
- [205] A. Drlica-Wagner, Y.-Y. Mao, S. Adhikari, R. Armstrong, A. Banerjee, N. Banik, K. Bechtol, S. Bird, K. K. Boddy, A. Bonaca, J. Bovy, M. R. Buckley, E. Bulbul, C. Chang, G. Chapline, J. Cohen-Tanugi, A. Cuoco, F.-Y. Cyr-Racine, W. A. Dawson, A. Díaz Rivero, C. Dvorkin, D. Erkal, C. D. Fassnacht, J. García-Bellido, M. Giannotti, V. Gluscevic, N. Golovich, D. Hendel, Y. D. Hezaveh, S. Horiuchi, M. J. Jee, M. Kaplinghat, C. R. Keeton, S. E. Koposov, C. Y. Lam, T. S. Li, J. R. Lu, R. Mandelbaum, S. D. McDermott, M. McNanna, M. Medford, M. Meyer, M. Marc, S. Murgia, E. O. Nadler, L. Necib, E. Nuss, A. B. Pace, A. H. G. Peter, D. A. Polin, C. Prescod-Weinstein, J. I. Read, R. Rosenfeld, N. Shipp, J. D. Simon, T. R. Slatyer, O. Straniero, L. E. Strigari, E. Tollerud, J. A. Tyson, M.-Y. Wang, R. H. Wechsler, D. Wittman, H.-B. Yu, G. Zaharijas, Y. Ali-Haïmoud, J. Annis, S. Birrer, R. Biswas, J. Blazek, A. M. Brooks, E. Buckley-Geer, R. Caputo, E. Charles, S. Digel, S. Dodelson, B. Flaugher, J. Frieman, E. Gawiser, A. P. Hearin, R. Hložek, B. Jain, T. E. Jeltema, S. M. Koushiappas,

- M. Lisanti, M. LoVerde, S. Mishra-Sharma, J. A. Newman, B. Nord, E. Nourbakhsh, S. Ritz, B. E. Robertson, M. A. Sánchez-Conde, A. Slosar, T. M. P. Tait, A. Verma, R. Vilalta, C. W. Walter, B. Yanny, and A. R. Zentner, arXiv e-prints **-**, arXiv:1902.01055 (2019).
- [206] Ž. Ivezić, S. M. Kahn, J. A. Tyson, B. Abel, E. Acosta, R. Allsman, D. Alonso, Y. AlSayyad, S. F. Anderson, J. Andrew, J. R. P. Angel, G. Z. Angeli, R. Ansari, P. Antilogus, C. Araujo, R. Armstrong, K. T. Arndt, P. Astier, É. Aubourg, N. Auza, T. S. Axelrod, D. J. Bard, J. D. Barr, A. Barrau, J. G. Bartlett, A. E. Bauer, B. J. Bauman, S. Baumont, E. Bechtol, K. Bechtol, A. C. Becker, J. Becla, C. Beldica, S. Bellavia, F. B. Bianco, R. Biswas, G. Blanc, J. Blazek, R. D. Blandford, J. S. Bloom, J. Bogart, T. W. Bond, M. T. Booth, A. W. Borgland, K. Borne, J. F. Bosch, D. Boutigny, C. A. Brackett, A. Bradshaw, W. N. Brandt, M. E. Brown, J. S. Bullock, P. Burchat, D. L. Burke, G. Cagnoli, D. Calabrese, S. Callahan, A. L. Callen, J. L. Carlin, E. L. Carlson, S. Chandrasekharan, G. Charles-Emerson, S. Chesley, E. C. Cheu, H.-F. Chiang, J. Chiang, C. Chirino, D. Chow, D. R. Ciardi, C. F. Claver, J. Cohen-Tanugi, J. J. Cockrum, R. Coles, A. J. Connolly, K. H. Cook, A. Cooray, K. R. Covey, C. Cribbs, W. Cui, R. Cutri, P. N. Daly, S. F. Daniel, F. Daruich, G. Daubard, G. Dauves, W. Dawson, F. Delgado, A. Dellapenna, R. de Peyster, M. de Val-Borro, S. W. Digel, P. Doherty, R. Dubois, G. P. Dubois-Felsmann, J. Durech, F. Economou, T. Eifler, M. Eracleous, B. L. Emmons, A. Fausti Neto, H. Ferguson, E. Figueroa, M. Fisher-Levine, W. Focke, M. D. Foss, J. Frank, M. D. Freeman, E. Gangler, E. Gawiser, J. C. Geary, P. Gee, M. Geha, C. J. B. Gessner, R. R. Gibson, D. K. Gilmore, T. Glanzman, W. Glick, T. Goldina, D. A. Goldstein, I. Goodenow, M. L. Graham, W. J. Gressler, P. Gris, L. P. Guy, A. Guyonnet, G. Haller, R. Harris, P. A. Hascall, J. Haupt, F. Hernandez, S. Herrmann, E. Hileman, J. Hoblitt, J. A. Hodgson, C. Hogan, J. D. Howard, D. Huang, M. E. Huffer, P. Ingraham, W. R. Innes, S. H. Jacoby, B. Jain, F. Jammes, M. J. Jee, T. Jenness, G. Jernigan, D. Jevremović, K. Johns, A. S. Johnson, M. W. G. Johnson, R. L. Jones, C. Juramy-Gilles, M. Jurić, J. S. Kalirai, N. J. Kallivayalil, B. Kalmbach, J. P. Kantor, P. Karst, M. M. Kasliwal, H. Kelly, R. Kessler, V. Kinnison, D. Kirkby, L. Knox, I. V. Kotov, V. L. Krabbendam, K. S. Krughoff, P. Kubánek, J. Kuczewski, S. Kulkarni, J. Ku, N. R. Kurita, C. S. Lage, R. Lambert, T. Lange, J. B. Langton, L. Le Guillou, D. Levine, M. Liang, K.-T. Lim, C. J. Lintott, K. E. Long, M. Lopez, P. J. Lotz, R. H. Lupton, N. B. Lust, L. A. MacArthur, A. Mahabal, R. Mandelbaum, T. W. Markiewicz, D. S. Marsh, P. J. Marshall, S. Marshall, M. May, R. McKercher, M. McQueen, J. Meyers, M. Migliore, M. Miller, D. J. Mills, C. Miraval, J. Moeyens, F. E. Moolekamp, D. G. Monet, M. Moniez, S. Monkewitz, C. Montgomery, C. B. Morrison, F. Mueller, G. P. Muller, F. Muñoz Arancibia, D. R. Neill, S. P. Newbry, J.-Y. Nief, A. Nomerotski, M. Nordby, P. O'Connor, J. Oliver, S. S. Olivier, K. Olsen, W. O'Mullane, S. Ortiz, S. Osier, R. E. Owen, R. Pain, P. E. Palecek, J. K.

- Parejko, J. B. Parsons, N. M. Pease, J. M. Peterson, J. R. Peterson, D. L. Petravick, M. E. Libby Petrick, C. E. Petry, F. Pierfederici, S. Pietrowicz, R. Pike, P. A. Pinto, R. Plante, S. Plate, J. P. Plutchak, P. A. Price, M. Prouza, V. Radeka, J. Rajagopal, A. P. Rasmussen, N. Regnault, K. A. Reil, D. J. Reiss, M. A. Reuter, S. T. Ridgway, V. J. Riot, S. Ritz, S. Robinson, W. Roby, A. Roodman, W. Rosing, C. Roucelle, M. R. Rumore, S. Russo, A. Saha, B. Sassolas, T. L. Schalk, P. Schellart, R. H. Schindler, S. Schmidt, D. P. Schneider, M. D. Schneider, W. Schoening, G. Schumacher, M. E. Schwamb, J. Sebag, B. Selvy, G. H. Sembroski, L. G. Seppala, A. Serio, E. Serrano, R. A. Shaw, I. Shipsey, J. Sick, N. Silvestri, C. T. Slater, J. A. Smith, R. C. Smith, S. Sobhani, C. Soldahl, L. Storrie-Lombardi, E. Stover, M. A. Strauss, R. A. Street, C. W. Stubbs, I. S. Sullivan, D. Sweeney, J. D. Swinbank, A. Szalay, P. Takacs, S. A. Tether, J. J. Thaler, J. G. Thayer, S. Thomas, A. J. Thornton, V. Thukral, J. Tice, D. E. Trilling, M. Turri, R. Van Berg, D. Vanden Berk, K. Vetter, F. Virieux, T. Vucina, W. Wahl, L. Walkowicz, B. Walsh, C. W. Walter, D. L. Wang, S.-Y. Wang, M. Warner, O. Wiecha, B. Willman, S. E. Winters, D. Wittman, S. C. Wolff, W. M. Wood-Vasey, X. Wu, B. Xin, P. Yoachim, and H. Zhan, *The Astrophysical Journal* **873**, 111 (2019).
- [207] A. M. Brooks, E. Papastergis, C. R. Christensen, F. Governato, A. Stilp, T. R. Quinn, and J. Wadsley, *The Astrophysical Journal* **850**, 97 (2017).
 - [208] A. Fitts, M. Boylan-Kolchin, B. Bozek, J. S. Bullock, A. Graus, V. Robles, P. F. Hopkins, K. El-Badry, S. Garrison-Kimmel, C.-A. Faucher-Giguère, A. Wetzel, and D. Kereš, *Monthly Notices of the Royal Astronomical Society* **490**, 962 (2019).
 - [209] A. Banerjee, K. K. Boddy, F.-Y. Cyr-Racine, A. L. Erickcek, D. Gilman, V. Gluscevic, S. Kim, B. V. Lehmann, Y.-Y. Mao, P. Mocz, F. Munshi, E. O. Nadler, L. Necib, A. Parikh, A. H. G. Peter, L. Sales, M. Vogelsberger, and A. C. Wright, arXiv e-prints -, arXiv:2203.07049 (2022).
 - [210] J. D. Van Nest, F. Munshi, A. C. Wright, M. Tremmel, A. M. Brooks, D. Nagai, and T. Quinn, *The Astrophysical Journal* **926**, 92 (2022).
 - [211] P. G. van Dokkum, R. Abraham, A. Merritt, J. Zhang, M. Geha, and C. Conroy, *The Astrophysical Journal Letters* **798**, L45 (2015).
 - [212] M. J. Disney, *Nature* **263**, 573 (1976).
 - [213] A. Sandage and B. Binggeli, *Astronomical Journal* **89**, 919 (1984).
 - [214] C. Impey, G. Bothun, and D. Malin, *The Astrophysical Journal* **330**, 634 (1988).
 - [215] J. J. Dalcanton, D. N. Spergel, J. E. Gunn, M. Schmidt, and D. P. Schneider, *Astronomical Journal* **114**, 635 (1997).

- [216] C. J. Conselice, Research Notes of the American Astronomical Society **2**, 43 (2018).
- [217] J. Koda, M. Yagi, H. Yamanoi, and Y. Komiyama, The Astrophysical Journal Letters **807**, L2 (2015).
- [218] J. C. Mihos, P. R. Durrell, L. Ferrarese, J. J. Feldmeier, P. Côté, E. W. Peng, P. Harding, C. Liu, S. Gwyn, and J.-C. Cuillandre, The Astrophysical Journal **809**, L21 (2015).
- [219] R. F. J. van der Burg, A. Muzzin, and H. Hoekstra, Astronomy & Astrophysics **590**, A20 (2016).
- [220] A. Venhola, R. Peletier, E. Laurikainen, H. Salo, T. Lisker, E. Iodice, M. Capaccioli, G. Verdois Kleijn, E. Valentijn, and S. Mieske, Astronomy & Astrophysics **608**, A142 (2017).
- [221] S. Danieli, P. van Dokkum, A. Merritt, R. Abraham, J. Zhang, I. D. Karachentsev, and L. N. Makarova, The Astrophysical Journal **837**, 136 (2017).
- [222] E. Papastergis, E. A. K. Adams, and A. J. Romanowsky, Astronomy & Astrophysics **601**, L10 (2017).
- [223] J. P. Greco, J. E. Greene, M. A. Strauss, L. A. MacArthur, X. Flowers, A. D. Goulding, S. Huang, J. H. Kim, Y. Komiyama, A. Leauthaud, L. Leisman, R. H. Lupton, C. Sifón, and S.-Y. Wang, The Astrophysical Journal **857**, 104 (2018).
- [224] Y. Rong, Q. Guo, L. Gao, S. Liao, L. Xie, T. H. Puzia, S. Sun, and J. Pan, Monthly Notices of the Royal Astronomical Society **470**, 4231 (2017).
- [225] A. Ferré-Mateu, A. Alabi, D. A. Forbes, A. J. Romanowsky, J. Brodie, V. Pandya, I. Martín-Navarro, S. Bellstedt, A. Wasserman, M. B. Stone, and N. Okabe, Monthly Notices of the Royal Astronomical Society **479**, 4891 (2018).
- [226] D. Tanoglidis, A. Drlica-Wagner, K. Wei, T. S. Li, J. Sánchez, Y. Zhang, A. H. G. Peter, A. Feldmeier-Krause, J. Prat, K. Casey, A. Palmese, C. Sánchez, J. DeRose, C. Conselice, L. Gagnon, T. M. C. Abbott, M. Aguena, S. Allam, S. Avila, K. Bechtol, E. Bertin, S. Bhargava, D. Brooks, D. L. Burke, A. C. Rosell, M. C. Kind, J. Carretero, C. Chang, M. Costanzi, L. N. da Costa, J. De Vicente, S. Desai, H. T. Diehl, P. Doel, T. F. Eifler, S. Everett, A. E. Evrard, B. Flaugher, J. Frieman, J. García-Bellido, D. W. Gerdes, R. A. Gruendl, J. Gschwend, G. Gutierrez, W. G. Hartley, D. L. Hollowood, D. Huterer, D. J. James, E. Krause, K. Kuehn, N. Kuropatkin, M. A. G. Maia, M. March, J. L. Marshall, F. Menanteau, R. Miquel, R. L. C. Ogando, F. Paz-Chinchón, A. K. Romer, A. Roodman, E. Sanchez, V.

- Scarpine, S. Serrano, I. Sevilla-Noarbe, M. Smith, E. Suchyta, G. Tarle, D. Thomas, D. L. Tucker, A. R. Walker, and DES Collaboration, *The Astrophysical Journals* **252**, 18 (2021).
- [227] N. Chamba, I. Trujillo, and J. H. Knapen, in *Contributions to the XIV.0 Scientific Meeting (virtual) of the Spanish Astronomical Society* (-, -, 2020), p. 20.
 - [228] I. Trujillo, N. Chamba, and J. H. Knapen, *Monthly Notices of the Royal Astronomical Society* **493**, 87 (2020).
 - [229] P. van Dokkum, R. Abraham, A. J. Romanowsky, J. Brodie, C. Conroy, S. Danieli, D. Lokhorst, A. Merritt, L. Mowla, and J. Zhang, *The Astrophysical Journal Letters* **844**, L11 (2017).
 - [230] D. A. Forbes, A. Alabi, A. J. Romanowsky, J. P. Brodie, and N. Arimoto, *Monthly Notices of the Royal Astronomical Society* **492**, 4874 (2020).
 - [231] J. E. Doppel, L. V. Sales, J. F. Navarro, M. G. Abadi, E. W. Peng, E. Toloba, and F. Ramos-Almendares, *Monthly Notices of the Royal Astronomical Society* **502**, 1661 (2021).
 - [232] N. C. Amorisco, A. Monachesi, A. Agnello, and S. D. M. White, *Monthly Notices of the Royal Astronomical Society* **475**, 4235 (2018).
 - [233] T. Saifollahi, I. Trujillo, M. A. Beasley, R. F. Peletier, and J. H. Knapen, *Monthly Notices of the Royal Astronomical Society* **502**, 5921 (2021).
 - [234] T. Carleton, Y. Guo, F. Munshi, M. Tremmel, and A. Wright, *Monthly Notices of the Royal Astronomical Society* **502**, 398 (2021).
 - [235] P. van Dokkum, S. Danieli, Y. Cohen, A. Merritt, A. J. Romanowsky, R. Abraham, J. Brodie, C. Conroy, D. Lokhorst, L. Mowla, E. O'Sullivan, and J. Zhang, *Nature* **555**, 629 (2018).
 - [236] S. Danieli, P. van Dokkum, C. Conroy, R. Abraham, and A. J. Romanowsky, *The Astrophysical Journal Letters* **874**, L12 (2019).
 - [237] P. van Dokkum, S. Danieli, R. Abraham, C. Conroy, and A. J. Romanowsky, *The Astrophysical Journal Letters* **874**, L5 (2019).
 - [238] C. Yozin and K. Bekki, *Monthly Notices of the Royal Astronomical Society* **452**, 937 (2015).
 - [239] D. Dutta Chowdhury, F. C. van den Bosch, and P. van Dokkum, *The Astrophysical Journal* **877**, 133 (2019).
 - [240] N. C. Amorisco and A. Loeb, *Monthly Notices of the Royal Astronomical Society* **459**, L51 (2016).

- [241] G. Ogiya, Monthly Notices of the Royal Astronomical Society **480**, L106 (2018).
- [242] T. Carleton, R. Errani, M. Cooper, M. Kaplinghat, J. Peñarrubia, and Y. Guo, Monthly Notices of the Royal Astronomical Society **485**, 382 (2019).
- [243] A. Di Cintio, C. B. Brook, A. A. Dutton, A. V. Macciò, A. Obreja, and A. Dekel, Monthly Notices of the Royal Astronomical Society **466**, L1 (2017).
- [244] T. K. Chan, D. Kereš, A. Wetzel, P. F. Hopkins, C. A. Faucher-Giguère, K. El-Badry, S. Garrison-Kimmel, and M. Boylan-Kolchin, Monthly Notices of the Royal Astronomical Society **478**, 906 (2018).
- [245] F. Jiang, A. Dekel, J. Freundlich, A. J. Romanowsky, A. A. Dutton, A. V. Macciò, and A. Di Cintio, Monthly Notices of the Royal Astronomical Society **487**, 5272 (2019).
- [246] S. Liao, L. Gao, C. S. Frenk, R. J. J. Grand, Q. Guo, F. A. Gómez, F. Marinacci, R. Pakmor, S. Shao, and V. Springel, Monthly Notices of the Royal Astronomical Society **490**, 5182 (2019).
- [247] G. Martin, S. Kaviraj, C. Laigle, J. E. G. Devriendt, R. A. Jackson, S. Peirani, Y. Dubois, C. Pichon, and A. Slyz, Monthly Notices of the Royal Astronomical Society **485**, 796 (2019).
- [248] M. Tremmel, A. C. Wright, A. M. Brooks, F. Munshi, D. Nagai, and T. R. Quinn, Monthly Notices of the Royal Astronomical Society **497**, 2786 (2020).
- [249] A. C. Wright, M. Tremmel, A. M. Brooks, F. Munshi, D. Nagai, R. S. Sharma, and T. R. Quinn, Monthly Notices of the Royal Astronomical Society **502**, 5370 (2021).
- [250] S. Cardona-Barrero, A. Di Cintio, C. B. A. Brook, T. Ruiz-Lara, M. A. Beasley, J. Falcón-Barroso, and A. V. Macciò, Monthly Notices of the Royal Astronomical Society **497**, 4282 (2020).
- [251] L. Leisman, M. P. Haynes, S. Janowiecki, G. Hallenbeck, G. Józsa, R. Giovanelli, E. A. K. Adams, D. Bernal Neira, J. M. Cannon, W. F. Janesh, K. L. Rhode, and J. J. Salzer, The Astrophysical Journal **842**, 133 (2017).
- [252] A. Burkert, The Astrophysical Journal **838**, 93 (2017).
- [253] Y. Rong, X.-Y. Dong, T. H. Puzia, G. Galaz, R. Sánchez-Janssen, T. Cao, R. F. J. van der Burg, C. Sifón, P. E. Mancera Piña, M. Marcelo, G. D’Ago, H.-X. Zhang, E. J. Johnston, and P. Eigenthaler, The Astrophysical Journal **899**, 78 (2020).
- [254] E. Kado-Fong, M. Petrescu, M. Mohammad, J. Greco, J. E. Greene, E. A. K. Adams, S. Huang, L. Leisman, F. Munshi, D. Tanoglidis, and J. Van Nest, The Astrophysical Journal **920**, 72 (2021).

- [255] J. W. Wadsley, J. Stadel, and T. Quinn, *New Astronomy* **9**, 137 (2004).
- [256] B. P. Moster, T. Naab, and S. D. M. White, *Monthly Notices of the Royal Astronomical Society* **428**, 3121 (2013).
- [257] M. Schramm and J. D. Silverman, *The Astrophysical Journal* **767**, 13 (2013).
- [258] N. Katz and S. D. M. White, *The Astrophysical Journal* **412**, 455 (1993).
- [259] A. D. Ludlow, J. Schaye, M. Schaller, and J. Richings, *Monthly Notices of the Royal Astronomical Society* **488**, L123 (2019).
- [260] M. Tremmel, F. Governato, M. Volonteri, and T. R. Quinn, *Monthly Notices of the Royal Astronomical Society* **451**, 1868 (2015).
- [261] T. R. Saitoh and J. Makino, *The Astrophysical Journal Letters* **697**, L99 (2009).
- [262] S. Shen, J. Wadsley, and G. Stinson, *Monthly Notices of the Royal Astronomical Society* **407**, 1581 (2010).
- [263] J. W. Wadsley, G. Veeravalli, and H. M. P. Couchman, *Monthly Notices of the Royal Astronomical Society* **387**, 427 (2008).
- [264] I. S. Butsky, J. N. Burchett, D. Nagai, M. Tremmel, T. R. Quinn, and J. K. Werk, *Monthly Notices of the Royal Astronomical Society* **490**, 4292 (2019).
- [265] F. Haardt and P. Madau, *The Astrophysical Journal* **746**, 125 (2012).
- [266] A. Pontzen, F. Governato, M. Pettini, C. M. Booth, G. Stinson, J. Wadsley, A. Brooks, T. Quinn, and M. Haehnelt, *Monthly Notices of the Royal Astronomical Society* **390**, 1349 (2008).
- [267] R. Cen, *The Astrophysical Journals* **78**, 341 (1992).
- [268] J. H. Black, *Monthly Notices of the Royal Astronomical Society* **197**, 553 (1981).
- [269] D. A. Verner and G. J. Ferland, *The Astrophysical Journals* **103**, 467 (1996).
- [270] T. Abel, P. Anninos, Y. Zhang, and M. L. Norman, *New Astronomy* **2**, 181 (1997).
- [271] C. R. Christensen, F. Governato, T. Quinn, A. M. Brooks, S. Shen, J. McCleary, D. B. Fisher, and J. Wadsley, *Monthly Notices of the Royal Astronomical Society* **440**, 2843 (2014).
- [272] V. Bromm, A. Ferrara, P. S. Coppi, and R. B. Larson, *Monthly Notices of the Royal Astronomical Society* **328**, 969 (2001).

- [273] G. Stinson, A. Seth, N. Katz, J. Wadsley, F. Governato, and T. Quinn, Monthly Notices of the Royal Astronomical Society **373**, 1074 (2006).
- [274] P. Kroupa, Monthly Notices of the Royal Astronomical Society **322**, 231 (2001).
- [275] J. M. Bellovary, F. Governato, T. R. Quinn, J. Wadsley, S. Shen, and M. Volonteri, The Astrophysical Journal Letters **721**, L148 (2010).
- [276] M. Tremmel, F. Governato, M. Volonteri, T. R. Quinn, and A. Pontzen, Monthly Notices of the Royal Astronomical Society **475**, 4967 (2018).
- [277] M. Tremmel, F. Governato, M. Volonteri, A. Pontzen, and T. R. Quinn, The Astrophysical Journal Letters **857**, L22 (2018).
- [278] S. R. Knollmann and A. Knebe, The Astrophysical Journals **182**, 608 (2009).
- [279] G. L. Bryan and M. L. Norman, The Astrophysical Journal **495**, 80 (1998).
- [280] M. Geha, M. R. Blanton, R. Yan, and J. L. Tinker, The Astrophysical Journal **757**, 85 (2012).
- [281] A. Pontzen, R. Roškar, G. Stinson, and R. Woods, pynbody: N-Body/SPH analysis for python, Astrophysics Source Code Library, record ascl 1305.002, 2013.
- [282] A. Pontzen and M. Tremmel, The Astrophysical Journals **237**, 23 (2018).
- [283] S. Jester, D. P. Schneider, G. T. Richards, R. F. Green, M. Schmidt, P. B. Hall, M. A. Strauss, D. E. Vand en Berk, C. Stoughton, J. E. Gunn, J. Brinkmann, S. M. Kent, J. A. Smith, D. L. Tucker, and B. Yanny, Astronomical Journal **130**, 873 (2005).
- [284] I. Trujillo and J. Fliri, The Astrophysical Journal **823**, 123 (2016).
- [285] A. Borlaff, I. Trujillo, J. Román, J. E. Beckman, M. C. Eliche-Moral, R. Infante-Sáinz, A. Lumbreras-Calle, R. T. S. M. de Almagro, C. Gómez-Guijarro, M. Cebrián, A. Dorta, N. Cardiel, M. Akhlaghi, and C. Martínez-Lombilla, Astronomy & Astrophysics **621**, A133 (2019).
- [286] J. L. Sérsic, Boletin de la Asociacion Argentina de Astronomia La Plata Argentina **6**, 41 (1963).
- [287] A. A. Dutton, T. Buck, A. V. Macciò, K. L. Dixon, M. Blank, and A. Obreja, Monthly Notices of the Royal Astronomical Society **499**, 2648 (2020).
- [288] H. Hetznecker and A. Burkert, Monthly Notices of the Royal Astronomical Society **370**, 1905 (2006).

- [289] Y. Dubois, C. Pichon, C. Welker, D. Le Borgne, J. Devriendt, C. Laigle, S. Codis, D. Pogosyan, S. Arnouts, K. Benabed, E. Bertin, J. Blaizot, F. Bouchet, J. F. Cardoso, S. Colombi, V. de Lapparent, V. Desjacques, R. Gavazzi, S. Kassin, T. Kimm, H. McCracken, B. Milliard, S. Peirani, S. Prunet, S. Roubertol, J. Silk, A. Slyz, T. Sousbie, R. Teyssier, L. Tresse, M. Treger, D. Vibert, and M. Volonteri, *Monthly Notices of the Royal Astronomical Society* **444**, 1453 (2014).
- [290] R. A. Jackson, G. Martin, S. Kaviraj, M. Ramsøy, J. E. G. Devriendt, T. Sedgwick, C. Laigle, H. Choi, R. S. Beckmann, M. Volonteri, Y. Dubois, C. Pichon, S. K. Yi, A. Slyz, K. Kraljic, T. Kimm, S. Peirani, and I. Baldry, *Monthly Notices of the Royal Astronomical Society* **502**, 4262 (2021).
- [291] Y. Dubois, R. Beckmann, F. Bournaud, H. Choi, J. Devriendt, R. Jackson, S. Kaviraj, T. Kimm, K. Kraljic, C. Laigle, G. Martin, M.-J. Park, S. Peirani, C. Pichon, M. Volonteri, and S. K. Yi, *Astronomy & Astrophysics* **651**, A109 (2021).
- [292] R. F. J. van der Burg, H. Hoekstra, A. Muzzin, C. Sifón, M. Viola, M. N. Bremer, S. Brough, S. P. Driver, T. Erben, C. Heymans, H. Hildebrandt, B. W. Holwerda, D. Klaes, K. Kuijken, S. McGee, R. Nakajima, N. Napolitano, P. Norberg, E. N. Taylor, and E. Valentijn, *Astronomy & Astrophysics* **607**, A79 (2017).
- [293] J. Van Nest, F. Munshi, C. Christensen, A. M. Brooks, M. Tremmel, and T. R. Quinn, *The Astrophysical Journal* **956**, 96 (2023).
- [294] M. L. Mateo, *Annual Review of Astronomy & Astrophysics* **36**, 435 (1998).
- [295] S. Koposov, V. Belokurov, N. W. Evans, P. C. Hewett, M. J. Irwin, G. Gilmore, D. B. Zucker, H. W. Rix, M. Fellhauer, E. F. Bell, and E. V. Glushkova, *The Astrophysical Journal* **686**, 279 (2008).
- [296] J. D. Simon, *Annual Review of Astronomy & Astrophysics* **57**, 375 (2019).
- [297] R. A. Ibata, G. F. Lewis, A. W. McConnachie, N. F. Martin, M. J. Irwin, A. M. N. Ferguson, A. Babul, E. J. Bernard, S. C. Chapman, M. Collins, M. Fardal, A. D. Mackey, J. Navarro, J. Peñarrubia, R. M. Rich, N. Tanvir, and L. Widrow, *The Astrophysical Journal* **780**, 128 (2014).
- [298] N. F. Martin, R. A. Ibata, G. F. Lewis, A. McConnachie, A. Babul, N. F. Bate, E. Bernard, S. C. Chapman, M. M. L. Collins, A. R. Conn, D. Crnojević, M. A. Fardal, A. M. N. Ferguson, M. Irwin, A. D. Mackey, B. McMonigal, J. F. Navarro, and R. M. Rich, *The Astrophysical Journal* **833**, 167 (2016).
- [299] A. W. McConnachie, R. Ibata, N. Martin, A. M. N. Ferguson, M. Collins, S. Gwyn, M. Irwin, G. F. Lewis, A. D. Mackey, T. Davidge, V. Arias, A. Conn,

- P. Côté, D. Crnojevic, A. Huxor, J. Penarrubia, C. Spengler, N. Tanvir, D. Valls-Gabaud, A. Babul, P. Barmby, N. F. Bate, E. Bernard, S. Chapman, A. Dotter, W. Harris, B. McMonigal, J. Navarro, T. H. Puzia, R. M. Rich, G. Thomas, and L. M. Widrow, *The Astrophysical Journal* **868**, 55 (2018).
- [300] A. Drlica-Wagner, K. Bechtol, E. S. Rykoff, E. Luque, A. Queiroz, Y. Y. Mao, R. H. Wechsler, J. D. Simon, B. Santiago, B. Yanny, E. Balbinot, S. Dodelson, A. Fausti Neto, D. J. James, T. S. Li, M. A. G. Maia, J. L. Marshall, A. Pieres, K. Stringer, A. R. Walker, T. M. C. Abbott, F. B. Abdalla, S. Allam, A. Benoit-Lévy, G. M. Bernstein, E. Bertin, D. Brooks, E. Buckley-Geer, D. L. Burke, A. Carnero Rosell, M. Carrasco Kind, J. Carretero, M. Crocce, L. N. da Costa, S. Desai, H. T. Diehl, J. P. Dietrich, P. Doel, T. F. Eifler, A. E. Evrard, D. A. Finley, B. Flaugher, P. Fosalba, J. Frieman, E. Gaztanaga, D. W. Gerdes, D. Gruen, R. A. Gruendl, G. Gutierrez, K. Honscheid, K. Kuehn, N. Kuropatkin, O. Lahav, P. Martini, R. Miquel, B. Nord, R. Ogando, A. A. Plazas, K. Reil, A. Roodman, M. Sako, E. Sanchez, V. Scarpine, M. Schubnell, I. Sevilla-Noarbe, R. C. Smith, M. Soares-Santos, F. Sobreira, E. Suchyta, M. E. C. Swanson, G. Tarle, D. Tucker, V. Vikram, W. Wester, Y. Zhang, J. Zuntz, and DES Collaboration, *The Astrophysical Journal* **813**, 109 (2015).
- [301] S. E. Koposov, V. Belokurov, G. Torrealba, and N. W. Evans, *The Astrophysical Journal* **805**, 130 (2015).
- [302] M. Geha, R. H. Wechsler, Y.-Y. Mao, E. J. Tollerud, B. Weiner, R. Bernstein, B. Hoyle, S. Marchi, P. J. Marshall, R. Muñoz, and Y. Lu, *The Astrophysical Journal* **847**, 4 (2017).
- [303] Y.-Y. Mao, M. Geha, R. H. Wechsler, B. Weiner, E. J. Tollerud, E. O. Nadler, and N. Kallivayalil, *The Astrophysical Journal* **907**, 85 (2021).
- [304] S. G. Carlsten, J. P. Greco, R. L. Beaton, and J. E. Greene, *The Astrophysical Journal* **891**, 144 (2020).
- [305] S. G. Carlsten, J. E. Greene, J. P. Greco, R. L. Beaton, and E. Kado-Fong, *The Astrophysical Journal* **922**, 267 (2021).
- [306] S. G. Carlsten, J. E. Greene, A. H. G. Peter, R. L. Beaton, and J. P. Greco, *The Astrophysical Journal* **908**, 109 (2021).
- [307] S. G. Carlsten, J. E. Greene, R. L. Beaton, S. Danieli, and J. P. Greco, *The Astrophysical Journal* **933**, 47 (2022).
- [308] A. S. Font, I. G. McCarthy, V. Belokurov, S. T. Brown, and S. G. Stafford, *Monthly Notices of the Royal Astronomical Society* **511**, 1544 (2022).
- [309] H. B. Akins, C. R. Christensen, A. M. Brooks, F. Munshi, E. Applebaum, A. Engelhardt, and L. Chamberland, *The Astrophysical Journal* **909**, 139 (2021).

- [310] C. Engler, A. Pillepich, A. Pasquali, D. Nelson, V. Rodriguez-Gomez, K. T. E. Chua, E. K. Grebel, V. Springel, F. Marinacci, R. Weinberger, M. Vogelsberger, and L. Hernquist, *Monthly Notices of the Royal Astronomical Society* **507**, 4211 (2021).
- [311] A. Karunakaran, K. Spekkens, K. A. Oman, C. M. Simpson, A. Fattahi, D. J. Sand, P. Bennet, D. Crnojević, C. S. Frenk, F. A. Gómez, R. J. J. Grand, M. G. Jones, F. Marinacci, B. Mutlu-Pakdil, J. F. Navarro, and D. Zaritsky, *The Astrophysical Journal Letters* **916**, L19 (2021).
- [312] J. Samuel, A. Wetzel, I. Santistevan, E. Tollerud, J. Moreno, M. Boylan-Kolchin, J. Bailin, and B. Pardasani, *Monthly Notices of the Royal Astronomical Society* **514**, 5276 (2022).
- [313] A. R. Wetzel, E. J. Tollerud, and D. R. Weisz, *The Astrophysical Journal Letters* **808**, L27 (2015).
- [314] C. M. Simpson, R. J. J. Grand, F. A. Gómez, F. Marinacci, R. Pakmor, V. Springel, D. J. R. Campbell, and C. S. Frenk, *Monthly Notices of the Royal Astronomical Society* **478**, 548 (2018).
- [315] R. C. Simons, M. S. Peebles, J. Tumlinson, B. W. O’Shea, B. D. Smith, L. Corlies, C. Lochhaas, Y. Zheng, R. Augustin, D. Prasad, G. F. Snyder, and E. Tollerud, *The Astrophysical Journal* **905**, 167 (2020).
- [316] C. Engler, A. Pillepich, G. D. Joshi, A. Pasquali, D. Nelson, and E. K. Grebel, *Monthly Notices of the Royal Astronomical Society* **522**, 5946 (2023).
- [317] J. W. Wadsley, B. W. Keller, and T. R. Quinn, *Monthly Notices of the Royal Astronomical Society* **471**, 2357 (2017).
- [318] A. D. Ludlow, J. Schaye, M. Schaller, and J. Richings, *Monthly Notices of the Royal Astronomical Society* **488**, L123 (2019).
- [319] A. Ricarte, M. Tremmel, P. Natarajan, and T. Quinn, *Monthly Notices of the Royal Astronomical Society* **489**, 802 (2019).
- [320] R. S. Sharma, A. M. Brooks, M. Tremmel, J. Bellovary, A. Ricarte, and T. R. Quinn, *The Astrophysical Journal* **936**, 82 (2022).
- [321] R. S. Sharma, A. M. Brooks, M. Tremmel, J. Bellovary, and T. R. Quinn, arXiv e-prints -, arXiv:2211.05275 (2022).
- [322] J. Guedes, S. Callegari, P. Madau, and L. Mayer, *The Astrophysical Journal* **742**, 76 (2011).
- [323] A. V. Kravtsov, A. A. Vikhlinin, and A. V. Meshcheryakov, *Astronomy Letters* **44**, 8 (2018).

- [324] A. Smercina, E. F. Bell, P. A. Price, R. D’Souza, C. T. Slater, J. Bailin, A. Monachesi, and D. Nidever, *The Astrophysical Journal* **863**, 152 (2018).
- [325] P. Bennet, D. J. Sand, D. Crnojević, K. Spekkens, A. Karunakaran, D. Zaritsky, and B. Mutlu-Pakdil, *The Astrophysical Journal* **885**, 153 (2019).
- [326] W. E. Harris and S. van den Bergh, *Astronomical Journal* **86**, 1627 (1981).
- [327] M. Nashimoto, M. Tanaka, M. Chiba, K. Hayashi, Y. Komiyama, and T. Okamoto, *The Astrophysical Journal* **936**, 38 (2022).
- [328] A. S. Font, I. G. McCarthy, and V. Belokurov, *Monthly Notices of the Royal Astronomical Society* **505**, 783 (2021).
- [329] A. S. Font, I. G. McCarthy, R. Poole-Mckenzie, S. G. Stafford, S. T. Brown, J. Schaye, R. A. Crain, T. Theuns, and M. Schaller, *Monthly Notices of the Royal Astronomical Society* **498**, 1765 (2020).
- [330] M. Geha, M. R. Blanton, R. Yan, and J. L. Tinker, *The Astrophysical Journal* **757**, 85 (2012).
- [331] M. Donnari, A. Pillepich, D. Nelson, F. Marinacci, M. Vogelsberger, and L. Hernquist, *Monthly Notices of the Royal Astronomical Society* **506**, 4760 (2021).
- [332] C. M. Dickey, T. K. Starkenburg, M. Geha, C. Hahn, D. Anglés-Alcázar, E. Choi, R. Davé, S. Genel, K. G. Iyer, A. H. Maller, N. Mandelker, R. S. Somerville, and L. Y. A. Yung, *The Astrophysical Journal* **915**, 53 (2021).
- [333] S. Garrison-Kimmel, A. Wetzel, P. F. Hopkins, R. Sanderson, K. El-Badry, A. Graus, T. K. Chan, R. Feldmann, M. Boylan-Kolchin, C. C. Hayward, J. S. Bullock, A. Fitts, J. Samuel, C. Wheeler, D. Kereš, and C.-A. Faucher-Giguère, *Monthly Notices of the Royal Astronomical Society* **489**, 4574 (2019).
- [334] E. Kado-Fong, J. E. Greene, S. Huang, R. Beaton, A. D. Goulding, and Y. Komiyama, *The Astrophysical Journal* **900**, 163 (2020).
- [335] W. L. Xu and L. Randall, *The Astrophysical Journal* **900**, 69 (2020).
- [336] E. Papastergis, R. Giovanelli, M. P. Haynes, and F. Shankar, *Astronomy & Astrophysics* **574**, A113 (2015).
- [337] E. L. Lokas, *Monthly Notices of the Royal Astronomical Society* **394**, L102 (2009).
- [338] M. G. Walker and J. Peñarrubia, *The Astrophysical Journal* **742**, 20 (2011).
- [339] N. C. Amorisco and N. W. Evans, *The Astrophysical Journal Letters* **756**, L2 (2012).

- [340] M. S. Pawlowski, S. S. McGaugh, and H. Jerjen, Monthly Notices of the Royal Astronomical Society **453**, 1047 (2015).
- [341] A. Marasco, K. A. Oman, J. F. Navarro, C. S. Frenk, and T. Oosterloo, Monthly Notices of the Royal Astronomical Society **476**, 2168 (2018).
- [342] S. Roychowdhury, J. N. Chengalur, I. D. Karachentsev, and E. I. Kaisina, Monthly Notices of the Royal Astronomical Society **436**, L104 (2013).
- [343] A. van der Wel, Y.-Y. Chang, E. F. Bell, B. P. Holden, H. C. Ferguson, M. Giavalisco, H. W. Rix, R. Skelton, K. Whitaker, I. Momcheva, G. Brammer, S. A. Kassin, M. Martig, A. Dekel, D. Ceverino, D. C. Koo, M. Mozena, P. G. van Dokkum, M. Franx, S. M. Faber, and J. Primack, The Astrophysical Journal Letters **792**, L6 (2014).
- [344] H. Zhang, J. R. Primack, S. M. Faber, D. C. Koo, A. Dekel, Z. Chen, D. Ceverino, Y.-Y. Chang, J. J. Fang, Y. Guo, L. Lin, and A. v. d. Wel, Monthly Notices of the Royal Astronomical Society **484**, 5170 (2019).
- [345] J. F. Navarro, C. S. Frenk, and S. D. M. White, The Astrophysical Journal **462**, 563 (1996).
- [346] A. W. McConnachie, The Astronomical Journal **144**, 4 (2012).
- [347] M. G. Walker, M. Mateo, and E. W. Olszewski, The Astronomical Journal **137**, 3100 (2009).
- [348] X.-Z. Er, Research in Astronomy and Astrophysics **13**, 517 (2013).
- [349] A. Burkert, The Astrophysical Journal **808**, 158 (2015).
- [350] C. Christensen, T. Quinn, F. Governato, A. Stilp, S. Shen, and J. Wadsley, Monthly Notices of the Royal Astronomical Society **425**, 3058 (2012).
- [351] C. F. McKee and J. P. Ostriker, The Astrophysical Journal **218**, 148 (1977).
- [352] J. H. Wise, T. Abel, M. J. Turk, M. L. Norman, and B. D. Smith, Monthly Notices of the Royal Astronomical Society **427**, 311 (2012).
- [353] O. Agertz, A. V. Kravtsov, S. N. Leitner, and N. Y. Gnedin, The Astrophysical Journal **770**, 25 (2013).
- [354] B. Allgood, R. A. Flores, J. R. Primack, A. V. Kravtsov, R. H. Wechsler, A. Faltenbacher, and J. S. Bullock, Monthly Notices of the Royal Astronomical Society **367**, 1781 (2006).
- [355] M. Tomassetti, A. Dekel, N. Mandelker, D. Ceverino, S. Lapiner, S. Faber, O. Kneller, J. Primack, and T. Sai, Monthly Notices of the Royal Astronomical Society **458**, 4477 (2016).

- [356] M. Franx, G. Illingworth, and T. de Zeeuw, *The Astrophysical Journal* **383**, 112 (1991).
- [357] D. Foreman-Mackey, D. W. Hogg, D. Lang, and J. Goodman, *Publications of the Astronomical Society of the Pacific* **125**, 306 (2013).
- [358] A. Fitts, M. Boylan-Kolchin, O. D. Elbert, J. S. Bullock, P. F. Hopkins, J. Oñorbe, A. Wetzel, C. Wheeler, C.-A. Faucher-Giguère, D. Kereš, E. D. Skillman, and D. R. Weisz, *Monthly Notices of the Royal Astronomical Society* **471**, 3547 (2017).
- [359] P. F. Hopkins, A. Wetzel, D. Kereš, C.-A. Faucher-Giguère, E. Quataert, M. Boylan-Kolchin, N. Murray, C. C. Hayward, S. Garrison-Kimmel, C. Hummels, R. Feldmann, P. Torrey, X. Ma, D. Anglés-Alcázar, K.-Y. Su, M. Orr, D. Schmitz, I. Escala, R. Sanderson, M. Y. Grudić, Z. Hafen, J.-H. Kim, A. Fitts, J. S. Bullock, C. Wheeler, T. K. Chan, O. D. Elbert, and D. Narayanan, *Monthly Notices of the Royal Astronomical Society* **480**, 800 (2018).
- [360] M. Kaplinghat, S. Tulin, and H.-B. Yu, *Physical Review Letters* **116**, 041302 (2016).